

Dynamics, Control and Flight Testing of an
Unmanned, Finless Airship

Hashim Mazhar

Master of Engineering

Department of Mechanical Engineering

McGill University

Montreal, Quebec

December 2012

A thesis submitted to McGill University
in partial fulfilment of the requirements of the degree of
Master of Engineering

©Hashim Mazhar, 2012

ACKNOWLEDGEMENTS

First and foremost, I would like to extend my deepest gratitude to my supervisor Meyer Nahon for his unending support and thorough guidance over the course of this thesis. His insights and his patience were key towards completion of this work. I also thank him for his financial support during two years of my Masters.

I am grateful to my good friend, colleague and ex-PhD student, Torsten Liesk. He is a pleasure to work with, and his guidance in various domains of this research, especially during the flight tests, were irreplaceable.

I would like to thank the summer, intern and exchange students that worked at the lab for their interest in this research, and their contribution towards it. They are Maja Sevaldson, Sylvain Joassard, Matthias Borresman and Ryan Caverly.

In addition, I want to acknowledge the technical support of Quanser Inc. who designed the airship, as in the current work.

I thank my parents, Mazhar Alam and Salma Akhtar, who not only taught me the value of knowledge, but dedicated their all to aid me in its pursuit.

Last but not least, I thank my wife, Meaghan Seymour. I would not be completing this thesis without your help. You add life to living.

ABSTRACT

This thesis discusses a number of developments in the dynamics and control of a novel, autonomous, highly-maneuverable, finless, almost-lighter-than-air vehicle (ALTAV). The airship is inherently unstable due to absence of fins and is highly prone to winds. Four vectored thrusters are used to ensure closed-loop stability. This thesis deals with improvements made to an existing dynamics model, including the incorporation of the rotational damping moments of the airship, the drag resulting from the protuberances on the airship hull, the reaction torques and the gyroscopic moments on the airship due to the thrusters. Open-loop and closed-loop tests were designed and carried out to validate the physical parameters that were empirically estimated, and, in general, good agreement was obtained. Furthermore, a complete controller suite that includes a low-level controller and a high-level guidance controller was designed and implemented for autonomous operation of the vehicle. Experimental testing was carried out to validate the performance of the controller suite in the presence of winds. The controller suite was shown to perform reliably even under the influence of winds of comparable magnitude to the airship's speed.

ABRÉGÉ

Cette thèse examine le dynamique et contrôle d'un dirigeable autonome, extrêmement manœuvrable, dépourvu d'ailerons et presque plus léger que l'air (ALTAV). Ce dirigeable est intrinsèquement instable dû à l'absence de surfaces stabilisatrices et aussi très susceptible au vent. Quatre propulseurs vectorisés sont utilisés pour assurer la stabilité en boucle fermée. Cette thèse concerne les améliorations au modèle dynamique existant, incluant l'incorporation des moments d'amortissements rotationnels du dirigeable, la traînée résultant des protubérances du dirigeable, les torques de réactions et moments gyroscopiques sur le dirigeable dû aux propulseurs. Des essais à boucle ouverte et boucle fermée ont été conçus et effectués pour valider les paramètres physiques estimés empiriquement, et, en général, un bon accord a été obtenu. En outre, une suite de contrôle incluant un contrôleur à bas niveau et un contrôleur d'orientation de haut niveau a été conçu et mis en œuvre pour l'opération autonome du véhicule. Les essais expérimentaux ont été effectués pour valider la performance de la suite de contrôle en présence de vents variables. Cet ensemble de contrôle a été démontré fiable même sous l'influence de vents de vitesses comparable à la vitesse du dirigeable.

TABLE OF CONTENTS

ACKNOWLEDGEMENTS	i	
ABSTRACT.....	ii	
ABRÉGÉ.....	iii	
LIST OF TABLES	vii	
LIST OF FIGURES	viii	
Chapter 1	Introduction.....	1
1.1	Background.....	1
1.1.1	The Mk-II ALTAV	3
1.1.2	Thesis Motivation and Objectives	4
1.2	Literature Review	5
1.2.1	Rotational Damping Moments Estimation	5
1.2.2	Protuberance Drag	6
1.2.3	Reaction Torques	7
1.2.4	Thruster Gyroscopic Moments	8
1.2.5	Autonomous Vehicle Guidance.....	9
1.3	Thesis Organization.....	10
Chapter 2	Improvements to the Current Airship Model	11
2.1	Existing Dynamics Model	11
2.1.1	Relevant Frame Transformations	11
2.1.2	Airship Dynamics – Equations of Motion.....	13
2.2	Improvements to the Dynamics Model.....	16
2.2.1	Theoretical Estimation of Rotational Damping Moments.....	17
2.2.2	Effect of Protuberances on the Axial Drag Coefficient.....	20
2.3	Improvements to the Thruster Model	24
2.3.1	Moment of Inertia of the Thrusters.....	25
2.3.2	Determining Angular Velocity of the Propellers.....	26

2.3.3	Gyroscopic Moments due to the Thrusters	27
2.3.4	Reaction Torques due to the Thrusters	30
2.4	Implementing the Improvements to the Simulation Model	35
2.5	The Airship Hull – Refining its Geometric Description.....	40
2.5.1	Measurement.....	40
2.5.2	Refined CAD Model.....	41
Chapter 3	The Airship Controller Suite - Low and High Level Controllers	43
3.1	Controller Architecture.....	43
3.2	Low-Level controller	44
3.2.1	Simulation Results for the Low-Level Controller	46
3.3	High-Level Controller	48
3.3.1	Non-Dynamics-Based Guidance Algorithm:.....	48
3.3.2	Dynamics Based Guidance Algorithm	52
Chapter 4	Flight Tests and Controller Validation	67
4.1	Experimental setup	67
4.1.1	Overall Architecture	67
4.1.2	DAQ and On-board Microcontroller	68
4.1.3	Thrusters	69
4.1.4	Sensors.....	71
4.2	Validation of Airship Dynamics Model	75
4.2.1	Airship Pre-flight and Post-Flight Measurements	76
4.2.2	Heaviness and Center of Gravity Location Test.....	78
4.2.3	Normal Drag Test	81
4.2.4	Axial Drag Test.....	83
4.2.5	Damping Moment Coefficient Test.....	87
4.2.6	Experimental Determination of Added Masses.....	90
4.2.7	Experimental Validation of Thruster Reaction Torques.....	97

4.2.8	Munk Moment Validation	99
4.3	Closed-Loop Controller Suite Validation	104
4.3.1	Low-Level Controller Validation	105
4.3.2	Complete Controller Suite Validation	108
Chapter 5	Conclusions and Recommendations for Future Work.....	112
5.1	Improvements to the Dynamics Model.....	112
5.2	The Airship Controller Suite Design	113
5.3	Validation and Flight Testing	114
5.4	Future Work.....	115
Bibliography	117
Appendix A	Experimental Setup for Measuring Thrust/Torque Data	121
Appendix B	Estimation of the Aerodynamic Hull Forces	124
Appendix C	The Cross-flow Drag Model	125
Appendix D	Results for Reaction Torques Test.....	131
Appendix E	Results for Normal Drag Test.....	133
Appendix F	Results for Axial Drag Test	134
Appendix G	Results for Estimation of Longitudinal Added Mass	137

LIST OF TABLES

Table 2-1: Gondola and GPS Antenna dimensions (in meters)	21
Table 2-2: Normal and tangential force coefficients from [17]	23
Table 2-3: Inertial properties of the rotating thruster components	25
Table 2-4: Airship inertial properties and constants used in the dynamics model	42
Table 3-1: Summary of PID controller gains for the airship	46
Table 3-2: Waypoints describing the waylines in the simulation	50
Table 4-1: Airship's pre-flight and post-flight measurements.....	77
Table 4-2: Calculated parameters of the airship hull	77
Table 4-3: Airship thruster locations in the body-frame [8]	81
Table 4-4: Summary of results for normal drag test	82
Table 4-5: Results for forward drag test. Test cases A-F.....	84
Table 4-6: List of calculated values for experimental estimation of k_{ω}	89
Table 4-7: Summary of results for estimating longitudinal added mass.....	93
Table 4-8: Summary of results for estimating lateral added mass	96
Table 4-9: Gains used in guidance experiment.....	109
Table 4-10: Waypoint list for guidance experiment	109

LIST OF FIGURES

Figure 1-1: Meusnier’s <i>Dirigible</i> [3].	1
Figure 1-2: The Hindenburg (LZ-129) right after it burst into flames [4].	1
Figure 1-3: The hybrid LEMV concept [6].	2
Figure 1-4: The Solar Ship [7].	2
Figure 1-5: The Mk-II ALTAV [8].	3
Figure 1-6: Thruster arrangement [8].	3
Figure 2-1: The inertial NED frame and the airship body frame [8].	12
Figure 2-2: The thruster frame and the body frame.	13
Figure 2-3: Added mass and inertia factors versus fineness ratio [36].	15
Figure 2-4: Airship with circular cross-section.	18
Figure 2-5: Differential disc element at a distance x from the center of buoyancy.	18
Figure 2-6: Gondola and on-board GPS antenna.	22
Figure 2-7: Illustration of the viscous drag forces on the thruster legs.	23
Figure 2-8: CAD model of the thruster.	25
Figure 2-9: Thrust versus rpm^2 as measured in [8].	27
Figure 2-10: Servo rotation in the thruster frame.	28
Figure 2-11: Typical reaction torque curve, $c = 0.35$.	31
Figure 2-12: Typical reaction torque curve, $c = 0.35$. Details of rise and fall.	31
Figure 2-13 : Torque vs. Thrust. Experiment and linear fit.	32
Figure 2-14: Estimated and measured reaction toqrues.	34
Figure 2-15: Estimated and measured reaction torque, details of rise and fall.	34
Figure 2-16: Block diagram of the torque dynamics model.	35
Figure 2-17: Top to bottom: roll, pitch, yaw, forward velocity and height. Results for test cases (a) and (b).	37
Figure 2-18: Thruster forces and moments, top to bottom: F_x , F_z , M_x , M_y and M_z for tests cases (a) and (b).	38
Figure 2-19: Measuring hull profile by suspending plumb-bobs.	41
Figure 2-20: New hull profile polynomial approximation.	41
Figure 3-1: Schematic of the overall airship controller.	44
Figure 3-2: Pitch profile. PID simulation.	47
Figure 3-3: Yaw profile. PID simulation.	47

Figure 3-4: Inertial height profile. PID simulation	47
Figure 3-5: Velocity profile. PID simulation	47
Figure 3-6: Roll profile. PID simulation	48
Figure 3-7: The ghost vehicle and the desired wayline in the X_t - Y_t frame.....	49
Figure 3-8: Desired path in NEU frame.....	50
Figure 3-9: Airship trajectory in NE frame - test case 1.....	51
Figure 3-10: Height profile - test case 1	51
Figure 3-11: Airship trajectory in NE frame - test case 2.....	51
Figure 3-12: Height profile - test case 2	51
Figure 3-13: Illustration of airship's airspeed and groundspeed	53
Figure 3-14: Track-frame orientation	54
Figure 3-15: Function to generate χ_c as a function of y_t	56
Figure 3-16: Illustration of proposed guidance strategy.....	57
Figure 3-17: Diagrammatic illustration of angle-relations to represent ground speed in the track frame.	59
Figure 3-18: Wind compensation by the proposed guidance algorithm.	61
Figure 3-19: Desired height generation	62
Figure 3-20: Airship trajectory in NE frame – test case 1	64
Figure 3-21: Height profile with dynamics based guidance algorithm - test case 1	64
Figure 3-22: Yaw profile with the proposed waypoint controller – test case 1	64
Figure 3-23: Pitch profile with the proposed waypoint controller - test case 1	64
Figure 3-24: Airship trajectory in NED frame – test case 2	65
Figure 3-25: Height profile with dynamics based guidance algorithm - test case 2	65
Figure 3-26: Yaw profile with dynamics based guidance algorithm - test case 2	65
Figure 3-27: Pitch profile with dynamics based guidance algorithm - test case 2.....	65
Figure 4-1: Flight setup of the airship.....	68
Figure 4-2: Airship GUI for field testing.....	69
Figure 4-3: Joystick to provide desired states when HLC is not engaged.	69
Figure 4-4: GPS base antenna.....	69
Figure 4-5: GPS base receiver	69
Figure 4-6: Hitec HS-322HD servo motor.....	70
Figure 4-7: PJS 3D-1000N brushless motor	70
Figure 4-8: APC 12" \times 3.8" propeller	70

Figure 4-9: JETI Advance 30 Plus ESC	70
Figure 4-10: Schematic of the thruster setup	71
Figure 4-11: Microstrain 3DM-GX3-25-OEM™ Inertial Measurement Unit.....	71
Figure 4-12: System configuration with DGPS	73
Figure 4-13: System configuration with SGPS.....	74
Figure 4-14: MB 1260 XL –MaxSonar-EZL0 sonar	75
Figure 4-15: WindSonic 2-Axis ultrasonic anemometer	75
Figure 4-16: Concordia Stinger Dome[44]	76
Figure 4-17: Inertial height during heaviness test.....	79
Figure 4-18: Raw thruster forces in z during heaviness tests	80
Figure 4-19: Filtered thruster forces in z during heaviness test.....	80
Figure 4-20: Moment balance during hover, top view.	80
Figure 4-21: Force balance for the drop test under terminal velocity conditions	82
Figure 4-22: Inertial height during drop test – Test case A	83
Figure 4-23: Downward velocity during drop test – Test case A	83
Figure 4-24: Steady-state force balance in x-direction - forward drag test	84
Figure 4-25: Total thrust in x, test case A	85
Figure 4-26: Forward velocity, test case A.....	85
Figure 4-27: Linear fit to determine the forward drag coefficient.....	85
Figure 4-28: Flow over the airship hull without thrusters.	87
Figure 4-29: Flow over the airship hull with thrusters in operation.	87
Figure 4-30: Total thruster-induced moment during estimation of rotational damping coefficient.	88
Figure 4-31: Yaw-rate during estimation of rotational damping coefficient.....	88
Figure 4-32: $M_{z,thruster}$ vs. r^2 ; experimental data points and linear fit	89
Figure 4-33: Commanded thrusts in x-direction (top) and forward acceleration (bottom) – Forward acceleration test : Test case 1	93
Figure 4-34: Commanded thrusts in z-direction and $h_a g - D_N$ (top), and vertical acceleration (bottom) – Lateral added mass test : test case 1	96
Figure 4-35: Commanded thrusts in z-direction and $h_a g - D_N$ (top), and vertical acceleration (bottom) – Lateral added mass test : test case 3	96
Figure 4-36: Experimental yaw-rates (a) and (c) and corresponding commanded thrust in z-direction profiles (c) and (d).....	98
Figure 4-37: Munk moment test 1, u	101

Figure 4-38: Munk moment test 1, average thrust	101
Figure 4-39: Munk moment test 1, v	101
Figure 4-40: Munk moment test 1, Munk moment in y	101
Figure 4-41: Munk moment test 1, w	101
Figure 4-42: Munk moment test 1, Munk moment in z	101
Figure 4-43: Munk moment test 1, pitch	101
Figure 4-44: Munk moment test 1, yaw	101
Figure 4-45: Munk moment test 2, u	103
Figure 4-46: Munk moment test 2, Munk moment in y	103
Figure 4-47: Munk moment test 2, v	103
Figure 4-48: Munk moment test 2, Munk moment in z	103
Figure 4-49: Munk moment test 2, w	103
Figure 4-50: Munk moment test 2, roll.....	103
Figure 4-51: Munk moment test 2, pitch	103
Figure 4-52: Munk moment test 2, yaw	103
Figure 4-53: Satellite image of Rutherford Park[49]	105
Figure 4-54: PID validation, NE trajectory.....	107
Figure 4-55: PID validation, roll angle	107
Figure 4-56: PID validation, pitch angle.....	107
Figure 4-57: PID validation, yaw angle	107
Figure 4-58: PID validation, forward velocity.....	108
Figure 4-59: PID validation, height	108
Figure 4-60: PID validation, wind speed	108
Figure 4-61: PID validation, wind direction	108
Figure 4-62: HLC validation, 3D trajectory.....	109
Figure 4-63: HLC validation, NE trajectory	109
Figure 4-64: HLC validation, pitch angle	110
Figure 4-65: HLC validation, yaw angle	110
Figure 4-66: HLC validation, forward velocity	110
Figure 4-67: HLC validation, inertial height	110
Figure 4-68: HLC validation, wind speed.....	110
Figure 4-69: HLC validation, wind direction.....	110

Figure A-1: Experimental setup for measuring thrust and reaction torques. Figure from [8].....	122
Figure C-1: Reynolds number along the entire length of the airship for $r = 120^\circ/s$..	126
Figure C-2: Span-wise drag variation for a cylinder of aspect ratio 4.....	127
Figure C-3: Cross-flow around a low aspect ratio cylinder with two free-ends [54]. ..	127
Figure C-4: Drag coefficient along airship length.	128
Figure D-1: Measured and estimated reaction torques for 6 different command inputs.	131
Figure D-2: Measured and estimated reaction torques for 6 different command inputs. Details of rise and fall.	132
Figure E-1: Inertial height during drop test – Test case B	133
Figure E-2: Downward velocity during drop test – Test case B.....	133
Figure E-3: Inertial height during drop test – Test case C	133
Figure E-4: Downward velocity during drop test – Test case C.....	133
Figure F-1: Total thrust in x , test case A	134
Figure F-2: Forward velocity, test case A.....	134
Figure F-3: Total thrust in x , test case B	134
Figure F-4: Forward velocity, test case B.....	134
Figure F-5: Total thrust in x , test Case C.....	135
Figure F-6: Forward velocity, test case C	135
Figure F-7: Total thrust in x , test case D	135
Figure F-8: Forward velocity, test case D.....	135
Figure F-9: Total thrust in x , test case E.....	135
Figure F-10: Forward Velocity, test case E	135
Figure F-11: Total thrust in x , test case F.....	136
Figure F-12: Forward velocity, test case F	136
Figure G-1: Commanded thrusts in x -direction (top) and forward acceleration (bottom) – Forward acceleration test : test case 2.....	137
Figure G-2: Commanded thrusts in x -direction (top) and forward acceleration (bottom) – Forward acceleration test : test case 3.....	137
Figure G-3: Commanded thrusts in x -direction (top) and forward acceleration (bottom) – Forward acceleration test : test case 4.....	138

Chapter 1 Introduction

1.1 Background

Lighter-than-air-vehicles (LTAVs) can be divided into two types: balloons and airships. Both generate lift by virtue of a lifting gas, but airships are also equipped with propellers and control surfaces to maneuver them through air. In the early airships, hot air was the prime choice for the lifting gas. This was eventually replaced by hydrogen. Finally, helium became the most common lifting gas owing to its higher lifting capabilities than hot air, and lower volatility than hydrogen [1].

The design of the first modern-day airship hull (Figure 1-1) is credited to Jean Baptiste Meusnier, who in 1784 proposed a slender near-ellipsoidal hull shape, with three airscrew propellers and a rudder on the aft for steering; all to overcome the maneuverability issues of an earlier design [1]. The late 19th and early 20th century then saw a surge in airship development alongside the developments in engine technology and a better understanding of aerodynamic stability. The Golden age of airships is considered to be between the start of the 20th century until the era of *The Hindenburg* (LZ-129) airship by the Zeppelin Corporation[2] (Figure 1-2).

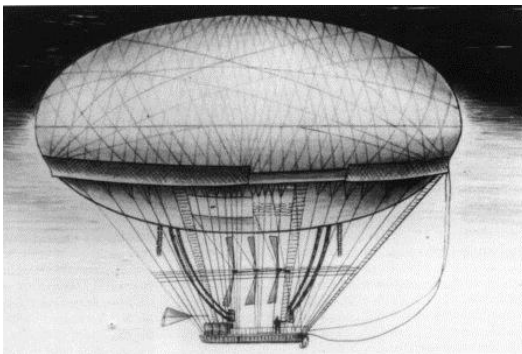


Figure 1-1: Meusnier's *Dirigible* [3].

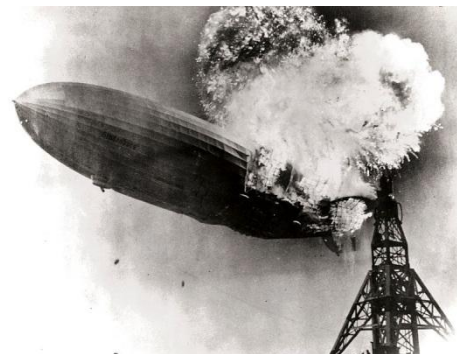


Figure 1-2: The Hindenburg (LZ-129) right after it burst into flames [4].

The Hindenburg met with a disaster, as it burst into flames on 6 May, 1937, minutes before landing. This shattered public confidence in airship travel, and brought an end to the golden age of airships.

More recently, with the growing costs of fuel and the many advances in material engineering, one can see a rising interest in airship technology. This is mainly because airships offer long endurance and low operating cost platforms as compared to other aerial vehicles. Moreover, modern designs are addressing the shortcomings of the conventional airship designs, especially with respect to poor handling at low speeds, ground handling and maneuverability. The modern airship designs overcome the limitations of conventional airship designs by employing specific techniques. Low-speed maneuverability and handling, which is mainly due to the conventional airship's reliance on aerodynamic control surfaces for steering and stability, are achieved by use of vectored thrusters. Another limitation of the conventional design is the issue of ground handling i.e. ensuring safe take-off and landing for the airship, which may require a large ground-crew. This can be tackled if an airship can provide Vertical/Short Take-Off and Landing (V/STOL) [5-7].



Figure 1-3: The hybrid LEMV concept [6]



Figure 1-4: The Solar Ship [7]

The US Army alongside Northrop Grumman, for example, is now developing the hybrid Long-Endurance Multi-intelligence Vehicle (LEMV) (Figure 1-3). A Canadian venture,

the *Solar Ship* (Figure 1-4) attempts to go even further with respect to energy-efficiency by covering its hull with solar cells to power the electric motors.

1.1.1 The Mk-II ALTAV

The Mk-II ALTAV (Almost-Lighter-Than-Air-Vehicle) (Figure 1-5), originally developed by Quanser Inc., is a novel airship that seeks to overcome the performance limitations of conventional designs – especially with respect to maneuverability. The airship is *almost* lighter than air, meaning that it is slightly negatively buoyant. This arrangement allows the airship to slowly fall back to ground in case of thruster- or communications-failure rather than drifting away with the wind. This also has an impact on the size of the airship envelope, which is reduced, since the airship can now derive some of its lift from the thrusters, thereby reducing its drag.



Figure 1-5: The Mk-II ALTAV [8]

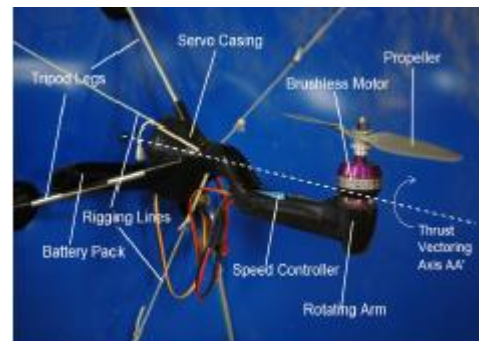


Figure 1-6: Thruster arrangement [8]

The airship hull is a slender-shaped near-ellipsoidal polymer hull. The airship spans around 4.8 m in length with a maximum diameter of about 1.5 m . Thus, its fineness ratio, which is the ratio of its length to its maximum diameter, is about 3.2.

The most unique feature of the Mk-II is its lack of any passive stabilizers, i.e., horizontal and vertical fins. This allows the Mk-II an improved maneuverability but compromises its inherent stability. As a result, a feedback controller on-board ensures artificial/active

stability during flight. The controller outputs are provided to the four vectoring thrusters that are mounted along the equator of the airship hull. Each thruster (Figure 1-6) has three legs that are attached to the airship hull by means of Velcro pads at the bottom of each leg. Each thruster is further secured to the hull by means of three strings. A 12'' \times 3.8'' propeller is mounted on a DC brushless motor to provide thrust. A servo tilts the motor housing, allowing the thrust to be vectored between $\pm 90^\circ$ from the vertical.

The goal is to make the Mk-II a fully autonomous vehicle with minimal intervention on the part of the human operator. It is equipped with a Global Positioning System (GPS), an Inertial Measurement Unit (IMU) and sonar for state-feedback. An off-board ground-station displays critical airship information and logs time histories of airship variables.

1.1.2 Thesis Motivation and Objectives

A first dynamics model of the airship was developed by Peddiraju [8]. Although that model functions well, it does warrant some improvements with respect to certain phenomena that were not taken into account. Specifically, these are the rotational damping moments acting on the hull, the drag due to protuberances, the thrusters' gyroscopic effects and the thrusters' reaction torques.

A second objective of this thesis is to design a high-level controller for autonomous airship guidance along predefined mission paths. Given the airship's relative size, it is highly prone to winds. Thus, a guidance algorithm maintains good airship performance in the presence of winds will be developed.

The third and final objective of this thesis is to perform flight tests for two reasons. Firstly, results of these flight tests will be used to experimentally validate certain physical

parameters of the airship that were theoretically estimated. Secondly, the flight tests will validate the performance of the controller-suite in the presence of winds.

1.2 Literature Review

1.2.1 Rotational Damping Moments Estimation

The rotational damping moments, which are the moments produced during rotational motion of a vehicle, are not much studied in the dynamics of aerial vehicles due to their negligible effect, since most vehicles spend most of their time in cruise with very low angular rates. Even when these effects are included, they are considered for vehicles at low angles-of-attack such as in [9-11] . For example, in [9] methods are presented for estimating the non-dimensional rotational damping coefficient with a derivation based on the static pitching/yawing moment coefficients. This approach is valid as long as the angle-of-attack remains small (while this has not been explicitly mentioned in [9], it is implied within the discussion). Another method for obtaining the rotational damping moments, applicable to a slender body but limited in application to very slow rotational motion, is presented by Tobak and Reese[12]. All the above methods have been derived for vehicles that are in high-velocity cruise flight at low angles-of-attack. This is because an important feature of high-velocity cruise flight is that during changes in the vehicle attitude (mostly heading), the forward velocity of the vehicle remains nearly constant. Thus, when these vehicles incur rotational motions, they interact with a flow dominated by potential flow theory [13] over the vehicle body which produces the damping moment. In slow-moving vehicles, changes in the attitude during flight may produce large perturbations in the velocity profiles. Only a limited body of literature exists for

estimation of the rotational damping moments on slow-moving vehicles. One approach is based on an assumption of pure rotation as in [14]. Georgiades[14] calculates this net moment, by breaking down a rectangular prism shaped robot into differential elements, calculating the damping moment about the center of mass due to each element under rotations and then integrating these differential moments over the length of the body. The damping moment is calculated based on a purely viscous flow assumption, which is likely for a bluff body. Although this method may give a reasonable estimate of the damping moments for pure rotational motions, and thus for bodies that are slow-moving, it is not applicable for high velocity vehicles for reasons mentioned in the previous paragraph.

1.2.2 Protuberance Drag

Protuberances are the various appendages protruding from the main streamlined hull. For an airplane fuselage, these may be the fuselage canopy that houses the pilot, the gun-turrets for military aircraft or even the various bolts and rivet-heads on the fuselage surface [15]. On airships the major protuberances are the gondola and the engine assemblies that are attached on the surface of the streamlined hull [16].

Large sets of empirical data exists for calculating protuberance drag on general shapes, such as plates, cuboids, rods, etc. [15, 17, 18]. These data sets were created from wind tunnel tests on simple shapes attached to a flat wall. The data sets are of two categories depending on whether or not the protuberance is ‘immersed’ in the turbulent boundary layer. Approximate methods for calculating the boundary layer thickness along the hull profile are also provided. For non-general shapes of protuberances, researchers have

relied on wind tunnel testing for estimating these drags quantitatively such as in [16]. Furthermore, specifically for airships, researchers have estimated the added drag due to the presence of the gondola and Dorrington [19] provides a summary for some of these results. For vehicles such as the ‘SSC’ and ‘ZMC-2 form’ with aspect ratios comparable to the Mk-II ALTAV the axial drag of the overall vehicle due to the presence of the gondola is increased by 34.5 % and 33.3 % , respectively.

1.2.3 Reaction Torques

Reaction torques are an important effect to model for propeller-based aerial vehicles. A major portion of the reaction torques is due to the aerodynamic drag experienced by the propeller, while another component arises as an inertial reaction due to changes in the rotor-propeller velocities. On airplanes, where the propeller’s spin axis is along the longitudinal body frame axis, these torques result in moments about the roll-axis [20]. On helicopters, the reaction torques due to the main rotor’s spin tend to produce a yawing moment, which is countered by the tail rotor [21]. Most modern UAV’s rely on more than one propeller-motor assembly (thruster) to generate maneuvering forces and the placement and spin-direction of these thrusters determines whether or not the reaction torques are significant. When all the thrusters spin in the same direction and/or each thruster operates exclusive of the other thruster (such as in the Mk-II ALTAV), these torques can collectively become important and must be modeled. However, for the quadrotor modeled in [22, 23], the four thrusters are placed on the same horizontal plane and the adjacent pairs are always counter rotating. Thus, the aerodynamic reaction torques cancel and are neglected.

For a tilt-rotor UAV, Amiri et al. [24] use a quadratic relationship between the aerodynamic reaction torque Q and the propeller speed ω as $Q = C_Q \omega^2$ where C_Q is a constant of proportionality. Goel et al. [25] arrive at the same result for a quadrotor for modeling these torques but present an analytical approach to estimate C_Q using momentum theory [21] which requires a knowledge of the physical parameters of the propeller. Distinct from the aerodynamic torque, the inertial counter torque is modeled based on the product between the moment of inertia of the rotating parts and their spin-accelerations [22]-[25].

1.2.4 Thruster Gyroscopic Moments

Gyroscopic moments have been discussed in literature for vehicles with a fixed propeller-engine assembly such as in airplanes by Etkin [20] and in quad-rotors by BouAbdullah [22] and Goel et al. [25]. The gyroscopic moments on the vehicle due to the spinning propeller assembly in these vehicles are a result of the coupling between the vehicle's body rotations and the propeller's spin. Vehicles with articulated thrusters (also known as tilt rotors) present a more complex dynamics problem in which the thrusters' vectoring lead to the generation of additional gyroscopic moments. Miller and Narkiewicz [26] have attempted to provide a dynamics representation of a tilt rotor for the V-22 Osprey. In this work, they take into account the moment of inertia of the nacelles, the engine, and the propellers to model the gyroscopic effects due to their large size. In smaller vehicles with articulated thrusters, the nacelles are less important, and the derivation becomes simpler, as in the tilt rotor model developed by Paparichtos et al.[27].

1.2.5 Autonomous Vehicle Guidance

The objective of the guidance problem is to formulate a real-time algorithm that allows the vehicle to track a predefined path [28]. This predefined path could be a general three dimensional curve, either generated by a path planning algorithm or defined manually by the user, according to the vehicle's mission objectives. Ideally, convergence onto the desired path should be guaranteed for a large set of initial conditions that would include the vehicle's position, attitude and velocity.

Usually, a guidance algorithm is implemented on a vehicle in the form of a high-level controller. This means that a guidance algorithm calculates the desired states that would guide a vehicle along the prescribed path, based on geometric or dynamic relationships between vehicle state and prescribed path. These desired states are then fed to a low-level controller (such as a PID controller), which tracks the desired states generated by the high-level controller. Some researchers have attempted to combine these two controllers into one [29, 30], or more specifically for airships [31, 32], thereby reducing the overall complexity of the controller architecture. Although this method simplifies the guidance problem, it gives designers less flexibility when making design changes to either controller.

Another major factor to account for while designing a guidance algorithm for a vehicle is the external disturbances, such as ambient winds. For micro-UAV's, Osborne and Rysdyk [33] propose a guidance algorithm, the objective of which is to minimize the cross-track error in the horizontal plane between the vehicle and the desired track. The same guidance method was then tested on a miniature-UAV by Nelson et al.[34] and

showed good wind handling abilities. The method currently exists only for 2-dimensional horizontal guidance.

1.3 Thesis Organization

This thesis is divided into three parts. The first part, documented in Chapter 2 presents improvements that have been made to the existing dynamics model of the Mk-II ALTAV developed by Peddiraju [8]. Next, in Chapter 3 a closed-loop controller suite developed for the airship is described. The low-level part of this controller was developed in [8]. A high-level controller (guidance algorithm) that was previously used on an underwater vehicle is then implemented and tested in simulation on the Mk-II ALTAV and its performance is discussed. This leads to the development of a more advanced high-level controller for the airship with superior performance in windy conditions. Next, in Chapter 4, flight tests are performed with three objectives: 1) experimental validation of certain physical parameters of the airship, 2) experimental validation of the low-level controller and, 3) experimental validation of the overall controller suite for autonomous guidance. Finally, Chapter 5 concludes and summarizes the work presented in the previous chapters, and recommendations are made for future work.

Chapter 2 Improvements to the Current Airship Model

This chapter deals with improvements made to the existing dynamics model of the MkII airship. One of the major goals of this development is to have a more comprehensive dynamics model to better predict airship performance. In particular, the effects modeled in this chapter are the aerodynamic rotational damping of the hull, the modified axial drag due to protuberances on the airship hull, and two additions to the thruster: the gyroscopic moments of the thrusters and the reaction torques of the rotating thrusters.

2.1 Existing Dynamics Model

This section describes the non-linear dynamics model of the Mk-II ALTAV as derived and implemented by Peddiraju[8], as an understanding of the existing airship model is needed to allow an understanding of the current thesis.

2.1.1 Relevant Frame Transformations

The airship (See Figure 2-1) is treated as a rigid body. It has 6 degrees of freedom: 3 translational (surge, sway and heave) and 3 rotational (roll, pitch and yaw). The *NED* frame (North-East-Down) is the geographic inertial reference frame with its X axis pointing north, Y axis pointing east and Z axis pointing downwards towards the center of the earth. The body-frame (*xyz*) is fixed to the airship with its origin at the center of buoyancy. Its *x*-axis points towards the nose, *y*-axis points out the right side and the *z*-axis points downwards.

A vector expressed in the *NED* frame can then be transformed into the body frame by employing a *Z-Y-X body-fixed rotation sequence* using the three Euler angles yaw (ψ), pitch (θ) and roll (ϕ) according to standard aeronautical convention [20].

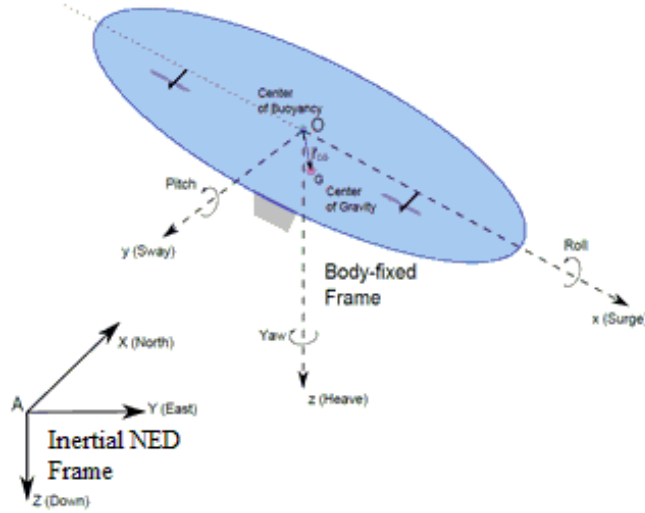


Figure 2-1: The inertial NED frame and the airship body frame [8]

Using short-hand notations for $\sin(\cdot)$ and $\cos(\cdot)$ as $s_{(\cdot)}$ and $c_{(\cdot)}$ respectively, the resulting rotation matrix that would transform a vector from the inertial frame to the body frame $\mathbf{R}_{i \rightarrow b}$ is given by:

$$\mathbf{R}_{i \rightarrow b} = \mathbf{R}_Z(\psi)\mathbf{R}_Y(\theta)\mathbf{R}_X(\phi) = \begin{bmatrix} c_\theta c_\psi & c_\theta s_\psi & -s_\theta \\ s_\theta s_\phi c_\psi - c_\phi s_\psi & s_\theta s_\phi s_\psi + c_\phi c_\psi & s_\phi c_\theta \\ c_\phi s_\theta c_\psi + s_\phi s_\psi & c_\phi s_\theta s_\psi - s_\phi c_\psi & c_\theta c_\psi \end{bmatrix} \quad (2.1)$$

A second frame relevant to the derivations in Sections 2.3.3 and 2.3.4 is the *thruster frame* ($O_t x_t y_t z_t$). This frame is attached to the thrusters in such a way that it rotates with the servo rotations (See Figure 2-2). Its origin O_t is at the point of intersection of the axis of the motor-propeller rotation (along x_t) and the servo rotation (along y_t). All four

thrusters spin in the counter-clockwise direction viewed from top. The thrusters are numbered 1, 2, 3 and 4 in a clockwise sequence, viewed from above, with the front right thruster being thruster 1. The rotation matrix $\mathbf{R}_{t \rightarrow b}$ which transforms vectors from the thruster frame to the body frame can be found as:

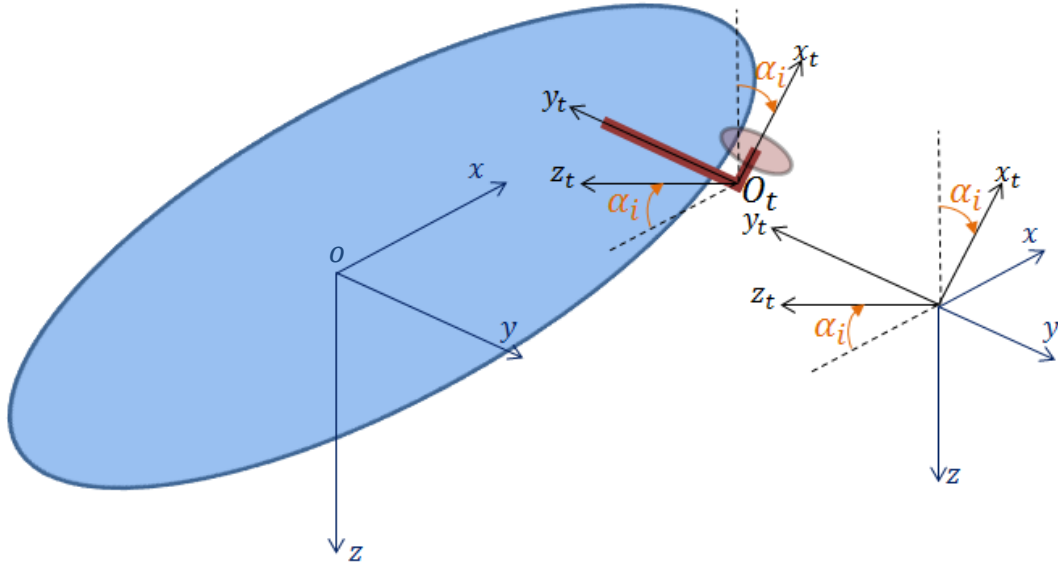


Figure 2-2: The thruster frame and the body frame

$$\mathbf{R}_{t \rightarrow b} = \begin{bmatrix} \sin(\alpha) & 0 & -\cos(\alpha) \\ 0 & -1 & 0 \\ -\cos(\alpha) & 0 & -\sin(\alpha) \end{bmatrix} \quad (2.2)$$

Since each of the four servos, at any given instant, has a unique position α_i , the rotation matrices for each will be denoted with a subscript i such as $(\mathbf{R}_{t \rightarrow b})_i$

2.1.2 Airship Dynamics – Equations of Motion

The dynamics model used by Peddiraju [8] included the following external forces and moments acting on the airship: aerodynamic viscous drag, added mass, wind, thruster, gravitational and buoyancy effects. The non-linear equations of motion for the airship are

derived using Newton's second law and Euler's equation, leading to the following translational and rotational equations, expressed in the body frame:

$$\begin{bmatrix} \dot{\mathbf{v}} \\ \dot{\boldsymbol{\omega}} \end{bmatrix} = \bar{\mathbf{M}}_a^{-1} \begin{bmatrix} \boldsymbol{\omega}^\times \mathbf{M}_a \mathbf{v} + m \boldsymbol{\omega}^\times \mathbf{r}_{CG}^\times \boldsymbol{\omega} + \boldsymbol{\omega}^\times \mathbf{M}_{D_a} \mathbf{v}_w - \mathbf{M}_{D_a} \boldsymbol{\omega}^\times \mathbf{v}_w + \mathbf{M}_{D_a} \dot{\mathbf{v}}_w + \mathbf{f}_v + \mathbf{f}_T + \mathbf{f}_G \\ -m \mathbf{r}_{CG}^\times \boldsymbol{\omega}^\times \mathbf{v} - \boldsymbol{\omega}^\times \mathbf{J}_a \boldsymbol{\omega} - (\mathbf{v} - \mathbf{v}_w) \times \mathbf{M}_{D_a} (\mathbf{v} - \mathbf{v}_w) + \mathbf{n}_v + \mathbf{n}_T + \mathbf{n}_G \end{bmatrix} \quad (2.3)$$

where the left-hand side represents the resulting inertial accelerations $[\dot{\mathbf{v}}^T \quad \dot{\boldsymbol{\omega}}^T]^T$ due to the applied force and moment terms on the right-hand side of the same equation. The vector $\dot{\mathbf{v}} = [\dot{u} \quad \dot{v} \quad \dot{w}]^T$ represents the translational acceleration of the center of buoyancy of the airship, while $\dot{\boldsymbol{\omega}} = [\dot{p} \quad \dot{q} \quad \dot{r}]^T$ represents the rotational acceleration of the airship. Both these vectors are expressed in the body frame. $\bar{\mathbf{M}}_a$ is the apparent mass matrix which includes the true and added mass and inertias of the airship as given below:

$$\bar{\mathbf{M}}_a = \begin{bmatrix} m \mathbf{I}_e + \mathbf{A}_m & -m \mathbf{r}_{CG}^\times \\ m \mathbf{r}_{CG}^\times & \mathbf{J} + \mathbf{A}_J \end{bmatrix} \quad (2.4)$$

where $\bar{\mathbf{M}}_a$ is of dimension 6×6 . The total true mass of the airship is m , including all its components and the mass of the enclosed helium while \mathbf{I}_e is the 3×3 identity matrix. The matrix \mathbf{J} represents the true inertia matrix of the airship, while \mathbf{A}_m and \mathbf{A}_J are the added mass and inertia matrices, respectively. For the axisymmetric airship hull the latter terms are given as:

$$\mathbf{A}_m = \begin{bmatrix} m_{11} & 0 & 0 \\ 0 & m_{22} & 0 \\ 0 & 0 & m_{22} \end{bmatrix} \quad \mathbf{A}_J = \begin{bmatrix} 0 & 0 & 0 \\ 0 & m_{33} & 0 \\ 0 & 0 & m_{33} \end{bmatrix} \quad (2.5)$$

where, m_{11} is the added mass of the airship hull along the longitudinal x -axis, m_{22} is the added mass along the transverse y and z -axes, while m_{33} is the added inertia about the y

and z -axes. Moreover, $m_{11} = k_1 m_D$, $m_{22} = k_2 m_D$ and $m_{33} = k_3 I_D$, where k_1 and k_2 are added mass factors and k_3 is the added inertia factor, all of which depend on the fineness ratio of the hull, as shown in Figure 2-3. Finally, m_D and I_D are the mass and moment of inertia of the air displaced by the airship, respectively.

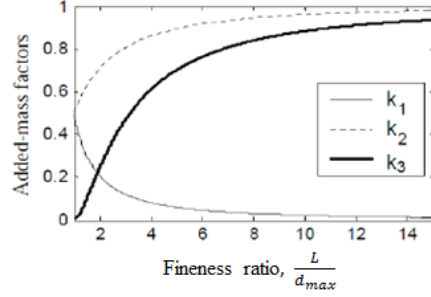


Figure 2-3: Added mass and inertia factors versus fineness ratio [35]

The symbol \mathbf{r}_{CG}^\times represents the skew-symmetric matrix¹ of the position vector of the center of gravity \mathbf{r}_{CG} expressed in the body frame.

The right hand side of Equation (2.3), when not multiplied by $\bar{\mathbf{M}}_a^{-1}$, represents the sum of the applied forces and moments acting on the airship expressed in the body frame. The terms $\boldsymbol{\omega}^\times \mathbf{M}_a \mathbf{v} + m \boldsymbol{\omega}^\times \mathbf{r}_{CG}^\times \boldsymbol{\omega}$ represent the inertial effects in translational motion, while $-m \mathbf{r}_{CG}^\times \boldsymbol{\omega}^\times \mathbf{v} - \boldsymbol{\omega}^\times \mathbf{J}_a \boldsymbol{\omega}$ represent these effects in rotational motion. Vectors \mathbf{v}_w and $\dot{\mathbf{v}}_w$ represent the wind velocity and wind acceleration, respectively, and so the effect of the forces due to coupling between wind and added mass is given by the terms $\boldsymbol{\omega}^\times \mathbf{M}_{D_a} \mathbf{v}_w - \mathbf{M}_{D_a} \boldsymbol{\omega}^\times \mathbf{v}_w + \mathbf{M}_{D_a} \dot{\mathbf{v}}_w$. The apparent *displaced mass* matrix \mathbf{M}_{D_a} is given by:

$$\mathbf{M}_{D_a} = m_D \mathbf{I}_e + \mathbf{A}_m \quad (2.6)$$

An important phenomenon relevant to bodies with slender shapes is the Munk moment given by the term $-(\mathbf{v} - \mathbf{v}_w) \times \mathbf{M}_{D_a} (\mathbf{v} - \mathbf{v}_w)$. It is based on the airspeed of the vehicle

¹ The skew-symmetric matrix \mathbf{a}^\times of a vector \mathbf{a} , multiplied by a vector \mathbf{b} , is used to express the cross-product $\mathbf{a} \times \mathbf{b}$.

$\mathbf{v} - \mathbf{v}_w$ and is destabilizing in nature such that it tends to orient the longitudinal x -axis of the airship perpendicular to the airspeed vector. That orientation is the stable equilibrium for the airship, in contrast to the nose pointing forward into the wind (when \mathbf{v} and \mathbf{v}_w are parallel) which is an unstable equilibrium.

The combined effects of buoyancy and gravity are given by \mathbf{f}_G and \mathbf{n}_G while the terms \mathbf{f}_v and \mathbf{n}_v represent the force and moment due to the aerodynamic viscous drag on the airship hull. The terms \mathbf{f}_T and \mathbf{n}_T are the total force and moment exerted by the thrusters

2.2 Improvements to the Dynamics Model

An accurate dynamics model of the airship can save field testing time since one is able to predict airship behaviour in advance. As such, it is desirable to improve the existing dynamics model by modeling additional effects not accounted for in Peddiraju[8].

In this chapter, we will modify three of the terms in Equation (2.3) (\mathbf{n}_v , \mathbf{f}_v and \mathbf{n}_T) to account for the rotational damping moments, the added drag due to protuberances, the gyroscopic moments and the thruster reaction torques.

The thrust moment will be modified to:

$$\mathbf{n}'_T = \mathbf{n}_T + \mathbf{n}_Q + \mathbf{n}_M \quad (2.7)$$

where \mathbf{n}_Q and \mathbf{n}_M represent contributions due to thruster reaction torques and thruster gyroscopic effects, respectively. The viscous moment will be modified to:

$$\mathbf{n}'_v = \mathbf{n}_v + \mathbf{n}_\omega \quad (2.8)$$

where \mathbf{n}_ω represents the rotational damping moment. Finally, the viscous force will be modified to

$$\mathbf{f}'_v = \mathbf{f}_v + \mathbf{f}_p \quad (2.9)$$

where \mathbf{f}_p represents the added drag due to protuberances. Equation (2.3) can now be written as:

$$\begin{bmatrix} \dot{\mathbf{v}} \\ \dot{\boldsymbol{\omega}} \end{bmatrix} = \bar{\mathbf{M}}_a^{-1} \begin{bmatrix} \boldsymbol{\omega}^\times \mathbf{M}_a \mathbf{v} + m \boldsymbol{\omega}^\times \mathbf{r}_{CG}^\times \boldsymbol{\omega} + \boldsymbol{\omega}^\times \mathbf{M}_{D_a} \mathbf{v}_w - \mathbf{M}_{D_a} \boldsymbol{\omega}^\times \mathbf{v}_w + \mathbf{M}_{D_a} \dot{\mathbf{v}}_w + \mathbf{f}'_v + \mathbf{f}_T + \mathbf{f}_G \\ -m \mathbf{r}_{CG}^\times \boldsymbol{\omega}^\times \mathbf{v} - \boldsymbol{\omega}^\times \mathbf{J}_a \boldsymbol{\omega} - (\mathbf{v} - \mathbf{v}_w) \times \mathbf{M}_{D_a} (\mathbf{v} - \mathbf{v}_w) + \mathbf{n}'_v + \mathbf{n}'_T + \mathbf{n}_G \end{bmatrix} \quad (2.10)$$

2.2.1 Theoretical Estimation of Rotational Damping Moments

In this section, we derive a method to evaluate the rotational damping moments acting on the airship \mathbf{n}_ω due to rotational rates about the transverse axes y and z . It is assumed here that there are no damping moments associated with the longitudinal axis x , since the airship has minimal resistance to roll motions. Moreover, it was found from test flights that roll rates are typically a factor of five less than pitch and yaw rates.

As discussed in Section 1.2.1, the rotational damping moments are often neglected when modeling air vehicles. Even when they are modeled, only the contribution from the flow described by the potential flow theory is taken into account. This is justifiable since the vehicles considered operate mostly in cruise flight. The Mk-II ALTAV, however, is a highly maneuverable vehicle that can undergo large pitch and yaw rates at relatively low forward speed. Therefore the flow around the airship is complex and includes both potential flow and viscous flow effects, making the damping moments estimation a difficult task. The potential flow contributions were estimated for our airship using a

method presented by Tobak and Reese [12] and it was found that these moments were very small. In order to model the forces, a method analogous to that used by Georgiades [14] was followed. This method only predicts the damping moments of a body under pure rotation (viscous effects dominant), as we were unable to find a more comprehensive approach in the literature.

The airship has a circular cross-section normal to and along its longitudinal axis, as shown in Figure 2-4. As shown in Figure 2-5, the airship can be considered to be composed of cylindrical disc elements of width dx . Because the approach used to quantify the pitch and yaw damping is based on the cross-flow drag of cylindrical elements across the airship length, it is important to have a drag model $C_d(x)$ along the span-wise length of the airship. This is discussed in Appendix C.

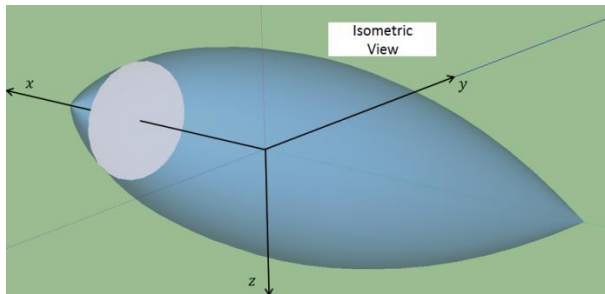


Figure 2-4: Airship with circular cross-section

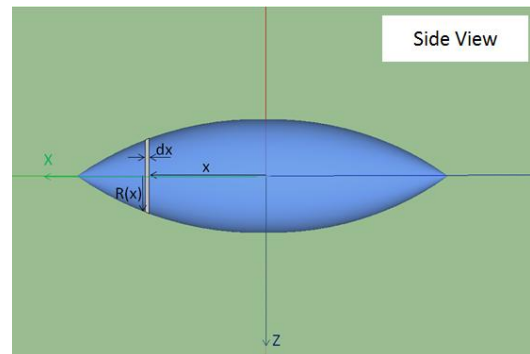


Figure 2-5: Differential disc element at a distance x from the center of buoyancy

We begin by finding the differential drag experienced by a differential disc element located on the longitudinal x -axis with its center at x (See Figure 2-5) while the airship undergoes a pure rotation about its transverse axes of $\hat{\omega} = [0 \quad q \quad r]^T$. The moment due to each differential drag will then be calculated and the total moment acting on the airship will be considered to be composed of the sum of these differential drags.

The area of the disc that will be exposed to the fluid during rotation is $dS(x) = 2R(x)dx$, where $R(x)$ is the radius of the circular cross section at station x .

Since the airship is considered to undergo pure rotation about the origin of the body frame, the velocity of the center of the differential disc element on the x -axis is given by:

$$\mathbf{v} = \hat{\boldsymbol{\omega}} \times \mathbf{r}_x = [0 \quad rx \quad -qx]^T \quad (2.11)$$

The magnitude of this velocity is $\|\mathbf{v}\| = v = (\sqrt{q^2 + r^2})x = \hat{\omega}x$ where $\hat{\omega} = \sqrt{q^2 + r^2}$.

If $C_d(x)$ is the drag of the cylinder at body station x , the differential drag $dD_r(x)$ on the disc element at station x due to $\hat{\omega}$ is thus given by:

$$dD_r(x) = \frac{1}{2} \rho C_d(x) (\hat{\omega}x)^2 dS(x) = \rho C_d(x) (\hat{\omega}x)^2 R(x) dx \quad (2.12)$$

The differential moment $dM_{D,r}$ is now given by:

$$dM_{D,r} = |x| dD_r \quad (2.13)$$

The total moment about the pitching moment center due to all disc elements along the airship length can now be found by integrating Equation (2.13) over $x \in [x_m, -(L - x_m)]$ resulting in:

$$M_D = k_\omega \hat{\omega}^2 \quad (2.14)$$

where

$$k_\omega = \rho \left(\int_{x_m}^{-(L-x_m)} |x| x^2 C_d(x) R(x) dx \right) \quad (2.15)$$

and the positive coefficient k_ω is defined as the rotational damping coefficient. As will be seen in Section 2.4, $R(x)$ in Equation (2.15) was approximated as an 8th order polynomial (Equation (2.39)). Using Equation (2.39) for $R(x)$, and the span-wise drag model $C_d(x)$ derived in Appendix C, we can integrate Equation (2.15) to find $k_\omega \approx 4.42 \frac{Nm}{(rad/s)^2}$.

Knowing that M_D always acts opposite to the direction of $\hat{\omega}$, we can now express the damping moment in the body-frame \mathbf{n}_ω as:

$$\mathbf{n}_\omega = \begin{bmatrix} 0 \\ \frac{M_D q}{\sqrt{q^2 + r^2}} \\ -\frac{M_D r}{\sqrt{q^2 + r^2}} \end{bmatrix} = \begin{bmatrix} 0 \\ -k_\omega q \hat{\omega} \\ -k_\omega r \hat{\omega} \end{bmatrix} \quad (2.16)$$

2.2.2 Effect of Protuberances on the Axial Drag Coefficient

The presence of attachments and appendages (collectively called protuberances) on the airship hull during forward flight can lead to a higher axial drag coefficient than the airship hull alone. We thus investigate the modified drag due to protuberances on the airship. These protuberances are the gondola, the GPS antenna and the thruster legs. The thruster body is not included in this analysis because its drag is dominated by propwash from the propellers. The thruster forces were modeled based on experimental measurements by Peddiraju [8], and this experiment was set up so that the stand holding the thrusters nearly emulates the thruster body. Thus, we assume that this drag force has already been accounted for in the thruster model. (See Appendix A).

Semi empirical methods based on the data available for drag on bodies of similar shapes, found in [15, 17, 18], are used to estimate the drag due to protuberances. To use the data in these references, one must know whether the protuberance is ‘immersed’ in the local

boundary layer or if it lies beyond it, in the free-stream region. This measure is given by the ratio $\gamma = h/\delta$, where h is the height of the protuberance above the surface and δ is the boundary layer thickness. From [15], the boundary layer thickness can be found approximately as a function of the distance from the nose x' as:

$$\delta = 0.02x' \quad (2.17)$$

In the following sections, we will estimate the drag due to the gondola $C_{A_{gondola}}$, the GPS antenna $C_{A_{ant}}$ and the 12 thruster legs $C_{A_{leg}}$ such that the resulting overall drag of the airship in the axial direction, at zero angle of attack, will be given as:

$$C_{A_0} = C_{A_{hull}} + C_{A_{gondola}} + C_{A_{ant}} + C_{A_{leg}} \quad (2.18)$$

where the right-hand side, multiplied by the dynamic pressure and the reference frontal area A_f yield the term f_p in Equation (2.9).

2.2.2.1 Gondola and GPS

Based on their geometry, the gondola and the GPS (shown in Figure 2-6) antenna are first approximated as rectangular prisms. Table 2-1 lists the approximate dimensions for the gondola and the GPS antenna (in meters) and the relevant parameters used in the estimation of the drag coefficient. The width w is the dimension of the protuberance across the flow, while the length l is the dimension along the flow.

Table 2-1: Gondola and GPS Antenna dimensions (in meters)

Protuberance	Width, w	Height, h	Length, l	x'	δ	γ
Gondola	0.135	0.135	0.27	2.20	0.044	3.068
GPS Antenna	0.013	0.013	0.05	2.20	0.044	0.295



Figure 2-6: Gondola and on-board GPS antenna

From the above two values of γ , it is clear that the gondola lies mostly in the free stream region ($\gamma > 1$) beyond the boundary layer, while the GPS antenna is immersed in the boundary layer ($\gamma < 1$).

Akins and Peterka [18] have experimentally measured the drag on various rectangular prism bodies attached to a flat plate. It was found in [18] that for bodies of this shape, that are *not immersed* in the boundary layer but lie in the free-stream region, the mean drag depends on the ratio $\frac{w}{l}$ of the body, and they tabulated data in [18] for bodies of different $\frac{w}{l}$ ratios. For the rectangular prism approximation for our gondola, from Table 2-1, this ratio is 0.5. Therefore, the axial drag coefficient of the gondola based on the frontal area of the airship hull A_f from the data in Table 1 and Fig. 6 in [18] is calculated as $C_{A_{gondola}} = 0.015$.

From [15], the axial drag coefficient of a body *immersed* in the boundary layer can be given as a function of γ . Thus, the drag to due the GPS antenna, based on the frontal area of the airship hull A_f , can be found using [15]:

$$C_{A_{ant}} = (0.75\sqrt{\gamma}C_{d_o}) \frac{hw}{A_f} \quad (2.19)$$

where, C_{d_o} is the independent drag coefficient for a square plate. Note that the factor $\frac{hw}{A_f}$ has been appended to the original equation to non-dimensionalize $C_{A_{ant}}$ with respect to the frontal area of the airship. From the information in [15], $C_{d_o} \approx 0.55$ for a square-plate of

height 1.3 cm based on the area subjected to the oncoming flow. Therefore, $C_{A_{ant}} = 0.000022$.

2.2.2.2 Thruster legs

The thruster legs are long, slender rods of diameter D_l and length L_l each. Due to their length compared to the local boundary layer thickness, it is assumed that the thrusters lie almost entirely in the free-stream region. There are three legs for each thruster securing it to the airship hull. The drag in the axial direction can be estimated based on data provided in Table 10-19 in [17] for a long rod inclined to the flow. Based on the inclination of each thruster leg θ_l (See Figure 2-7) its normal and tangential drag coefficients C_N and C_T , based on the frontal area of the airship A_f , can be given as in Table 2-2 where c_{θ_l} and s_{θ_l} are short-hand notations for $\cos \theta_l$ and $\sin \theta_l$ respectively.

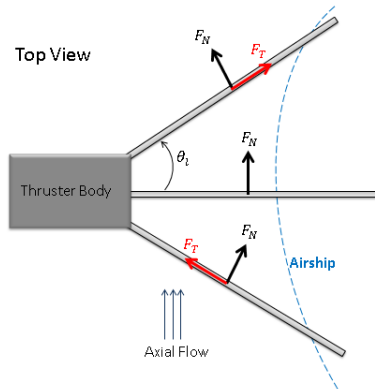


Figure 2-7: Illustration of the viscous drag forces on the thruster legs.

Table 2-2: Normal and tangential force coefficients from [17]

Normal Force F_N coefficient C_N	$C_N = 1.2s_{\theta_l}^2 \left(\frac{L_l D_l}{A_f} \right)$
Tangential Force F_T coefficient C_T	$C_T = 0.083c_{\theta_l}(1 - 0.422c_{\theta_l}) \left(\frac{\pi L_l D_l}{A_f} \right)$

The total viscous force coefficient due to the each thruster (three legs) $C'_{A_{leg}}$ in the direction of the axial flow can thus be given by:

$$C'_{A_{leg}} = (C_N \cos \theta_l + C_T \sin \theta_l) + (C_N) + (C_N \cos \theta_l + C_T \sin \theta_l) \quad (2.20)$$

Since each thruster has exactly the same dimensions, the total drag due to all 4 thrusters (12 thruster legs) can be given by:

$$C_{A_{leg}} = 4 \left(C'_{A_{leg}} \right) \quad (2.21)$$

Using measured values measured of $D_l = 0.005 \text{ m}$, $L_l = 0.13 \text{ m}$ and $\theta_l = 40^\circ$, we find $C_N \approx 0.0001854$, $C_T \approx 0.00005$, $C'_{A_{leg}} \approx 0.000535$ and $C_{A_{leg}} \approx 0.00214$.

2.2.2.3 Total Modified Drag in the Axial Direction

From [8], the axial drag coefficient of the hull $C_{A_{hull}} = 0.041$. Thus, the total axial drag at zero angle of attack C_{A_0} can now be given as a sum of the contributions from the airship hull, the gondola, the GPS antenna and the 12 thruster legs. Therefore, using Equation (2.18), the modified axial drag coefficient is calculated as $C_{A_0} \approx 0.058$ based on the frontal area of the airship. Abbott [16] had previously measured the protuberance drag of the gondola (which he calls the ‘car’) for another airship. The size of the gondola relative to the airship hull used in [16] is smaller than for the Mk-II ALTAV. In [16], the gondola increased the overall drag by about 20%. For the Mk-II ALTAV, the protuberances account for about a 32% overall increase in the axial drag, of which the gondola contributes at least 87%. Thus our results are consistent with those in [16].

2.3 Improvements to the Thruster Model

This section discusses two improvements that were made to the thruster model originally implemented by Peddiraju [8]. In particular, we consider two effects – the gyroscopic moments and the reaction torques exerted by the thrusters on the airship. Before moving

on to the derivation of these effects, we will estimate the inertia of the rotating parts on the thruster and present a method to calculate the speed of the thrusters, both essential to the derivations discussed in the following sections.

2.3.1 Moment of Inertia of the Thrusters

The term thruster used in this section means the motor-propeller arrangement. The motor consists of a stator (comprised of the copper windings) and a hollow rotor with magnets around its circumference. The propeller is then fixed on top of the motor shaft and fastened to it using 3 washers and a nut. Taking the above components into account, an approximate CAD model of the rotating parts of the thrusters was produced. It was divided into three components: the rotor, the propeller and the nut-washer combination. Figure 2-8 shows the CAD assembly and Table 2-3 gives the inertial information about the component parts, and the assembly as a whole.

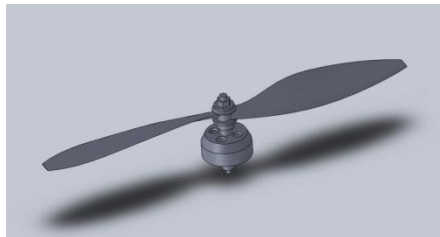


Figure 2-8: CAD model of the thruster

Table 2-3: Inertial properties of the rotating thruster components

Part	Mass (g)	Volume (cm ³)	Average Density (g/cm ³)	Inertia about rotation axis x_t (kgm ²)
Rotor	45	8.95	5.03	0.20×10^{-4}
Propeller	18	11.97	1.50	1.01×10^{-4}
Washers + Nut	11	2.93	3.75	0.04×10^{-4}
Overall Assembly	74	23.85	3.21	1.25×10^{-4}

The thruster frame was defined earlier in Section 2.1.1. It should be noted that the way the thruster-frame has been defined, the inertia of the thrusters along the y_t and z_t axes changes continuously due to the propeller rotations, since the overall mass distribution during the propeller rotation varies. A propeller is often modelled as an equivalent thin disk to overcome this complexity, and this approach is adopted here. As a result, the thruster has 2 planes of symmetry at all times, leading to a diagonal inertia matrix about the thruster frame $O_t x_t y_t z_t$:

$$\mathbf{I} = \begin{bmatrix} I_t & 0 & 0 \\ 0 & I'_t & 0 \\ 0 & 0 & I'_t \end{bmatrix} \quad (2.22)$$

where, I_t is the moment of inertia in the x_t direction and I'_t is the moment of inertia in the y_t and z_t directions, being equal by virtue of the condition of symmetry imposed by the propeller assumed as an equivalent disk.

The CAD model description yielded $I_t = 1.25 \times 10^{-4} \text{ kgm}^2$ and $I'_t = 0.65 \times 10^{-4} \text{ kgm}^2$. All four thrusters are presumed to be identical.

2.3.2 Determining Angular Velocity of the Propellers

We define the angular velocity vector of the thrusters in the thruster frame as $\boldsymbol{\omega}_T = [\omega_{prop} \ 0 \ 0]^T$. Since no sensors are present on the thrusters to measure their rotational speeds, we use the thrust-rpm relationship previously determined by Peddiraju [8], to deduce the rpm from the commanded thrust.

The experimental results from [8] are shown in Figure 2-9, where the thrust T has been plotted against ω_{prop}^2 . A linear fit for the experimental data points is found such that:

$$T = k_T \omega_{prop}^2 \quad (2.23)$$

where $k_T = 1.993 \times 10^{-5} \frac{N}{(rad/s)^2}$. This quadratic relationship is in agreement with data for propellers from other sources[36].

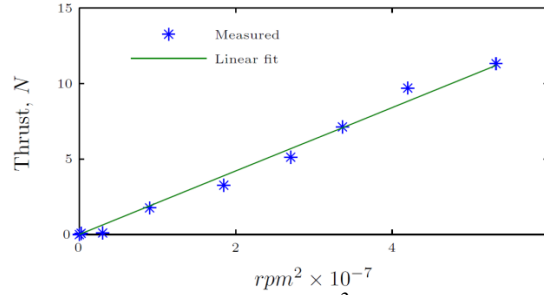


Figure 2-9: Thrust versus rpm^2 as measured in [8]

If the thrust generated by the thrusters is known, we can estimate ω_{prop} using the inverse relationship between ω_{prop} and T from Equation (2.23) as:

$$\omega_{prop} = k_{\omega_{prop}} \sqrt{T} \quad (2.24)$$

where $k_{\omega_{prop}} \approx 224 \frac{rad/s}{\sqrt{N}}$.

2.3.3 Gyroscopic Moments due to the Thrusters

Gyroscopic moments act on a body due to a combination of any two rotations that are orthogonal to each other, thus producing a moment which is orthogonal to both rotations. The moment exerted by the thrusters on the airship can be expressed as a cross-product between the applied rotation *experienced* by the thruster ω_{tot} and the *angular momentum* of the spinning thruster \mathbf{L} [37]. Thus:

$$\mathbf{M}_{gyro} = -\omega_{tot} \times \mathbf{L} \quad (2.25)$$

On the airship, the applied rotation is from two sources; the servo rotations and the rotations of the airship hull to which the thruster is attached.

To begin, a few simplifying assumptions are made. Firstly, since there is only a slight offset, less than 1 cm, between the axis of the servo-rotation and the centroid of the thruster, we assume that they intersect at the origin of the thruster-frame at point O_t as shown in Figure 2-10 (subscript i refers to the i 'th thruster).

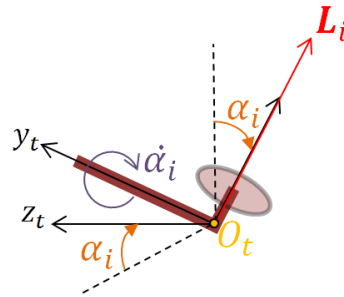


Figure 2-10: Servo rotation in the thruster frame

Also, the thruster arrangement is assumed to be attached rigidly to the airship hull, and so there is no relative motion between them due to the flexibility of the airship hull.

The angular momentum of the i 'th thruster L_i depends on its angular velocity ω_{T_i} at that instant. Thus, as depicted in Figure 2-10, L_i can be given by:

$$L_i = I\omega_{T_i} \quad (2.26)$$

where $\omega_{T_i} = [\omega_{prop,i} \ 0 \ 0]^T$. The body frame velocities of the airship $\omega = [p \ q \ r]^T$ expressed in the i 'th thruster frame can be given by $(\omega)_{t,i} = (\mathbf{R}_{t \rightarrow b})^T \omega$.

If the servo rotation is given as $(\omega_{servo})_{t,i} = [0 \ \dot{\alpha}_i \ 0]^T$, the total angular rate experienced by the thruster, $(\omega_{tot})_{t,i}$ can be given as:

$$(\boldsymbol{\omega}_{tot})_{t,i} = (\boldsymbol{\omega})_{t,i} + (\boldsymbol{\omega}_{servo})_{t,i} \quad (2.27)$$

Using Equation (2.26) and (2.27), the gyroscopic moment exerted by thruster i , can be written as:

$$(\mathbf{M}_{gyro})_{t,i} = -(\boldsymbol{\omega}_{tot})_{t,i} \times \mathbf{I}\boldsymbol{\omega}_{T_i} \quad (2.28)$$

Expressing the above moment vector in the body-frame, we get:

$$(\mathbf{M}_{gyro})_{b,i} = -(\mathbf{R}_{t \rightarrow b})_i (\mathbf{M}_{gyro})_{t,i} \quad (2.29)$$

Expanding Equation (2.29) to give us the moments in the x, y and z directions, yields:

$$(\mathbf{M}_{gyro})_{b,i} = \begin{bmatrix} I_t \omega_{prop,i} (q \cos \alpha_i) - I_t \omega_{prop,i} \dot{\alpha}_i \cos(\alpha_i) \\ -I_t \omega_{prop,i} (p \cos \alpha_i + r \sin \alpha_i) \\ I_t \omega_{prop,i} (q \sin \alpha_i) - I_t \omega_{prop,i} \dot{\alpha}_i \sin(\alpha_i) \end{bmatrix} \quad (2.30)$$

The first term in each element is the contribution to the gyroscopic moment from the vehicle rotations. The second term in the first and third elements are due to the servo rotations. As can be seen, there is no gyroscopic moment due to servo rotations in the y -axis. Also, the gyroscopic moments only depend on the inertia of the thrusters about the x_t axis. This saves us the need to model the motor-prop arrangement as an equivalent disk.

The total thruster gyroscopic moment exerted on the airship \mathbf{n}_M expressed in the body frame due to contributions from the body rotations and the servo rotations of all four thrusters can be given as:

$$\mathbf{n}_M = \sum_{i=1}^4 (\mathbf{M}_{gyro})_{b,i} \quad (2.31)$$

2.3.4 Reaction Torques due to the Thrusters

In this section, we discuss the reaction torques acting on the airship due to the thrusters. This reaction torque model is then added to the thruster model to produce a more comprehensive thruster model. The reaction torques are present due to two reasons, 1) a component of the aerodynamic drag of the propellers resulting in a torque about the axis of the propeller and 2) the inertial torques due to the thrusters' angular accelerations. For the Mk-II ALTAV, modeling these torques is important, since all four thrusters spin in the same direction (CCW viewed from above). The goal of the reaction torque characterization in this section is to be able to fully describe the reaction torques acting on the airship, assuming that a thrust model for the thrusters is available. In our case, a reliable thrust model is already in place as discussed in Section 2.3.2. For a brief overview of the measurement setup of the thrusts and torques, and the thrust model developed by Peddiraju [8] the reader is referred to Appendix A. The reaction torque model will be based on data collected by Peddiraju, but not presented in [8].

Typical Reaction Torque Curve

A command input c , which is just a PWM value normalized between 0 and 1, regulates the motor speeds. In each test, Peddiraju [8] first commands $c = 0.19$ at $t = 4$ s to idle the thrusters. Then, at $t = 14$ s, a unique value of the command input c is commanded for each of the 6 tests (0.25, 0.30, 0.35, 0.40, 0.45, 0.50). At $t = 54$ s the thrusters are idled again.

To remove noise from the reaction torque data measured by Peddiraju, the results are post-processed using the *filtfilt()* command in MATLAB. This function performs a bi-

directional zero-phase filtering operation, which does not introduce time delays into the data. The filter used is a second order low-pass Butterworth filter with a cut-off frequency of 1250 Hz. To choose this frequency, we first generate a frequency spectrum from which the measurement noise can be identified. A typical reaction torque curve, before and after filtering, for $c = 0.35$ is shown in Figure 2-11 for the entire range of measurement time, while Figure 2-12 shows specifically the rise and fall behaviours.

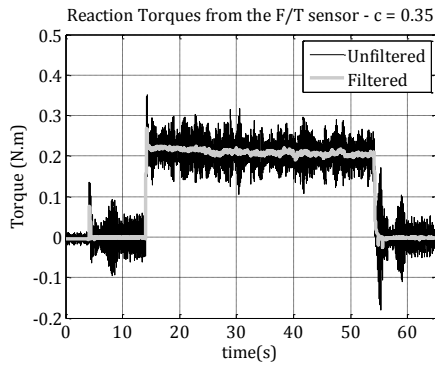


Figure 2-11: Typical reaction torque curve, $c = 0.35$

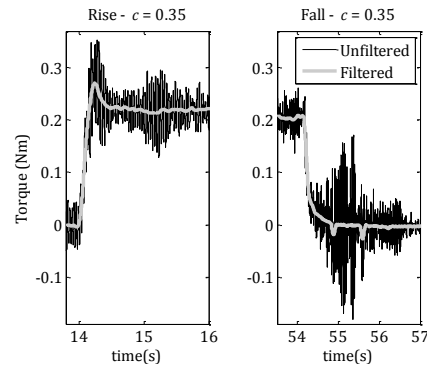


Figure 2-12: Typical reaction torque curve, $c = 0.35$. Details of rise and fall.

The filtered thruster torque, seen in Figure 2-11, can be separated into two components [22, 25]. Firstly, there is the aerodynamic torque acting on the thruster, primarily an effect of the aerodynamic drag acting on the propeller surface during operation. Secondly, there is an inertial component acting on the airship acting opposite the motion of the accelerating thruster, by virtue of Newton's third Law. Thus, during a change in thruster velocity, both the inertial and aerodynamic effects will be present, while during steady state operation, only the aerodynamic effect will be present. Therefore, we define the overall reaction torque Q as the sum of two torques:

$$Q = Q_{aero} + Q_{iner} \quad (2.32)$$

where Q_{aero} is the aerodynamic component of the torque and Q_{iner} is the inertial component of the torque.

Relationship between steady-state Aerodynamic Torque Q_{aero} and Thrust T

It is well documented in literature with regards to constant pitch marine propellers that, in steady-state, a linear relationship exists between the thrust T and the aerodynamic torque Q_{aero} [38]. We can verify this for our propeller by plotting the steady-state values of the thrust against the torque for a series of command-inputs as seen in Figure 2-13.

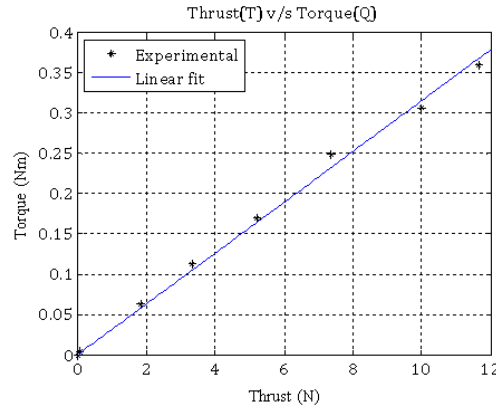


Figure 2-13 : Torque vs. Thrust. Experiment and linear fit

A linear fit is obtained for these data-points, which allows us to relate Q_{aero} against T linearly as:

$$Q_{aero} = k_Q T \quad (2.33)$$

where $k_Q = 31.52 \times 10^{-3} \frac{Nm}{N}$.

Relationship between Inertial Reaction Torque Q_{iner} and Thrust T

The inertial torque can be written as:

$$Q_{iner} = I_t \dot{\omega}_{prop} \quad (2.34)$$

where I_t is the moment of inertia of the rotating parts of the thruster about the axis of rotation and $\dot{\omega}_{prop}$ is the rotor acceleration. Since we do not have sensors onboard to measure $\dot{\omega}_{prop}$, we will need to estimate it. This can be done using the relationship between the steady-state thrust and the corresponding ω_{prop} . A quadratic relationship

between the steady-state thrust and the velocity of the thruster had been previously determined experimentally by means of the F/T sensor and a tachometer by Peddiraju[8], as discussed previously in Equation (2.24). Equation (2.24) can now be used in Equation (2.34) to estimate the inertial torque acting on the airship due to the thruster. Thus,

$$Q_{iner} = I_t \frac{d(k_{\omega_{prop}} \sqrt{T})}{dt} \quad (2.35)$$

Resulting Equation for the Estimated Torque

We can now estimate the total reaction torque by rewriting Equation (2.32) in light of the results obtained in the previous two sub-sections. The estimated torque can be written as:

$$Q = k_Q T + I_t \frac{d(k_{\omega_{prop}} \sqrt{T})}{dt} \quad (2.36)$$

The key benefit of an equation of this form is that Q can be estimated based only on T , without explicitly having direct information on ω_{prop} . From the experimentally measured values of the thrusts, it would be useful to see if Equation (2.36) gives a good estimate of the torque. To this end, we apply this equation to the measured thrust T for each command input to get an estimated torque, and compare the results with the measured torque. The results for a command input of $c = 0.35$ are given in Figure 2-14 and Figure 2-15. Figure 2-14 shows the comparison over the entire range of the measurement time, while Figure 2-15 shows specifically the rise and fall behaviours of the torque. For a complete set of results, please refer to Appendix D.

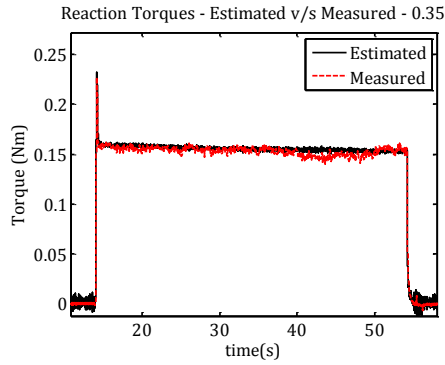


Figure 2-14: Estimated and measured reaction torques

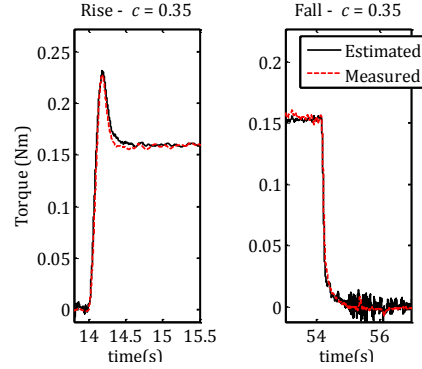


Figure 2-15: Estimated and measured reaction torque, details of rise and fall.

Very good agreement is obtained between the estimated and the measured torques for the entire range of command inputs, and we conclude that this method is able to successfully estimate both the rising and the falling behaviours of the reaction torques.

Revised Thruster Model to include Reaction Torques

The torque model, based on Equation (2.36) is now added to the existing dynamics model of the thruster leading to the block diagram shown in Figure 2-16. A linear interpolation previously determined by Peddiraju[8] calculates the command input, c , as a function of the desired thrust (T_{des}) commanded by the controller. The thrust model in [8] then simulates the thrust based on a first-order transfer function for a given command-input. The thrust simulated is then used to determine the reaction torque $Q_i = [-Q_i \ 0 \ 0]^T$ acting on the airship due to each thruster using Equation (2.36).

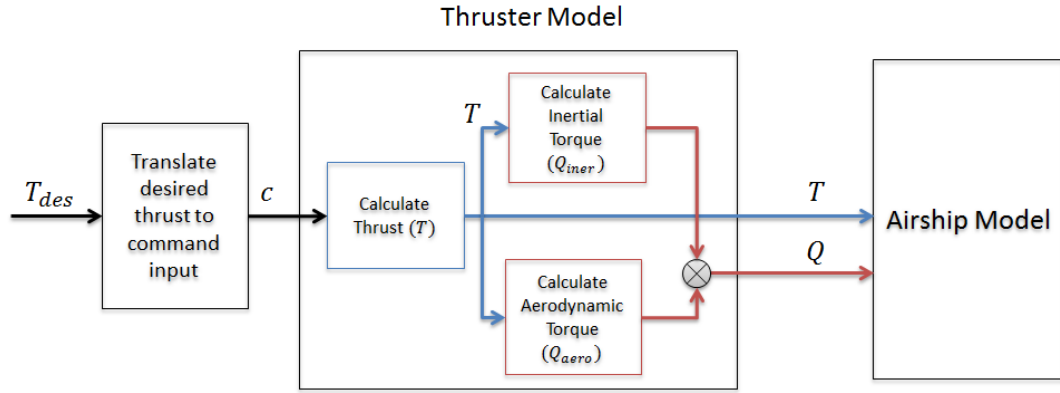


Figure 2-16: Block diagram of the torque dynamics model

Finally, the sum of the reaction torques due to all four thrusters expressed in the body-frame can be given as:

$$\mathbf{n}_Q = \sum_{i=1}^4 (\mathbf{R}_{t \rightarrow b})_i \mathbf{Q}_i \quad (2.37)$$

2.4 Implementing the Improvements to the Simulation Model

Having modeled the intended improvements for the dynamics model and the thruster model, we now add them to the simulation model in [8] and perform closed-loop simulation tests to assess how they affect the performance and stability of the airship during flight. To this end, we perform two closed-loop simulations with the same set of desired states: (a) one without the improvements added to the simulation model, and (b) one with the improvements added to the simulation model.

For this simulation, we are using the PID controller developed in [8] as the low-level controller. However, the gains have been adjusted for better performance. The new controller gains are provided in Table 3-1 and are used throughout the current thesis.

The desired states for this maneuver are shown in Figure 2-17. Over the time period A, indicated on the figure, step changes in desired pitch and yaw are commanded at zero forward speed, which induce large motions in the airship. The thrusters respond aggressively to track the desired motions. This region will thus give good insight into the effect of gyroscopic moments (Section 2.3.3) since it will contain, both, body- and thruster-rotations. In region B, a forward velocity of 1 *m/s* is commanded to see how the response is affected by the increased drag due to protuberances (Section 2.2.2). In region C, a large change in desired yaw is commanded to evaluate how the introduction of the rotational damping moments affects the simulation, by examining the corresponding yaw profile, and the total thruster moment in the *z*-direction (Section 2.2.1). Finally, in region D, the airship hovers at a desired height, and during this time, we examine the moments generated by the thruster in the *z*-direction to see how the thruster reaction torques affect the airship (Section 2.3.4). Figure 2-17 shows the profiles of the five states during the simulations while Figure 2-18 shows the corresponding thruster forces and moments exerted on the airship. Results for the test cases (a) and (b) are marked ‘With Improvements’ and ‘Without Improvements’, respectively.

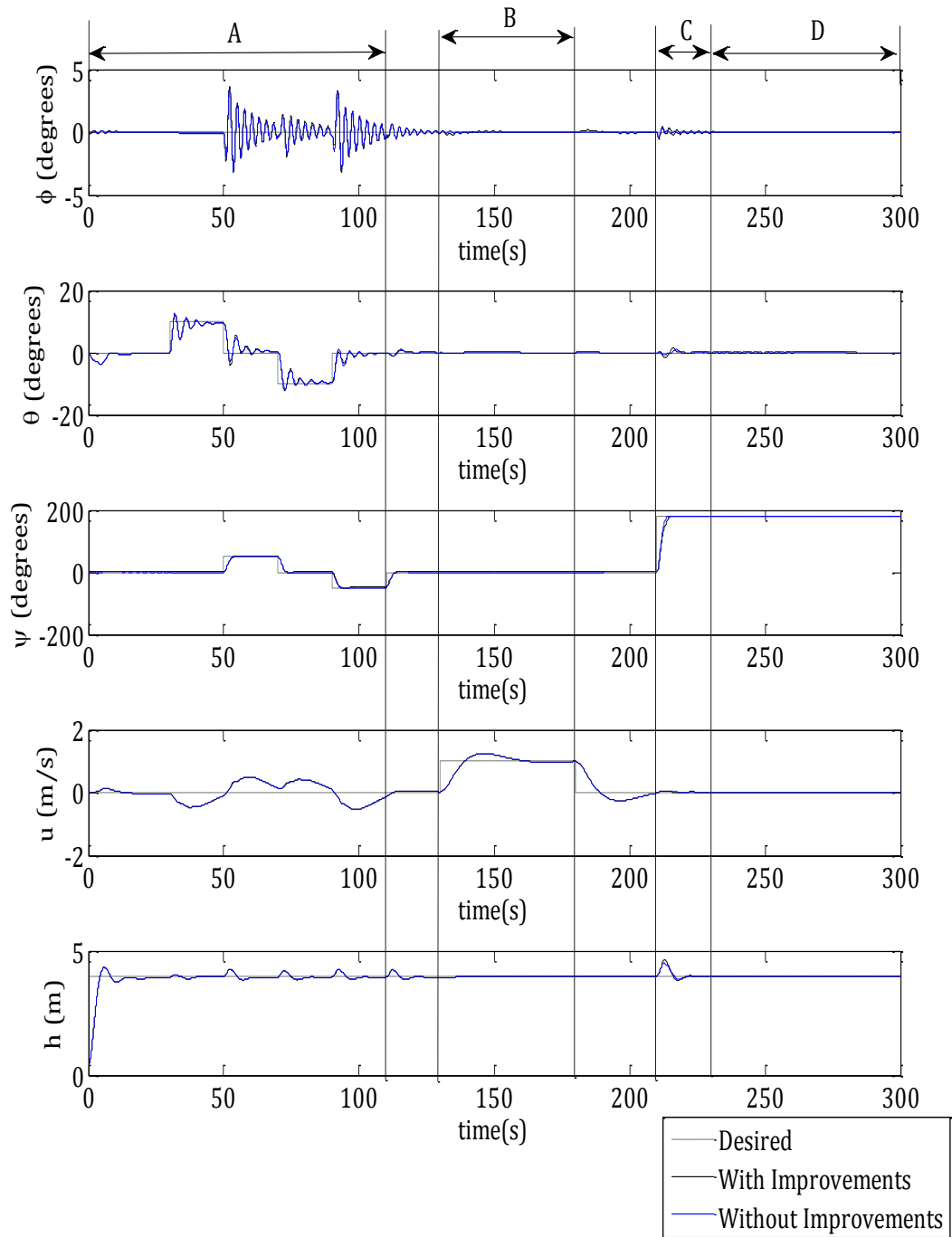


Figure 2-17: Top to bottom: roll, pitch, yaw, forward velocity and height. Results for test cases (a) and (b)

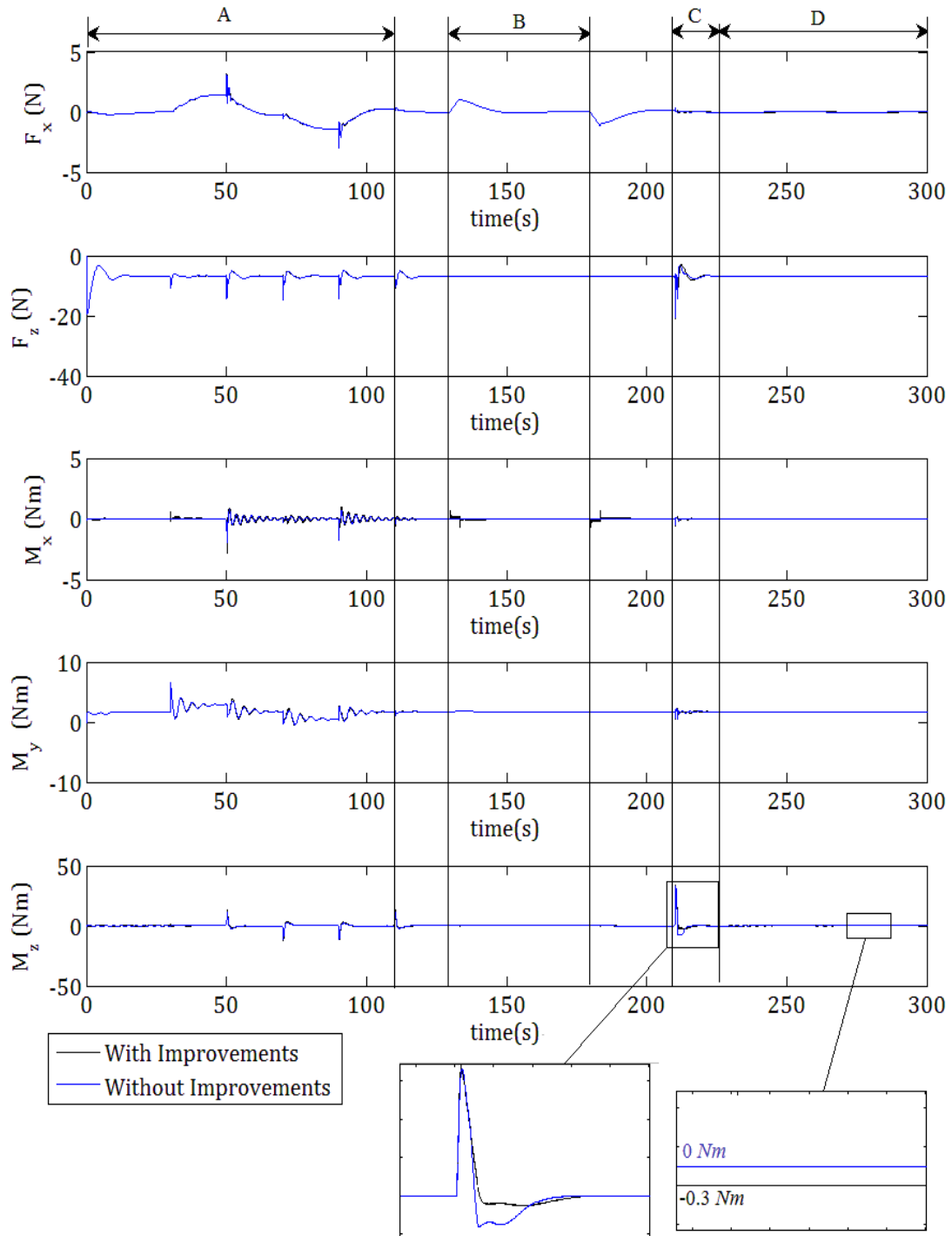


Figure 2-18: Thruster forces and moments, top to bottom: F_x , F_z , M_x , M_y , and M_z for tests cases (a) and (b)

As can be seen from region A in Figure 2-17, in closed-loop flight, the inclusion of the gyroscopic moments does not result in any visible change on the airship. Figure 2-18 also shows that the difference in the thruster forces and moments commanded between the two simulations is nearly identical, indicating that the airship experiences only negligible gyroscopic moments even during extreme maneuvers. This is because, even though the thrusters are spinning at high speeds, the inertia of the rotating parts and the angular rates incurred during stable flight, are quite small. In region B, a 30% increase in the axial drag coefficient introduces minimal change in the additional forward drag force required to cause a 1 m/s change in the forward velocity. In fact, the amount of additional force required in the x -direction (F_x in Figure 2-18) was, at most 0.01 N . In region C, the airship's yaw response in both simulations is similar. However the detailed plot in Figure 2-18 for region C, indicates that the thruster control effort M_z , with the damping moments included, is reduced during the period where M_z brings the yaw-rate back to zero. This is because the damping moment aids the thruster to decelerate the airship, thereby reducing the thruster effort needed to prevent the yaw from overshooting the desired setpoint. Finally, the effect of the thruster reaction torques is also minimal, as shown in Figure 2-18 region D. The detailed view shown for this region shows that with the reaction torques included, the controller generates about -0.3 Nm moment in the z -direction to counter the equal and opposite reaction torques. Although, this is an insignificant magnitude in closed-loop flight, its effect will be more important during open-loop flight validation tests in Chapter 4. It is emphasized that the evaluation of these effects while using a closed loop controller is not ideal, since the controller actively corrects for any differences in the dynamics. Therefore, it is expected that the airship motions would be

quite similar, and that differences in the models are exhibited as differences in the thruster forces and moments.

2.5 The Airship Hull – Refining its Geometric Description

Peddiraju [8] had measured the hull profile early during the course of his work. However due to wear and tear of the hull over time, this hull was replaced with a newer one. In [8], although all the experiments conducted (including determination of physical parameters) were with the newer hull, the mathematical description of the newer hull profile was determined not through an experimental measurement, but a scaling of the older profile. Since it is preferable to have an accurate description of the newer hull profile in Section 2.2.1, we repeat the measurement using the same method as Peddiraju [8].

2.5.1 Measurement

The hull is symmetric about the longitudinal x -axis. The profile of the inflated airship hull was measured by suspending 28 plumb-bobs on one side along the equator of the hull shown in Figure 2-19. The plumb-bobs were just touching the ground when suspended. The resulting roll was compensated for by suspending a comparable mass from the other side. A paper was then laid out under the plumb-bobs and the location of each, relative to the nose of the airship, was marked on the sheet of paper.



Figure 2-19: Measuring hull profile by suspending plumb-bobs

An eight-order polynomial $R(x')$ was then fitted to these points using the *cftool()* in MATLAB, yielding:

$$R(x') = -0.00283x'^8 + 0.0526x'^7 - 0.402x'^6 + 1.635x'^5 - 3.815x'^4 + 5.148x'^3 - 4.02x'^2 + 2.033x' \quad (2.38)$$

Where x' is the distance from the nose along the longitudinal axis. Figure 2-20 below shows the experimental data points and the eight order polynomial fit.

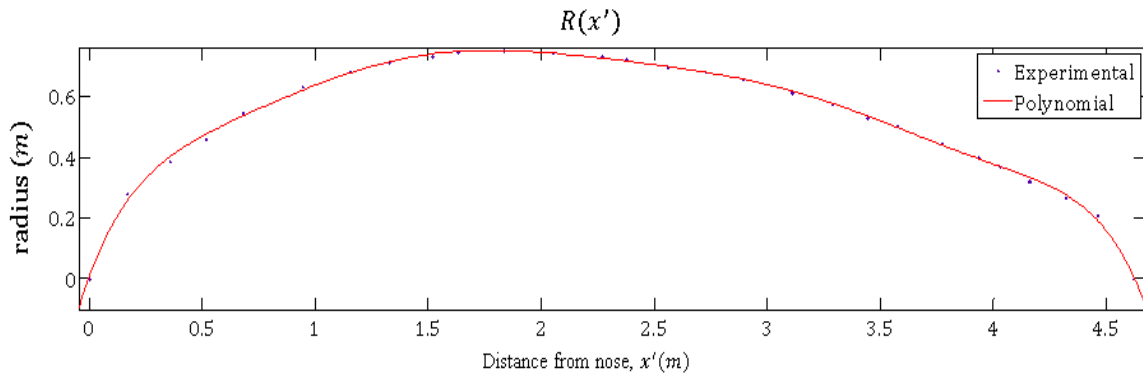


Figure 2-20: New hull profile polynomial approximation

2.5.2 Refined CAD Model

With the mathematical description of the new profile, the airship's CAD Model, as developed by Peddiraju[8] using ProEngineer was now revised, only by changing the description of the hull profile and keeping all other properties unchanged. The values

from the revised CAD model are presented in Table 2-4. Finally, a mathematical description of the profile relative to the center of buoyancy x_m can be obtained by replacing x' by x in Equation (2.38) such that $x = -(x' - x_m)$, with $x_m = 2.210$ m. The hull profile in terms of x , $R(x)$ is given as:

$$R(x) = -0.00283x^8 + 0.00245x^7 + 0.0236x^6 - 0.0161x^5 - 0.0647x^4 + 0.0465x^3 - 0.0433x^2 - 0.0804x + 0.750 \quad (2.39)$$

Table 2-4: Airship inertial properties and constants used in the dynamics model

Airship Parameter (units)	Value
Total mass of airship, m (kg)	6.416
Density of air, ρ_{air} (kg/m ³)	1.204
Density of Helium, ρ_{He} (kg/m ³)	0.166
Volume of hull, V (m ³)	4.747
Length of hull, L (m)	4.626
Center of buoyancy location from nose, x_m (m)	2.210
Center of gravity location from nose, x_{CG} (m)	2.183
Maximum diameter of hull, d_{max} (m)	1.500
Frontal Area of Airship, A_f (m ²)	1.770
Planform Area of the Airship, A_p (m ²)	5.204
Fineness ratio, L/d_{max} (non-dimensional)	3.084
Mass of displaced air, m_D (kg)	5.716
Inertia of displaced air, I_D (kgm ²)	6.761
Longitudinal added mass, m_{11} (kg)	0.646
Lateral added mass, m_{22} (kg)	4.672
Added inertia, m_{33} (kgm ²)	3.368

Chapter 3 The Airship Controller Suite - Low and High Level Controllers

This chapter discusses the design of the controller suite implemented on the airship. The controller suite is comprised of the following two sub-controllers, implemented hierarchically:

- 1) The low-level controller (LLC) tracks the desired attitude, velocity and altitude profiles generated by the HLC. The objective of the LLC is to stabilize the airship around those HLC commands.
- 2) The high-level controller (HLC) generates the desired attitude, velocity and altitude profiles of the airship to be used by the low level controller. The objective of the high level controller is to guide the vehicle along a given path.

3.1 Controller Architecture

As mentioned in Chapter 1, the Mk-II ALTAV is an inherently unstable airship due to its finless design. Moreover, the thruster-servo arrangement on this airship allows control over five degrees of freedom, namely, roll, pitch, yaw, surge and heave with no control over the lateral degree of freedom (sway). The controller suite design is based on a strategy to control five motion variables: the attitude (ϕ, θ, ψ), forward speed (u) and the inertial height (h) in order to achieve desired motion.

The major advantage of a hierarchical controller suite scheme as presented in this chapter is that it results in a more modular system, that allows designing and testing various LLC and HLC algorithms independently. Figure 3-1 shows the schematic for the proposed

controller architecture. Waypoints defining the desired trajectory in space for the airship are fed into the HLC along with the current airship motion data which includes its position, orientation and speed. The guidance algorithm then generates five desired states ($\phi_d, \theta_d, \psi_d, u_d$ and h_d) that are fed into the LLC. Based on the error between the current and desired states, the LLC generates desired values of thruster and servo commands to reduce this error. The thrusters and servos on the airship then respond to these LLC outputs. The resulting motion of the airship is then fed back into the HLC and LLC.

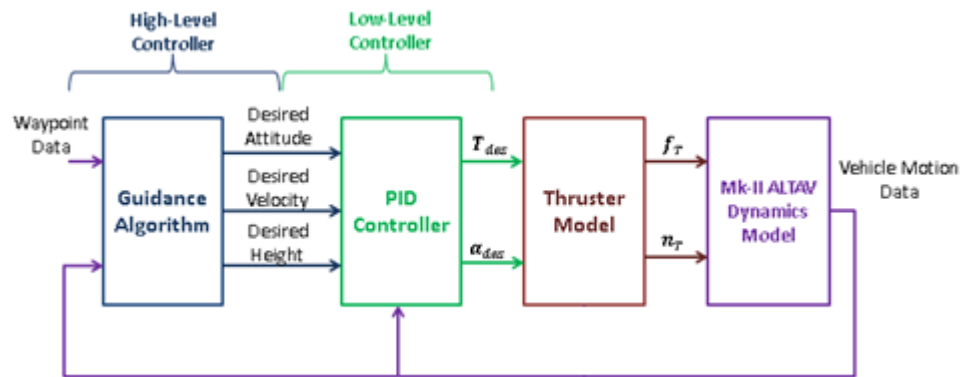


Figure 3-1: Schematic of the overall airship controller

3.2 Low-Level controller

The low level controller was developed by Peddiraju [8]. It consists of five independent PID (Proportional-Integral-Derivative) controllers each controlling one of the five states of the airship i.e. roll(ϕ), pitch(θ), yaw(ψ), forward-speed (u) and inertial height(h). The yaw and forward-speed controllers generate force commands along the x -direction of the body frame, while the roll, pitch and height controllers generate force commands in the z - direction of the body frame. The yaw and inertial height PID controllers are presented below as examples.

To control the yaw, a differential thrust is commanded in the x -direction on the left and right pairs of thrusters as follows:

$$\begin{bmatrix} T_{1x,\psi} \\ T_{2x,\psi} \\ T_{3x,\psi} \\ T_{4x,\psi} \end{bmatrix} = \begin{bmatrix} -k_{P,\psi} \\ -k_{P,\psi} \\ k_{P,\psi} \\ k_{P,\psi} \end{bmatrix} (\psi_d - \psi) + \begin{bmatrix} -k_{I,\psi} \\ -k_{I,\psi} \\ k_{I,\psi} \\ k_{I,\psi} \end{bmatrix} \int (\psi_d - \psi) dt + \begin{bmatrix} -k_{D,\psi} \\ -k_{D,\psi} \\ k_{D,\psi} \\ k_{D,\psi} \end{bmatrix} (\dot{\psi}_d - \dot{\psi}) \quad (3.1)$$

where, $T_{ix,s}$ represents the thrust generated by the i 'th thruster in the x direction by the controller for state s . $k_{P/I/D,s}$ refers to the proportional (P)/ integral(I)/ derivative(D) gain of the state s .

The height is controlled by commanding a thrust in the z -direction as follows:

$$\begin{bmatrix} T_{1z,h} \\ T_{2z,h} \\ T_{3z,h} \\ T_{4z,h} \end{bmatrix} = \begin{bmatrix} k_{P,h} \\ k_{P,h} \\ k_{P,h} \\ k_{P,h} \end{bmatrix} (h_d - h) + \begin{bmatrix} k_{I,h} \\ k_{I,h} \\ k_{I,h} \\ k_{I,h} \end{bmatrix} \int (h_d - h) dt + \begin{bmatrix} k_{D,h} \\ k_{D,h} \\ k_{D,h} \\ k_{D,h} \end{bmatrix} (\dot{h}_d - \dot{h}) \quad (3.2)$$

where $T_{iz,s}$ represents the thrust generated by the i 'th thruster in the z -direction. Similarly, a differential thrust in the z -direction between the front and rear pairs of thrusters controls the pitch, a differential thrust in the z -direction between the right and left pair of thrusters controls the roll, and a net thrust in the x -direction from all four thrusters controls the forward speed. Details of the relevant PID controller equations can be found in [8].

The net commanded thrust for the i 'th thruster T_i is computed as:

$$T_i = \sqrt{(T_{ix,u} + T_{ix,\psi})^2 + (T_{iz,h} + T_{iz,\phi} + T_{iz,\theta})^2} \quad (3.3)$$

The commanded servo angle for the i 'th thruster α_i is computed as:

$$\alpha_i = \tan^{-1} \frac{(T_{ix,u} + T_{ix,\psi})}{-(T_{iz,h} + T_{iz,\phi} + T_{iz,\theta})} \quad (3.4)$$

where a limit of $\alpha_i \in [-90,90]$ is imposed in the model following the same physical limit of the servo on the actual thruster. A servo angle of 0° would vector the thrust vertically upwards (negative z -direction). The airship relies on its net-heaviness (negative buoyancy) to reduce its height. Furthermore, a rate-limit of $\pm 287^\circ/s$ is imposed on the servo rotations since it was experimentally shown in [8] that this serves as a good model for the servo dynamics, under nominal-load conditions.

The gains were re-tuned from [8] by trial and error to give better tracking performance under wind disturbances. A summary of the gains is presented in Table 3-1.

Table 3-1: Summary of PID controller gains for the airship

	PID Gains as in [8]			Re-tuned PID Gains		
	P	I	D	P	I	D
Roll	0.05 N/deg	0.01 N/deg s	0.07 N/(deg/s)	0.02 N/deg	0 N/deg s	0.05 N/(deg/s)
Pitch	0.28 N/deg	0 N/deg s	0.22 N/(deg/s)	0.05 N/deg	0.03 N/deg s	0.1 N/(deg/s)
Yaw	0.25 N/deg	0 N/deg s	0.1 N/(deg/s)	0.25 N/deg	0 N/deg s	0.1 N/(deg/s)
Height	0.37 N/m	0 N/ms	0.25 N/(m/s)	0.7 N/m	0.05 N/ms	1.5 N/(m/s)
Velocity	0.75 N/(m/s)	0 N/m	0 N/(m/s ²)	0.8 N/(m/s)	0.5 N/m	1.2 N/(m/s ²)

3.2.1 Simulation Results for the Low-Level Controller

A simulation using the tuned gains was carried out. In this simulation, we are testing the LLC's ability to track desired setpoints, and its ability to handle changes in desired setpoints. To this end, we will command setpoints in yaw, pitch, velocity and height that vary with time. Desired roll will be set at zero, since this is the way the airship is typically flown. All initial states are set to zero.

Figures 3-2 – 3-6 show the desired and actual states' profiles during a 200 s simulation. The LLC tracks the desired state profiles successfully and the steady-state convergence of

the controllers is good. The roll shows some oscillatory behaviour but remains stable. There are little to no steady-state errors in the pitch, yaw, velocity and height; an important result due to the introduction of integral gains. The airship also responds gracefully to setpoint changes. For example, a large step setpoint change in pitch is commanded around $t = 55 \text{ s}$, which the airship tracks easily, with minimal overshoot and a settling time of less than 10 s. One may notice that the forward-velocity is quite sensitive to setpoint changes in the other states. A closer look into Figure 3-5 reveals slight upsets at $t = 55 \text{ s}, 110 \text{ s}, 140 \text{ s}$ and 170 s . This behaviour results from corresponding changes commanded in desired pitch and yaw at those times, indicating some coupling between the states. The velocity controller recovers well from these upsets and remains stable. The most significant improvement from retuning of the gains is the elimination of oscillations in the inertial height and velocity profiles that were present in [8].

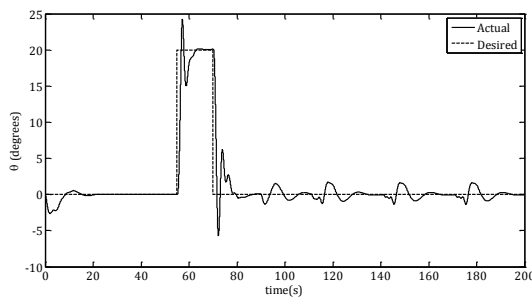


Figure 3-2: Pitch profile. PID simulation

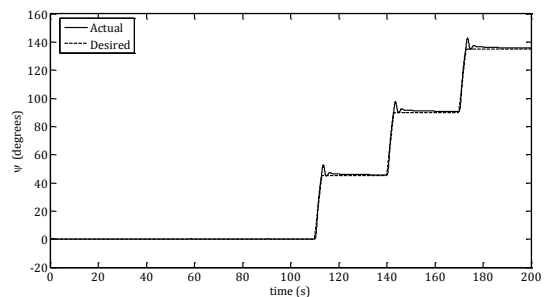


Figure 3-3: Yaw profile. PID simulation

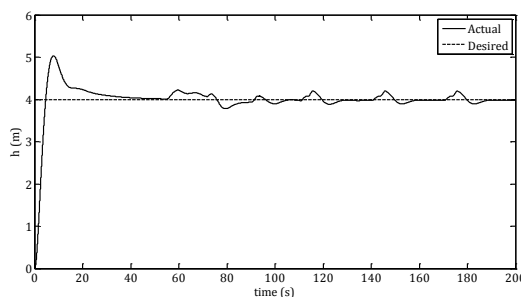


Figure 3-4: Inertial height profile. PID simulation

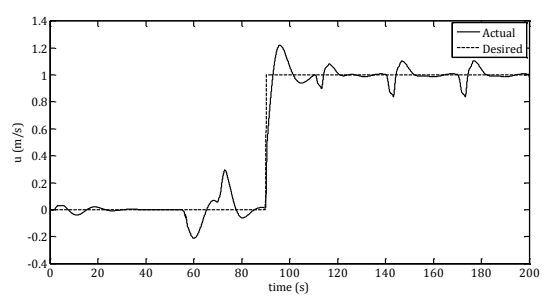


Figure 3-5: Velocity profile. PID simulation

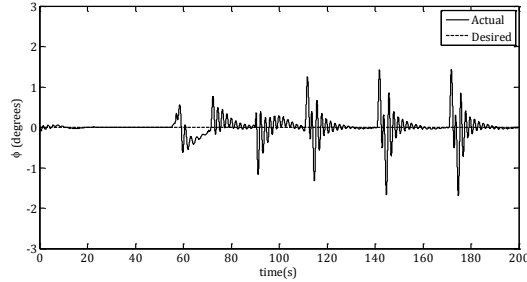


Figure 3-6: Roll profile. PID simulation.

3.3 High-Level Controller

In this section two HLCs (also called guidance algorithms) are discussed. First, a non-dynamics-based guidance algorithm that was implemented previously on the C-SCOUT underwater vehicle in [39] is discussed in Section 3.3.1. A non-dynamics-based guidance algorithm only takes into account the current states. It does not include any information about the rates of the states (derivatives), or their time histories (integrals). It also does not consider any information of the environmental disturbances (such as currents in water, and wind in air). The algorithm from [39] was chosen since it is a simple geometric algorithm that has been tested in a uniform, steady underwater environment with no disturbances. As such, it serves as a good starting point to test the overall HLC-LLC controller suite architecture. An advanced guidance algorithm is proposed later in 3.3.2 which tries to improve the system performance in windy conditions.

3.3.1 Non-Dynamics-Based Guidance Algorithm

The *NED* frame refers to the inertial North-East-Down frame. The basis of the algorithm is that the airship follows a ghost vehicle on the desired wayline whose position in the inertial frame is $\mathbf{r}_{tar} = [N_{tar} \ E_{tar} \ D_{tar}]^T$, as shown in Figure 3-7.

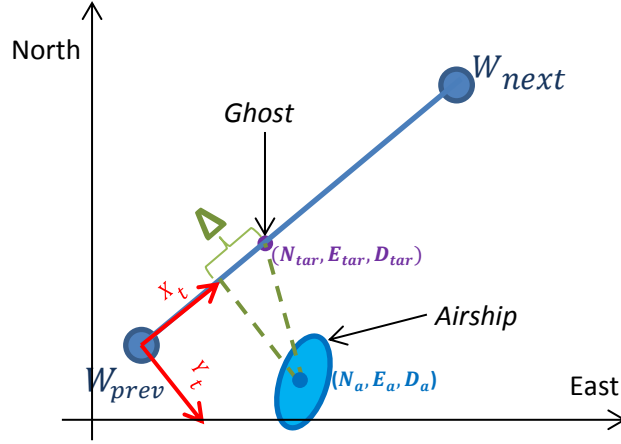


Figure 3-7: The ghost vehicle and the desired wayline in the X_t - Y_t frame

The position of the ghost vehicle is chosen at a distance, Δ , in front of the point on the wayline that is the shortest distance from the airship's center of mass. If $\mathbf{r}_a = [N_a \ E_a \ D_a]^T$ is the position of the airship's center of mass expressed in the inertial frame, the desired setpoints for yaw, pitch and height are calculated as follows:

$$\psi_d = \text{atan2}(E_{tar} - E_a, N_{tar} - N_a) \quad (3.5)$$

$$\theta_d = -\tan^{-1} \left(\frac{D_{tar} - D_a}{\sqrt{(E_{tar} - E_a)^2 + (N_{tar} - N_a)^2}} \right) \quad (3.6)$$

$$h_d = -D_{tar} \quad (3.7)$$

The desired forward velocity is held at $u_d = 1 \text{ m/s}$ while the desired roll is held at $\phi_d = 0^\circ$.

3.3.1.1 Simulation results: Non-Dynamics-Based Guidance Algorithm

The guidance algorithm is implemented in Simulink along with the LLC controller described in Section 3.1. The airship is commanded to follow the waylines described by the waypoints given in Table 3-2. Figure 3-8 shows graphically the chosen waypoints in a North-East-Up frame. This waypoint pattern will test the guidance algorithm's ability to

deal with height, pitch and yaw changes. In the presence of wind, a straight-line pattern allows us to evaluate the effect of tail-, head-, and cross-winds separately.

Table 3-2: Waypoints describing the waylines in the simulation

	N	E	D
Waypoint 1	0	0	-4
Waypoint 2	0	40	-6
Waypoint 3	40	40	-3
Waypoint 4	40	0	-5
Waypoint 5	0	0	-4

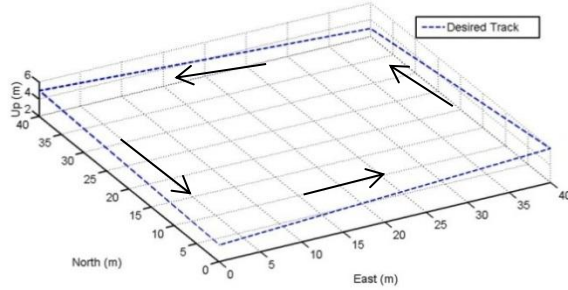


Figure 3-8: Desired path in *NEU* frame

The initial values of five states, both actual and desired, are set to zero. To stabilize the airship, for the first 10 seconds we command the airship to attain an inertial height of 4 meters after which the waypoint controller is engaged. An acceptable value of Δ is chosen to be 4 *m*. As for the turning criterion, the airship transitions to the next wayline once it is 4 meters away from the current targeted waypoint.

Rate-limiters are employed on the generated desired pitch and yaw to ensure that the airship is not destabilized during flight by changes of set-point. The values of these rate-limiters were chosen by trial and error to give satisfactory performance. The rate limits for the desired pitch and yaw angles were chosen as $\pm 5^\circ/s$ and $\pm 15^\circ/s$, respectively.

Simulations were carried out for two wind conditions: 1) No Wind; 2) Wind at 3 *kph* (0.83 *m/s*) from the North. The vertical component of the wind is set to zero. The first test case is intended to evaluate the guidance algorithm's general performance while the second is meant to evaluate its ability to handle wind.

Analysis Test Case 1

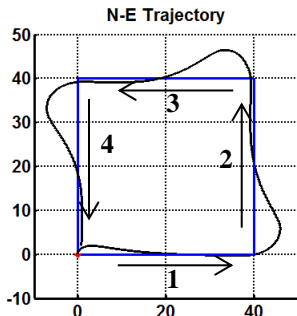


Figure 3-9: Airship trajectory in *NE* frame - test case 1

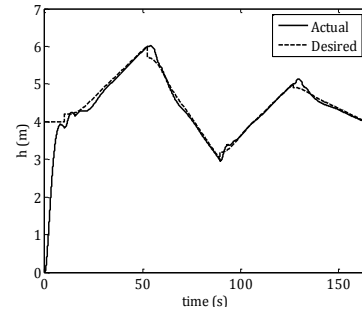


Figure 3-10: Height profile - test case 1

The trajectory evolution of the airship is shown in Figure 3-9 and Figure 3-10. The airship successfully tracks the given set of waypoints. However, at the turns, there is a sizeable overshoot of about 6 m from the desired wayline. One way to reduce this is by increasing the value of Δ but that tends to increase how far down the desired wayline the airship manages to zero its cross track error (which in this case is around the 20 m mark beyond each waypoint). Thus, a compromise was made between the two in the selection of Δ . In general, in no-wind conditions, the performance of this algorithm is acceptable, but not stellar.

Analysis Test Case 2

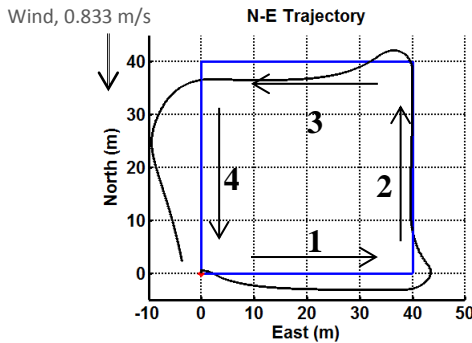


Figure 3-11: Airship trajectory in *NE* frame - test case 2.

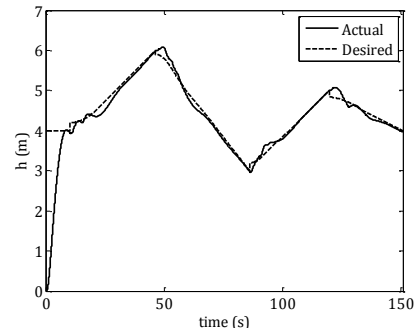


Figure 3-12: Height profile - test case 2

The major effect of the wind, as shown in Figure 3-11 and Figure 3-12, is that it pushes the airship off-course (See wayline 1 and 3 in Figure 3-12). This result is largely due to two factors:

- 1) The desired yaw setpoint is generated to align the airship's yaw angle with the local track tangent, while not explicitly trying to minimize the cross track error.
- 2) In the presence of cross-winds the airship presents a large drag surface area to the oncoming wind.

A successful guidance algorithm for this vehicle should take these effects into account. Turning into the tail wind leg appears particularly difficult for the airship (wayline 4) because the airship is trying to maintain the desired 1 m/s forward speed (ground speed). Given that the guidance algorithm does not compensate for wind-effects, the airship does not manage to zero the cross-track error while trying to intercept wayline 4.

In summary, this guidance algorithm employs a simple geometric method to calculate the desired setpoints for yaw, pitch and height. No information is available to the guidance algorithm on how these values are affected by the wind. The algorithm also makes no specific effort to minimize the cross-track error. For a low-altitude vehicle, a tight conformance to the desired track is vital. The above short-comings make this guidance algorithm undesirable for a light vehicle that is heavily affected by winds.

3.3.2 Dynamics Based Guidance Algorithm

Apart from being highly affected by ambient wind conditions, the airship operates at low speeds ($0 - 3\text{ m/s}$) making it difficult to have on-board sensors for wind estimation. In light of this, and based on our literature review in Section 1.2.5, a second guidance

algorithm was chosen for the Mk-II ALTAV using the works of Rysdyk [40] and Osborne and Rysdyk [33]. The major advantage of this method is that it provides the desired setpoints for the Euler angles based on a continuous reduction of the cross-track error. Moreover, the method is able to compensate for the effect of winds on the airship without an explicit knowledge of the wind conditions. It will also be seen later how the guidance algorithm reduces the effective drag being experienced by the airship in the presence of cross-winds. The guidance algorithm in [33] and [40] is for 2-dimensional horizontal guidance of micro-UAV's. In the present work, we extend the method to 3-dimensions, while assuming a desired path composed of straight-lines. The results of the proposed guidance algorithm will then be compared against the performance of the guidance algorithm discussed in Section 3.3.1.

3.3.2.1 Wind Effects

We first make a distinction between the airship's true airspeed V_a and ground speed V_g expressed in the inertial NED frame as in Figure 3-13.

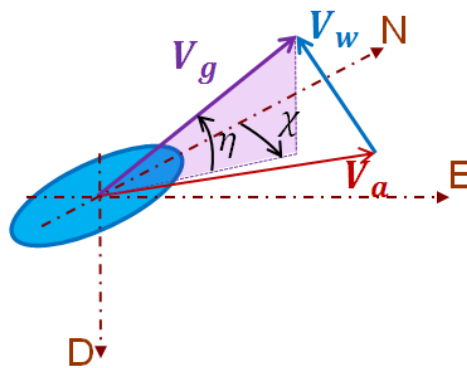


Figure 3-13: Illustration of airship's airspeed and groundspeed

The ground speed of the airship is the vector sum of its true airspeed and the wind velocity V_w i.e. $V_g = V_a + V_w$. Thus, the airspeed and groundspeed can be significantly

different in the presence of strong winds, especially for vehicles that have velocities comparable to the wind velocity. Since, the airship operates at $0 - 3 \text{ m/s}$, a wind speed of $5 \text{ knots} (\approx 2.6 \text{ m/s})$ would be comparable to the airship's operational speed. A guidance algorithm based on the ground-speed would therefore have inherent information of the wind that could be exploited. Thus, based on the ground-speed, we define the horizontal and vertical *course angles* χ and η as:

$$\chi = \text{atan2}(V_{g,E}, V_{g,N}) \quad (3.8)$$

$$\eta = \text{atan2}\left(-V_{g,D}, \sqrt{V_{g,N}^2 + V_{g,E}^2}\right) \quad (3.9)$$

where $\mathbf{V}_g = [V_{g,N} \ V_{g,E} \ V_{g,D}]^T$ is airship's ground speed vector expressed in the inertial *NED* frame.

3.3.2.2 The Desired Track's Track-Frame and Cross-Track Errors

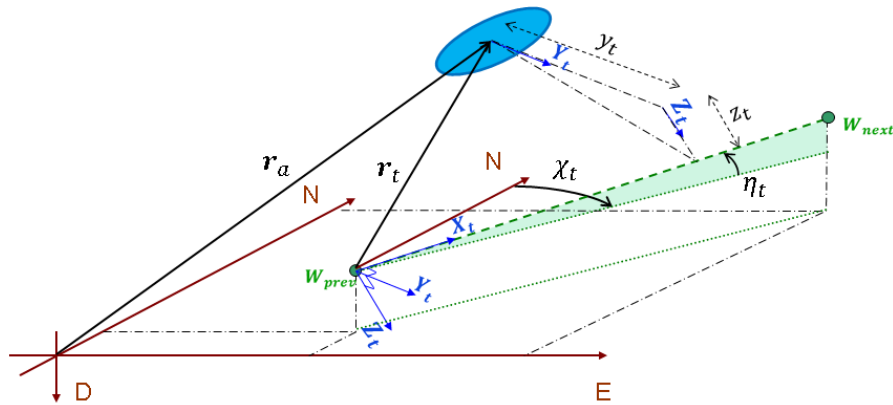


Figure 3-14: Track-frame orientation

The track frame $(X_t - Y_t - Z_t)$, with its origin at the starting point of the current wayline, has its X_t axis pointing to the target waypoint along the wayline. Its Y_t axis lies perpendicular to the X_t axis in a plane parallel to the *NE* plane, while the Z_t axis

completes the right-handed frame. Here we present the rotation matrix that transforms a vector from the inertial frame to the track-frame. The horizontal and vertical orientations of the desired wayline are given by χ_t and η_t as shown in Figure 3-14. The starting point of the desired wayline is given by $\mathbf{W}_{prev} = [W_{prev,x} \quad W_{prev,y} \quad W_{prev,z}]^T$.

Given the position of a point in the inertial NED frame, we can express the point in the track-frame using a combined rotation and translation, in sequence. The rotation matrix $\mathbf{R}_{i \rightarrow tr}$ that transforms a vector from the inertial frame to the track-frame can be computed by performing 2 body-fixed rotations about χ_t and η_t given by:

$$\mathbf{R}_{i \rightarrow tr} = \begin{bmatrix} \cos \eta_t & 0 & -\sin \eta_t \\ 0 & 1 & 0 \\ \sin \eta_t & 0 & \cos \eta_t \end{bmatrix} \begin{bmatrix} \cos \chi_t & \sin \chi_t & 0 \\ -\sin \chi_t & \cos \chi_t & 0 \\ 0 & 0 & 1 \end{bmatrix} = \begin{bmatrix} \cos \chi_t \cos \eta_t & \cos \eta_t \sin \chi_t & -\sin \eta_t \\ -\sin \chi_t & \cos \chi_t & 0 \\ \cos \chi_t \sin \eta_t & \sin \eta_t \sin \chi_t & \cos \eta_t \end{bmatrix} \quad (3.10)$$

Now, if the airship position in the inertial frame is $\mathbf{r}_a = [N_a \quad E_a \quad D_a]^T$, the airship position along X_t, Y_t and Z_t i.e. $\mathbf{r}_t = [x_t \quad y_t \quad z_t]^T$ (See Figure 3-14) can be calculated as:

$$\mathbf{r}_t = \mathbf{R}_{i \rightarrow tr} \mathbf{r}_a - \mathbf{W}_{prev} \quad (3.11)$$

Note that y_t and z_t are the cross-track errors. Finally, we define angles relative to the desired wayline. For angles measured with respect to the horizontal χ_t we use a *tilde* over-head and for angles measured with respect to the vertical η_t , we use a *hat* over-head, such that:

$$\widetilde{(\cdot)} \triangleq (\cdot) - \chi_t \quad \text{and} \quad \widehat{(\cdot)} \triangleq (\cdot) - \eta_t \quad (3.12)$$

3.3.2.3 Horizontal and Vertical Commanded Course Angles

Osborne and Rysdyk [33] propose a horizontal *commanded-course angle* χ_c which is the horizontal angle at which a vehicle must fly with to minimize, and eventually nullify, its

horizontal cross track error. According to the definition in Equation (3.12) $\tilde{\chi}_c$ represents the difference between the commanded course and the wayline heading. From [33] and [40], $\tilde{\chi}_c$ is generated based on the current cross-track of the airship by the function $\sigma(y_t)$ as:

$$\tilde{\chi}_c = \chi_c - \chi_t = \sigma(y_t) = \tilde{\chi}_{max} \left(\frac{e^{-\frac{a}{2}y_t} - 1}{e^{-\frac{a}{2}y_t} + 1} \right) \quad (3.13)$$

where $\tilde{\chi}_{max}$ represents the generated $\tilde{\chi}_c$ at large y_t and a determines the profile of the $\tilde{\chi}_c$ generated for intermediate values of y_t . Figure 3-15 shows how this functions varies with different values of a .

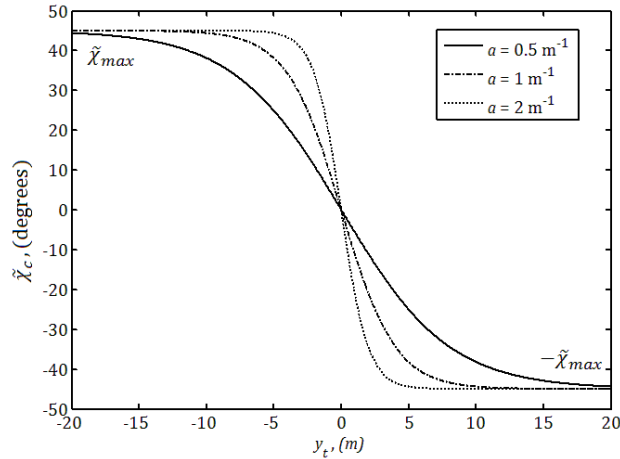


Figure 3-15: Function to generate $\tilde{\chi}_c$ as a function of y_t

The waypoint algorithm attempts to reduce the cross-track error while ensuring that the airship aligns itself with the local track (See Figure 3-16). The continuous profile of $\sigma(y_t)$ ensures a smooth convergence onto the wayline.

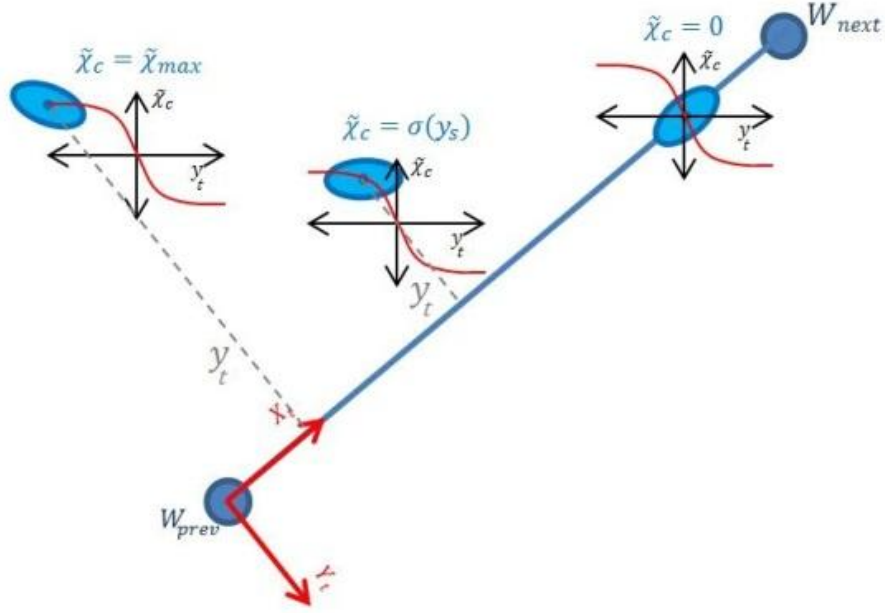


Figure 3-16: Illustration of proposed guidance strategy.

Extending the above concept, we propose a vertical commanded course angle η_c which is based on the vertical cross-track error (z_t) along the Z_t axis. In other words, z_t is the shortest distance from the airship to the $X_t - Y_t$ plane, measured along the Z_t axis. The function $\mu(z_t)$ which generates $\hat{\eta}_c$ based on the vertical cross-track error z_t is given by:

$$\hat{\eta}_c = \eta_c - \eta_t = \mu(z_t) = -\hat{\eta}_{max} \left(\frac{e^{-\frac{b}{2}z_t} - 1}{e^{-\frac{b}{2}z_t} + 1} \right) \quad (3.14)$$

where $\hat{\eta}_{max}$ is analogous to $\tilde{\chi}_{max}$ and b is analogous to a in Equation (3.13).

3.3.2.4 Generating the Desired State Setpoints

The LLC discussed previously in Section 3.2 requires 5 desired states $(\phi_d, \theta_d, \psi_d, u_d, h_d)$ which it attempts to track. Under fully autonomous control, these states are the outputs of the HLC as shown in Figure 3-1. In the following section, we will show how these setpoints are generated by the dynamics-based guidance algorithm based on knowledge of the course angles and the airship position.

Desired Yaw (ψ_d)

To design a control law that aims to make the airship fly along the commanded course specified by Equation (3.13), we first identify the error that needs to be minimized for successful guidance.

In the horizontal plane, this error would be $\tilde{\chi}_c - \tilde{\chi}$. That is, as $\tilde{\chi}_c - \tilde{\chi} = 0 \rightarrow \tilde{\chi}_c = \tilde{\chi}$. A variety of control laws can be used to minimize this error. We choose the PID control law that attempts to minimize this error, given as:

$$K_D(\dot{\tilde{\chi}}_c - \dot{\tilde{\chi}}) + K_P(\tilde{\chi}_c - \tilde{\chi}) + K_I \int_0^t (\tilde{\chi}_c - \tilde{\chi}) d\tau = 0 \quad (3.15)$$

Rearranging the above equation to isolate $\dot{\tilde{\chi}}$ to the left-hand-side of the equation:

$$\dot{\tilde{\chi}} = \dot{\tilde{\chi}}_c + K_{p_\chi}(\tilde{\chi}_c - \tilde{\chi}) + K_{i_\chi} \int_0^t (\tilde{\chi}_c - \tilde{\chi}) d\tau \quad (3.16)$$

where, $K_{p_\chi} = \frac{K_P}{K_D}$ and $K_{i_\chi} = \frac{K_I}{K_D}$ are the proportional and integral gains for the yaw-setpoint. We evaluate $\dot{\tilde{\chi}}_c$ by means of its definition in Equation (3.13):

$$\dot{\tilde{\chi}}_c = \frac{d}{dt}(\sigma(y_t)) = \frac{d}{dy_t}(\sigma(y_t)) \frac{dy_t}{dt} \quad (3.17)$$

where,

$$\frac{d}{dy_t}(\sigma(y_t)) = -a\tilde{\chi}_{max} \frac{e^{-\frac{a}{2}y_t}}{\left(e^{-\frac{a}{2}y_t} + 1\right)^2} \quad (3.18)$$

$\frac{dy_t}{dt}$ is the component of the ground speed of the airship along the Y_t axis of the track-frame. For completeness, Equation (3.19) below gives this decomposition along the X_t , Y_t and Z_t axes in terms of the course angles relative to the track frame $\tilde{\chi}$ and $\hat{\eta}$. Figure 3-17 diagrammatically illustrates how these velocities are determined.

$$\begin{aligned}
\frac{dx_t}{dt} &= V_{g,x_t} = V_g \cos \tilde{\chi} \cos \hat{\eta} \\
\frac{dy_t}{dt} &= V_{g,y_t} = V_g \sin \tilde{\chi} \cos \hat{\eta} \\
\frac{dz_t}{dt} &= V_{g,z_t} = -V_g \sin \hat{\eta}
\end{aligned} \tag{3.19}$$

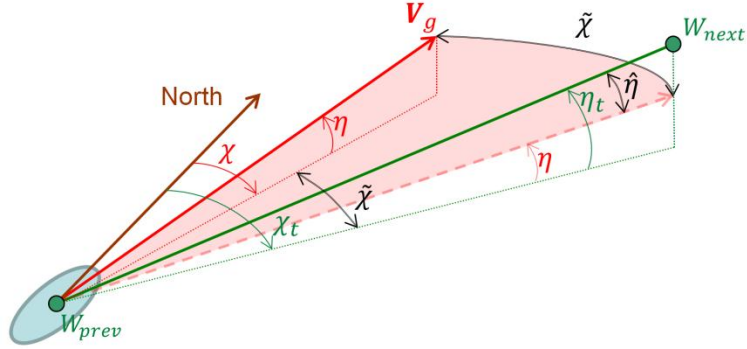


Figure 3-17: Diagrammatic illustration of angle-relations to represent ground speed in the track frame.

Equation (3.16) can be further simplified by noting that for straight-line paths, $\dot{\chi}_t = 0$. Therefore $\dot{\tilde{\chi}} = \dot{\chi} - \dot{\chi}_t = \dot{\chi}$. Furthermore, for our purpose, we choose $K_{i_\chi} = 0$, since for short distance flights, it is of little consequence. However, for long distance flights, including the integral gain could improve the guidance algorithm by nullifying steady-state cross-track errors.

As noted earlier, the LLC requires ψ_d input for horizontal guidance. This can be introduced into the dynamics by setting $\dot{\psi}_d = \dot{\chi}$ as our desired yaw-rate derivative for convergence. Finally, using $\frac{dy_t}{dt}$ from Equation (3.19) and $\frac{d}{dy_t}(\sigma(y_t))$ from Equation (3.18), we get the desired yaw-rate $\dot{\psi}_d$ for ideal convergence as:

$$\dot{\psi}_d = (V_g \sin \tilde{\chi} \cos \hat{\eta}) \left\{ -a \tilde{\chi}_{max} \frac{e^{-\frac{a}{2}y_t}}{\left(e^{-\frac{a}{2}y_t} + 1\right)^2} \right\} + K_{p_\chi} (\tilde{\chi}_c - \tilde{\chi}) \tag{3.20}$$

Finally the desired yaw set-point is found by integrating the above equation:

$$\psi_d(t) = \int_0^t \dot{\psi}_d(\tau) d\tau + \psi_d(0) \quad (3.21)$$

The above result has several implications. We first explain how the Equation (3.20) acts under *no* wind conditions. When the airship is away from the desired wayline ($\tilde{\chi}_c - \tilde{\chi} \neq 0$), the second term in Equation (3.20) will generate a non-zero $\dot{\psi}_d$. This results in the airship moving towards the desired wayline, and so its velocity transverse to the desired wayline $V_g \sin \tilde{\chi} \cos \hat{\eta} \neq 0$ which means the first term in Equation (3.20) is also not zero. However, once the airship has converged onto the path, both these terms will yield zero and the airship heading ψ and course χ will both be along the desired wayline ($\psi = \chi = \chi_t$).

Now under steady, uniform wind conditions, when the airship is away from the track, just as the no-wind case, the first two terms in Equation (3.20) will be non-zero. However, once the airship has converged onto the path, there is still a cross-wind that is pushing the airship away from the desired wayline making $V_g \sin \tilde{\chi} \cos \hat{\eta} \neq 0$. The first term in Equation (3.20) reacts to this by producing a value of $\dot{\psi}_d$ which tends to slightly orient the longitudinal axis of the airship against the cross-wind, as much as needed to counter its effect. Once the cross-wind has been countered, both the terms in Equation (3.20) tend to zero, thereby not producing any more change in ψ_d (i. e. $\dot{\psi}_d = 0$). The airship will then remain slightly oriented in the wind until the end of the current wayline. As well, the airship *course-angle* will be along the desired wayline, but the airship heading ψ will be slightly oriented into the wind as shown in Figure 3-18. Thus the above dynamics-based

guidance algorithm compensates for a cross-wind by slightly orienting the airship into the wind.

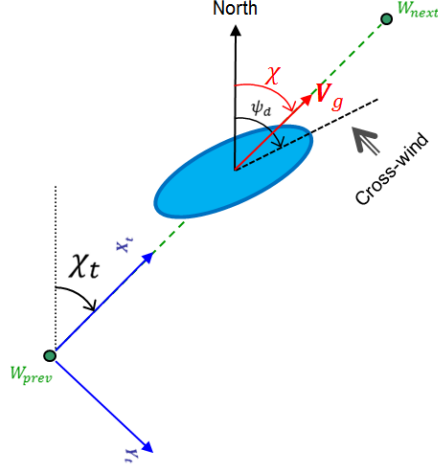


Figure 3-18: Wind compensation by the proposed guidance algorithm.

Desired Pitch (θ_d)

Following an approach similar to the previous section, we aim to minimize the error $\hat{\eta}_c - \hat{\eta}$, where $\hat{\eta} = \eta - \eta_t$ and $\hat{\eta}_c$ is specified by Equation (3.14). A regulator PID law, to eliminate $\hat{\eta}_c - \hat{\eta}$ is proposed such that,

$$K_{d_\eta}(\dot{\hat{\eta}}_c - \dot{\hat{\eta}}) + K_{p_\eta}(\hat{\eta}_c - \hat{\eta}) + K_{i_\eta} \int_0^t (\hat{\eta}_c - \hat{\eta}) d\tau \rightarrow 0 \quad (3.22)$$

Simplifying in a manner similar to that for the desired yaw, neglecting the integral part, and knowing that $\frac{dz_t}{dt} = V_{g,z_t} = -V_g \sin \hat{\eta}$, we get the following equation by setting $\dot{\theta}_d = \dot{\eta}$.

$$\dot{\theta}_d = -(V_g \sin \hat{\eta}) \left\{ b \hat{\eta}_{max} \frac{e^{-\frac{b}{2} z_t}}{\left(e^{-\frac{b}{2} z_t} + 1 \right)^2} \right\} + K_{P_\eta} (\hat{\eta}_c - \hat{\eta}) \quad (3.23)$$

where, $K_{P_\eta} = \frac{K_{p_\eta}}{K_{d_\eta}}$ is the proportional gain for the pitch setpoint.

$$\theta_d(t) = \int_0^t \dot{\theta}_d(\tau) d\tau + \theta_d(0) \quad (3.24)$$

To avoid very large pitch angles, we limit θ_d to $\pm 20^\circ$.

Desired Inertial Height (h_d)

Following the same approach as in the derivation of ψ_d and θ_d , in this case, we define an error $D_{tar} - D_a$ (See Figure 3-19). Thus a regulator PID law can be written as:

$$K_{d_h}(\dot{D}_{tar} - \dot{D}_a) + K_{p_h}(D_{tar} - D_a) + K_{i_h} \int_0^t (D_{tar} - D_a) d\tau \rightarrow 0 \quad (3.25)$$

Again, neglecting the integral part, and defining the ideal convergence dynamics as $\dot{h}_d = \dot{D}_a$, we get:

$$\dot{h}_d = K_{p_h}(D_{tar} - D_a) + \dot{D}_{tar} \quad (3.26)$$

where, $K_{p_h} = \frac{K_{p_h}}{K_{d_h}}$. Following up with an integration,

$$h_d(t) = \int_0^t \dot{h}_d(\tau) d\tau + h_d(0) \quad (3.27)$$

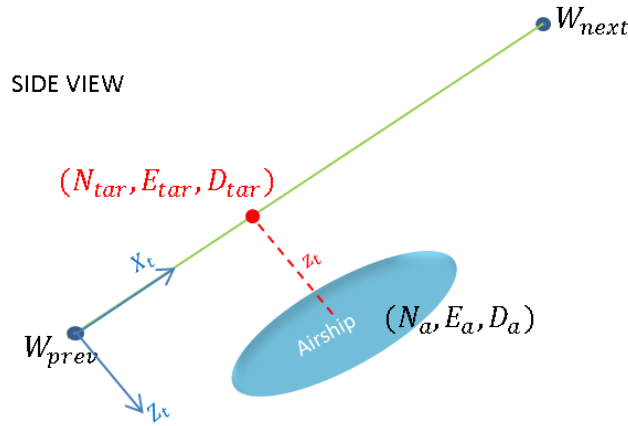


Figure 3-19: Desired height generation

Finally, the guidance algorithm in Section 3.3.1 used a constant u_d and ϕ_d and to allow a fair comparison between the controller proposed in this section and the one in Section 3.3.1. The same desired values of $u_d = 1 \frac{m}{s}$ and $\phi_d = 0^\circ$ were used.

3.3.2.5 Simulation Results

The simulation conditions are kept the same as Section 3.3.1.1. to allow a fair comparison of the current guidance method with the previous one. K_{p_χ} , K_{p_η} and K_{p_h} are chosen, through trial and error, as 0.1 s^{-1} , 0.1 s^{-1} and 0.2 s^{-1} respectively. $\tilde{\chi}_{max}$ and a are chosen as 45° and 1.2 m^{-1} while $\tilde{\eta}_{max}$ and b are 20° and 0.8 m^{-1} , respectively. Simulation results are presented for two wind conditions: 1) No Wind; 2) Wind at 3 *kph* (0.83 m/s) from the North and compared to the results with the non-dynamics based guidance algorithm. $\dot{\psi}_d$ and $\dot{\theta}_d$ generated are limited to $\pm 15^\circ/\text{s}$ and $\pm 5^\circ/\text{s}$, respectively.

Analysis Test Case 1

As can be seen in Figure 3-21 the new guidance algorithm shows a marked improvement over the previous one. The cross track error at the turns is reduced to less than 3 *m*, compared to around 6 *m* previously. Figure 3-22 shows the yaw profile during the test. As can be seen, under no wind conditions, the desired yaw eventually converges to the local track tangent. The low-level controller tracks the desired yaw very well, which is why the actual (solid) and desired (dotted) yaw profiles overlap. The pitch profile is shown in Figure 3-23. The airship begins to pitch nose up to intercept waylines sloping upwards, and begins to pitch down for waylines sloping downwards.

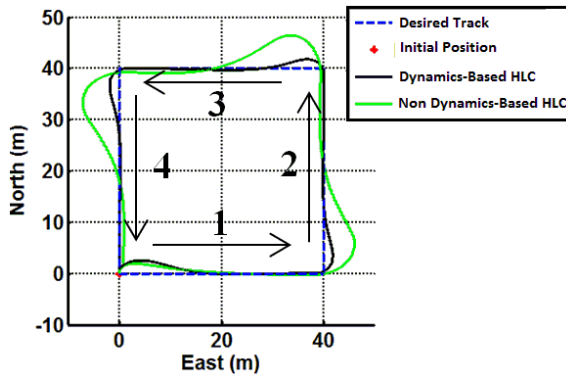


Figure 3-20: Airship trajectory in NE frame – test case 1

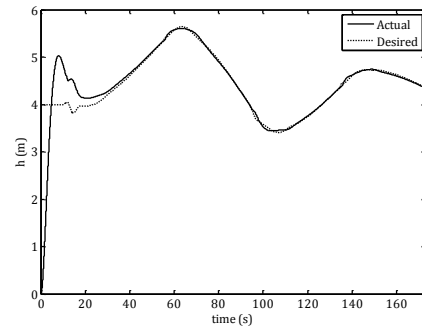


Figure 3-21: Height profile with dynamics based guidance algorithm - test case 1

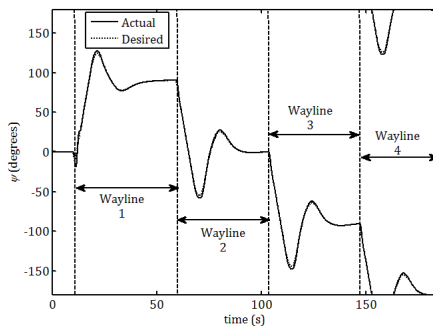


Figure 3-22: Yaw profile with the proposed waypoint controller – test case 1

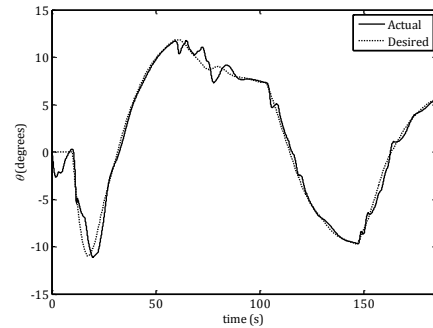


Figure 3-23: Pitch profile with the proposed waypoint controller - test case 1

A key advantage of this method is that at the instant when the desired track changes, the desired setpoint trajectories generated are always smooth, since the method relies on the integration of setpoint rates. For the same reason, during experiments, in case of unreliability/breaks in the sensor data (like the GPS or IMU), the desired setpoints generated will not change erratically. This improves stability during operation.

Analysis Test Case 2

All simulation conditions are the same as the previous case, except that we have a northerly wind at 3 *kph* ($\approx 0.83 \text{ m/s}$). The airship's motions are shown in Figures 3-24 - 3-27. Figure 3-24 compares the horizontal trajectory of the algorithm proposed in this section with the previous algorithm from Section 3.3.1.

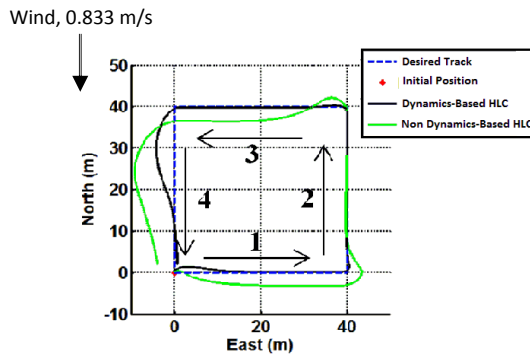


Figure 3-24: Airship trajectory in NED frame – test case 2

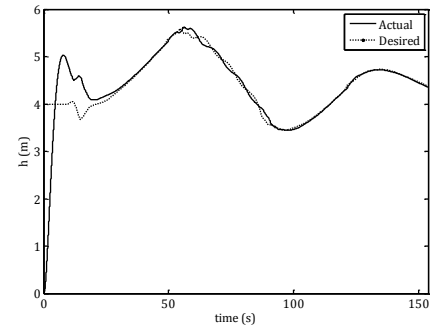


Figure 3-25: Height profile with dynamics based guidance algorithm - test case 2

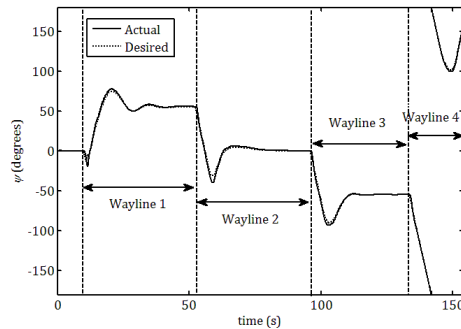


Figure 3-26: Yaw profile with dynamics based guidance algorithm - test case 2

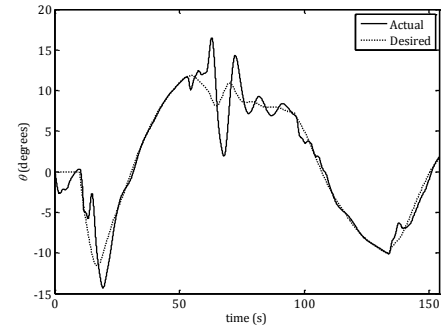


Figure 3-27: Pitch profile with dynamics based guidance algorithm - test case 2

As can be seen, the cross-track error during the flight has been almost entirely nullified. Figure 3-26 shows how this was achieved: the airship’s heading along wayline 1 does not converge to 90° , but rather converges to around 55° under the influence of the cross wind. The same is seen for wayline 3 where the airship converges to -55° instead of -90° . This indicates that a component of the inertial velocity perpendicular to the track counters the horizontal cross-wind and nullifies the cross-track error. A major advantage of this method is that while aligning slightly into the wind, the airship reduces its drag surface offered to the cross-wind. This further facilitates in reduction of the cross-track error. While encountering the second wayline ($54s < t < 97s$), the airship experiences a headwind. Thus, the heading converges to 0° in this case since no cross track errors are induced by the headwind. Also note the slight oscillations in the height and pitch profiles (Figures 3-25 and 3-27) during this time, since the airship is experiencing the

destablizing Munk moment. In the case of the final path ($t > 135s$), the airship experiences a tail wind that tends to push it forward, thus slowing the airship's convergence onto the path.

In summary, the proposed guidance algorithm successfully manages to guide the airship over the desired course in the presence winds comparable to the airship's speed. It achieves this without explicit knowledge of the wind since the airship has no on-board wind sensor. For a low-altitude airship, this is an important result since tight conformance to the path is important. By slightly orienting itself into the cross-wind the airship manages to achieve two goals, namely reduction of cross-track error and minimization of cross-flow drag.

Chapter 4 Flight Tests and Controller Validation

This chapter discusses the experimental flight testing carried out with the airship. The chapter starts by describing the airship's instrumentation including its sensors, actuators, data-acquisition, control architecture and communications. Two sets of flight tests were then carried out. The first set were conducted to determine key airship parameters, including the airship's heaviness, location of the center of gravity, normal drag coefficient, axial drag coefficient, rotational damping coefficient, lateral and longitudinal added masses, thruster reaction torques and Munk moment. The second set of flight tests were aimed at validating the controller suite (LLC and HLC) as developed in Chapter 3.

4.1 Experimental setup

4.1.1 Overall Architecture

As shown in Figure 4-1, the airship hull is a helium-filled polymer-envelope to which are attached four vectorable thrusters, a gondola, a GPS Antenna and an Inertial Measurement Unit (IMU). The gondola houses an on-board microcontroller, the communication peripherals for interfacing with the ground-station, an on-board GPS module and a sonar. The IMU is attached to the hull with a Velcro strip. The GPS antenna is located on top of the airship, diametrically opposite the gondola, with a cable that runs around the circumference from the antenna, to the GPS module in the gondola.

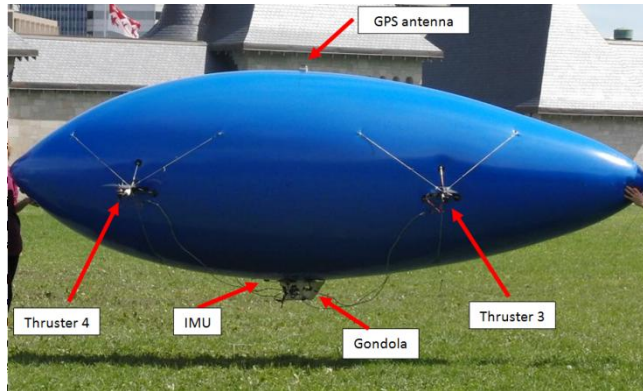


Figure 4-1: Flight setup of the airship.

4.1.2 DAQ and On-board Microcontroller

The QUARC microcontroller module, housed inside the gondola, is the main processing unit on-board the airship. It samples data from the sensors, runs the airship controller suite, and sends PWM outputs to the actuators. It also has a built-in WiFi communication module operating under the TCP/IP protocol to communicate with other hosts. The controller suite is implemented in Simulink which is supported by QUARC by means of the QUARC-Toolbox. The controller is compiled and downloaded onto the QUARC module using this toolbox. A ground station consisting of a laptop, a base GPS antenna/receiver pair and a joystick (Figures 4-2 to 4-5) is set up on the field. A GUI (Figure 4-2) running on the laptop displays the airship attitude and position data and provides a real-time interface to adjust the low-level controller gains and manually feed setpoints for the desired states. If the high-level controller is not engaged, setpoints for the desired values of yaw, forward velocity and height are fed through a joystick, as shown in Figure 4-3. The ground-station also logs all the relevant data. This data is acquired and the controller is implemented, both at an update rate of 50 Hz.

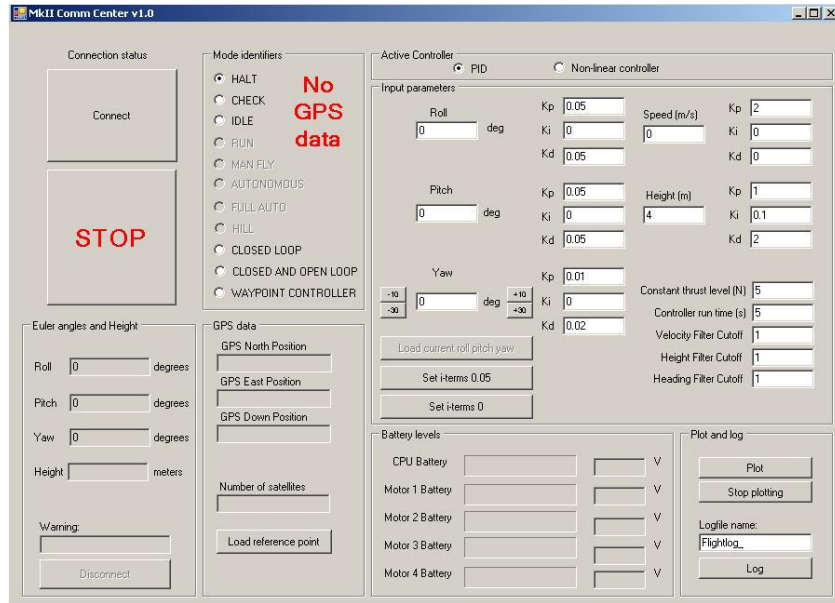


Figure 4-2: Airship GUI for field testing



Figure 4-3: Joystick to provide desired states when HLC is not engaged.



Figure 4-4: GPS base antenna



Figure 4-5: GPS base receiver

4.1.3 Thrusters

The overall thruster-servo arrangement has been shown previously in Figure 1-6. The airship is equipped with four vectorable thrusters, each actuated by means of a Hitec HS-322HD analog servo motor (Figure 4-6). The servo accepts a Pulse-Width-Modulated (PWM) signal from the microcontroller, the width of which governs the orientation of the servo shaft. The linear relationship between the pulse-width PW (in ms) and the servo angle α , in degrees, is given as [8]:

$$\alpha = 100(PW - 0.6) - 90 \quad (4.1)$$

The servo shaft is oriented such that its neutral position ($\alpha = 0^\circ$) corresponds to the thrust directed vertically upwards. Also, the servo shaft is constrained such that $\alpha \in [-90^\circ, 90^\circ]$. Therefore, the thrusters cannot produce a downward thrust.

A PJS 3D-1000N brushless motor (Figure 4-7) drives an APC 12'' \times 3.8'' constant pitch propeller (Figure 4-8). It has a motor constant K_v of 1240 rpm per Volt and has a nominal load current of 26 A [41]. Finally, a JETI Advance 30 Plus electronic-speed-controller (ESC; Figure 4-9) provides armature voltage commands to the brushless motor. It can supply up to 30 A current to the motor. As shown in Figure 4-10, the ESC is driven by a PWM signal generated by the microcontroller. The servo also draws its 5 V supply voltage from the ESC circuit.



Figure 4-6: Hitec HS-322HD servo motor



Figure 4-7: PJS 3D-1000N brushless motor



Figure 4-8: APC 12'' \times 3.8'' propeller



Figure 4-9: JETI Advance 30 Plus ESC

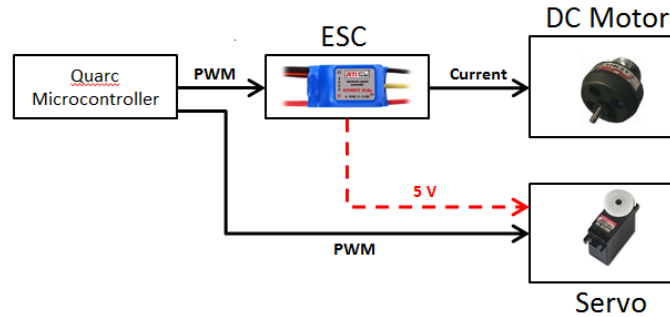


Figure 4-10: Schematic of the thruster setup

4.1.4 Sensors

4.1.4.1 IMU

The airship is equipped with a Microstrain 3DM-GX3-25-OEM™ Inertial Measurement Unit (IMU; Figure 4-11) for measurement of attitude, angular rate and linear accelerations data. It interfaces with the microcontroller via the RS-232 serial protocol, at an update rate of 20 Hz. It measures 38 mm × 24 mm × 12 mm and weighs 11.5 grams.

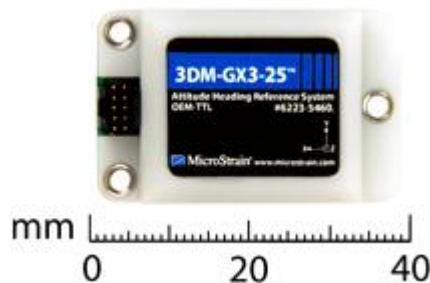


Figure 4-11: Microstrain 3DM-GX3-25-OEM™ Inertial Measurement Unit

4.1.4.2 GPS

Two GPS configurations were used during our tests: a single GPS (SGPS) configuration that uses only one airborne set of antenna and receiver; and a differential GPS (DGPS) configuration that makes use of two antennas and two receivers, with one set airborne and the other set near the ground station. With a less-complex communication setup and a

less-complex algorithm to compute a solution, the SGPS configuration is more robust relative to the DGPS configuration. However, the SGPS configuration provides less accurate position data than the DGPS configuration: the DGPS setup is capable of centimeter-level accuracy, while the SGPS only provides meter-level accuracy. The DGPS configuration was thus used for model validation presented in Section 4.2. The SGPS configuration is more representative of actual operation of an autonomous airship, and was used for the outdoor tests presented in Section 4.3.

Differential GPS Configuration

This setup used two receiver/antenna pairs; one on the airship, and the other located near the ground station. The on-board GPS used an Antcom 1G1215A-XS-4 dual-frequency antenna mounted at the top of the hull, connected to a Novatel OEM42GL receiver, housed in the gondola. The raw data from the onboard unit was sent over a Wi-Fi network to the ground station.

The base system antenna-receiver pair consists of a Novatel GPS-702-GG base antenna (Figure 4-4) and a Novatel DL-V Series base receiver (Figure 4-5). Its data was used, in conjunction with the on-board GPS data, by Waypoint's RTK-NAV software running on the ground station laptop, to calculate a precise solution for the inertial position and velocity of the airborne antenna. The DGPS approach uses algorithms to identify and cancel errors that are present in both the airborne and base data-sets [42]. The GPS solution is communicated back to the QUARC module over the Wi-Fi network, to be used along with the IMU and sensor data by the controller suite to compute the

appropriate thruster forces. The DGPS can compute up to 10 solutions per second. A schematic of this setup is shown in Figure 4-12.

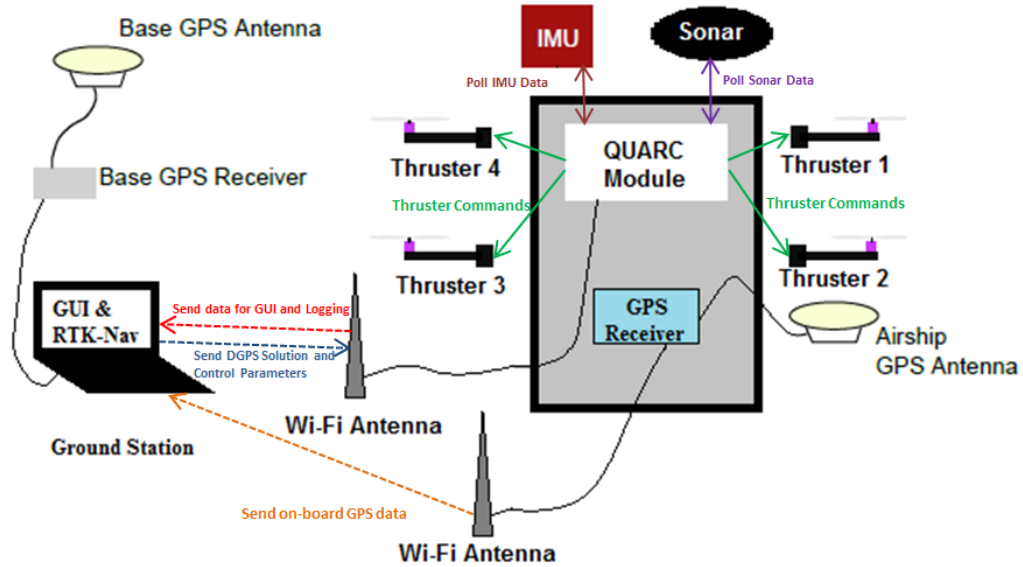


Figure 4-12: System configuration with DGPS

Single GPS Configuration

In this setup (Figure 4-13), the solution computed by the on-board GPS antenna and receiver is sent directly to the QUARC module, rather than sending raw GPS data to the ground station. This solution, along with the IMU and sonar measurements, is then used by the controller suite to compute the thruster forces. All relevant data is then sent over the Wi-Fi network to the ground station for logging.

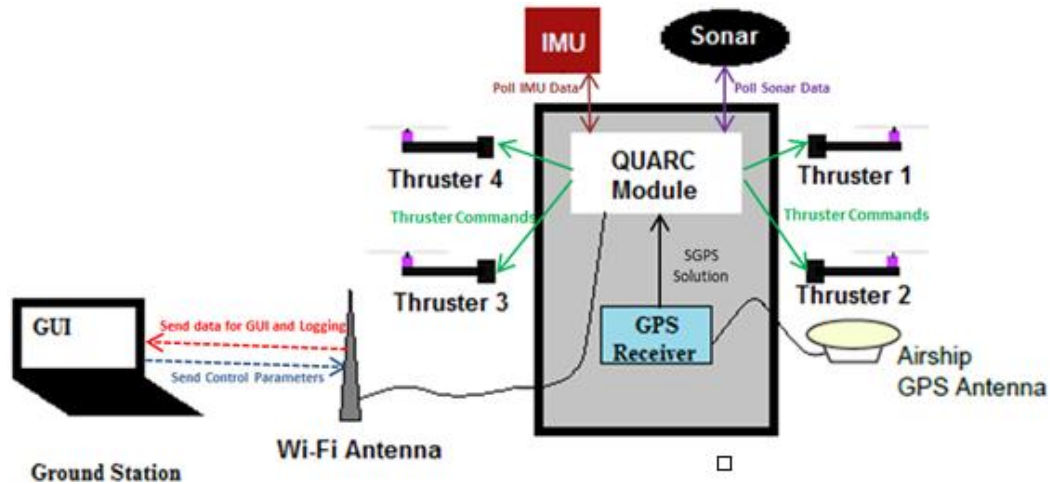


Figure 4-13: System configuration with SGPS

4.1.4.3 Sonar

An MB 1260 XL –MaxSonar-EZL0 sonar (Figure 4-14) is attached at the bottom of the gondola to provide a line of sight distance to the ground (or nearest obstacle). The sonar, which is only used with the SGPS configuration during outdoor tests, is to some extent, a redundant height measurement system since the GPS provides the inertial height relative to the base station. However, each device has its own shortcomings. The accuracy of the GPS depends on the number of satellites detected by the antenna and any loss of satellites compromises the GPS solution. The sonar performance relies on the surface of reflection and for outdoor tests, this surface is grass, thus limiting the range of measurements to below $\approx 6\text{ m}$. Therefore, in outdoor tests, where the SGPS setup is used, if the airship is below $\approx 6\text{ m}$, we use sonar readings as height measurements. If sonar readings lie beyond $\approx 6\text{ m}$, for 5 successive measurements, an algorithm identifies these measurements as outliers and switches to the GPS height measurements. During tests using the DGPS setup, only the GPS height measurements are used.



Figure 4-14: MB 1260 XL –MaxSonar-EZL0 sonar

4.1.4.4 Wind Sensor

During outdoor tests for validation of the high-level controller, a ground-based wind sensor, shown in Figure 4-15, was used. The wind sensor is a WindSonic™ 2-axis ultrasonic sensor providing wind speed and direction. It can measure wind speeds between 0 – 60 m/s and wind directions between 0 – 359°, at an update rate of 20 Hz . A 0° wind direction corresponds to a wind directed from the North while 90° corresponds to a wind directed from the East.

This data is not used by the controller, and is used only to validate controller performance in winds during post-processing. It is located next to the ground station at a height of $\approx 7 m$, thus providing only average wind conditions over time and not the specific wind conditions at the airship location. It communicates with the ground-station using the RS-232 serial protocol.



Figure 4-15: WindSonic 2-Axis ultrasonic anemometer

4.2 Validation of Airship Dynamics Model

In this section, we will discuss tests that were carried out to validate certain airship parameters as estimated by Peddiraju [8] and in the current thesis. Specifically, these parameters are the airship's net heaviness h_a ; the horizontal location of the airship's

center of gravity x_{cg} and y_{cg} ; the cross-flow drag coefficient C_d ; the axial drag coefficient C_{A_0} ; the rotational damping coefficient k_ω ; added masses in the longitudinal and lateral directions m_{11} and m_{22} , respectively; the thruster reaction torques; and the presence of the Munk moment.

Two flight tests were conducted on the 12th April, 2012 and the 15th April, 2012 in an indoor sports facility, called the ‘Stinger Dome’[43], shown in Figure 4-16. This facility has nearly zero wind conditions, making it a suitable choice for these tests. The maximum height of the dome is about 13 m. The dome is transparent to radio signals, thereby allowing the use of GPS indoors. The DGPS configuration was used for horizontal position, velocity and inertial height measurements. The sonar data was not used during these tests.



Stinger Dome / Loyola Campus - photo Stephan Jahanshahi

Figure 4-16: Concordia Stinger Dome[43]

4.2.1 Airship Pre-flight and Post-Flight Measurements

For proper validation of the dynamics model, the airship should be inflated such that its physical properties match those used in the simulation model. Therefore, before and after each flight test day, the airship circumference at its largest diameter, the airship’s internal pressure and the airship’s net heaviness were measured using a tape measure, a pressure gauge and a weighing scale. These measurements are tabulated in Table 4-1.

Table 4-1: Airship's pre-flight and post-flight measurements

	12 th April, 2012			15 th April, 2012		
	Start	End	Average	Start	End	Average
Circumference, C (m)	4.68	4.64	4.66	4.62	4.58	4.60
Internal Pressure, P_{int} (mBar)	3.80	3.41	3.61	3.79	3.01	3.40
Heaviness, h_a (kg)	0.673	0.695	0.684	0.668	0.745	0.707

From the above values, we would like to have an estimate of the gross inertial mass m of the airship (including the helium and all other attachments), which is needed in the later sections. The average airship circumference allows us to find the corresponding average airship radius for each flight test day. The inertial mass m , in terms of the heaviness h_a and volume V can be found from:

$$m = h_a + \rho V \quad (4.2)$$

where ρ is the density of the ambient air. We can estimate V by using the relationship between the internal pressure P_{int} and V , that was tabulated in Table 2-2 in [8]. These calculated values are shown in Table 4-2 below.

Table 4-2: Calculated parameters of the airship hull

	12 th April, 2012	15 th April, 2012
Radius, r (m)	0.74	0.73
Volume, V (m ³)	4.50	4.47
Inertial mass, m (kg)	6.10	6.09

Finally, for the tests carried out using the PID controller in the upcoming sections, the values of the gains used are the same as those used in the simulations (See Table 3-1), except for the proportional and derivative height gains. Undesirable vertical oscillatory motion observed with the previous gains and so they were adjusted. The tuned values are

$$k_{P,h} = 0.5 \frac{N}{m}, k_{D,h} = 1.6 \frac{N}{(m/s)}.$$

4.2.2 Heaviness and Center of Gravity Location Test

This flight was conducted on 15th April, 2012. In this test we use the PID controller to make the airship hover at a desired height of 4 m. During this closed-loop maneuver, the desired thruster inputs (which are the desired thrusts and servo angles) are computed and recorded. During post-processing, these thruster commands are used to estimate the heaviness of the airship. It is thus important to note, that any errors/approximations in the thruster model, would affect the results of these tests.

The inertial height and the thrust in the z -direction from each of the four thrusters are shown in Figure 4-17 and Figure 4-18, respectively. Figure 4-19 shows the filtered values of thrusts using a 2nd order Butterworth filter at a cutoff frequency of 100 Hz. Filtered values are shown for visibility purposes only and are *not* used in the subsequent calculations. The total thrust in the z -direction from all four thrusters T_z is averaged over the time period between $t = 10 \rightarrow 25s$ (when the airship has stabilized at the desired height) and is found to be $T_z = 6.91 N$. The heaviness can be calculated as $h_a = \frac{T_z}{g}$, where g is the acceleration due to gravity ($g = 9.806 m/s^2$) yielding $h_a = 0.704 kg$, which matches the measurements tabulated in Table 4-1 almost perfectly. Apart from validating the heaviness of the airship, this exercise also validates the accuracy of the steady-state thruster model.

We now estimate the location of the center of gravity, based on the thruster data, using a moment balance about the center of buoyancy (CoB). The CoB has been previously estimated to lie at about 2.210 m from the nose of the hull in Section 2.5.2. From Figure 4-20, we can find a relation between the thruster forces and the location of the center of

gravity in the horizontal plane $\mathbf{r}'_{CG} = [x_{cg} \quad y_{cg} \quad 0]^T$ relative to the center of buoyancy. Peddiraju [8] used a similar approach to find x_{cg} based on load cell measurements with the airship suspended from the ceiling. From Figure 4-20, the moment balance relation yields an equation for the \mathbf{r}'_{CG} in terms of the average thrust of the i 'th thruster in the z -direction $\mathbf{T}_{z,i} = [0 \quad 0 \quad -T_{z,i}]^T$ and their distances from the CoB on the xy -plane $\mathbf{r}_i = [r_{x,i} \quad r_{y,i} \quad 0]^T$:

$$\mathbf{r}'_{CG} \times [0 \quad 0 \quad mg]^T + \sum_{i=1}^4 \mathbf{r}_i \times \mathbf{T}_{z,i} = \mathbf{0} \quad (4.3)$$

which can be solved to isolate x_{cg} and y_{cg} as:

$$\begin{bmatrix} x_{cg} \\ y_{cg} \\ 0 \end{bmatrix} = \frac{1}{mg} \begin{bmatrix} \sum_{i=1}^4 r_{x,i} T_{z,i} \\ \sum_{i=1}^4 r_{y,i} T_{z,i} \\ 0 \end{bmatrix} \quad (4.4)$$

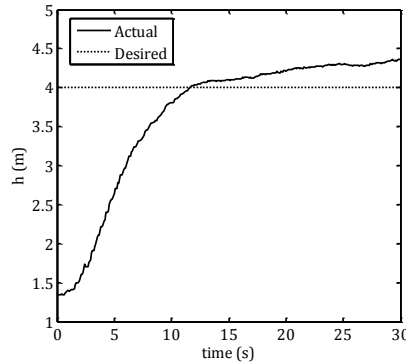


Figure 4-17: Inertial height during heaviness test

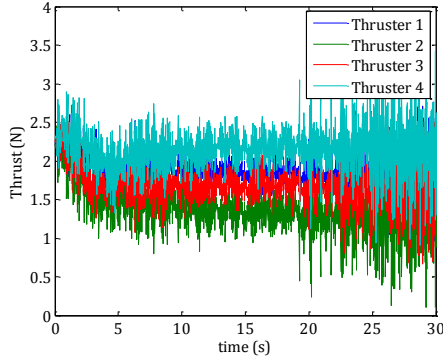


Figure 4-18: Raw thruster forces in z during heaviness tests

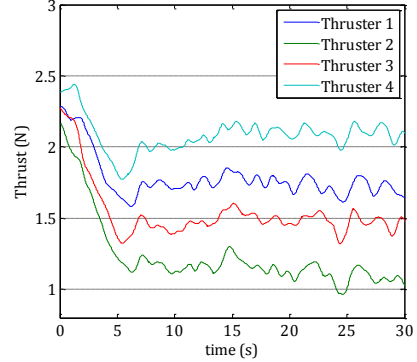


Figure 4-19: Filtered thruster forces in z during heaviness test

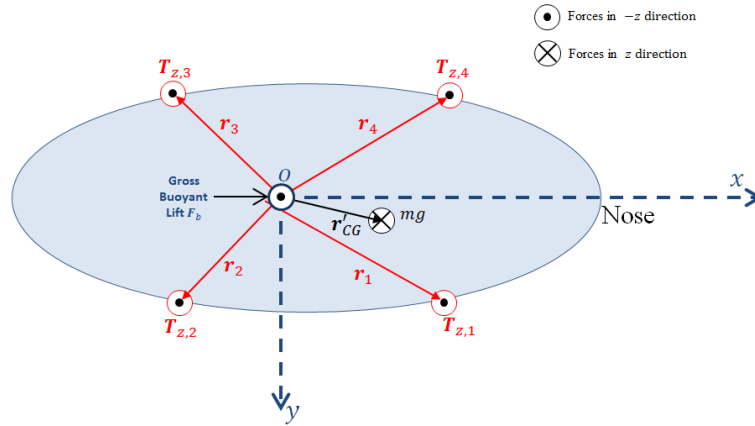


Figure 4-20: Moment balance during hover, top view.

It is important to note that Equation (4.4) only holds true if the airship is hovering in level flight i.e. roll ϕ and pitch θ must be held near zero. Averaged between $t = 10 \rightarrow 25$ s, the average values recorded for the roll and pitch angles were $\phi = -0.77^\circ$ and $\theta = -0.25^\circ$, which are acceptable for the purposes of this test. Now, using $m = 6.09$ kg from Table 4-2, the values for r_i from Table 4-3 (values from [8]) and average values of the thrusts in the z -directions between $t = 10 \rightarrow 25$ s as $T_{z,1} = 1.802$ N, $T_{z,2} = 1.323$ N, $T_{z,3} = 1.651$ N and $T_{z,4} = 2.134$ N, we find $x_{cg} = 0.0262$ m and $y_{cg} = -0.009$ m. The value determined for x_{cg} corresponds very closely to that determined by our CAD model (Section 2.4.) as $x_{cg} = 0.027$ m. The value determined for y_{cg} is not 0 m (as determined by the CAD model and assumed in the simulation model), likely due to asymmetries in

the assembly of the airship, by virtue of the hanging cables, imperfect placement of thrusters, gondola, sonar, IMU etc.

Table 4-3: Airship thruster locations in the body-frame [8]

Thruster number, i	$r_{x,i}$ (m)	$r_{y,i}$ (m)	$r_{z,i}$ (m)
1	1.172	0.994	0
2	-1.025	0.977	0
3	-1.025	-0.977	0
4	1.172	-0.994	0

4.2.3 Normal Drag Test

This test was carried out on the 12th April, 2012. In this test, we aim to determine the normal-drag coefficient C_d of the airship and compare it to that predicted in Appendix C.

The airship is made to hover at a desired height of 12 m. Once stable, all four thrusters are switched off and the airship falls freely under gravity. Due to the drag on the hull, the airship eventually reaches a steady-state terminal downwards velocity w_{ss} before it reaches the ground. A force balance on the airship in this state is shown in Figure 4-21. Under these conditions the total normal force (drag) acting on the airship D_N can be given as:

$$D_N = \frac{1}{2} \rho w_{ss}^2 A_p C_d \quad (4.5)$$

Equation (4.5) is rearranged to solve for C_d while taking into account that $D_N = mg - F_b = (m - \rho V)g = h_a g$. This yields,

$$C_d = \frac{2h_a g}{\rho w_{ss}^2 A_p} \quad (4.6)$$

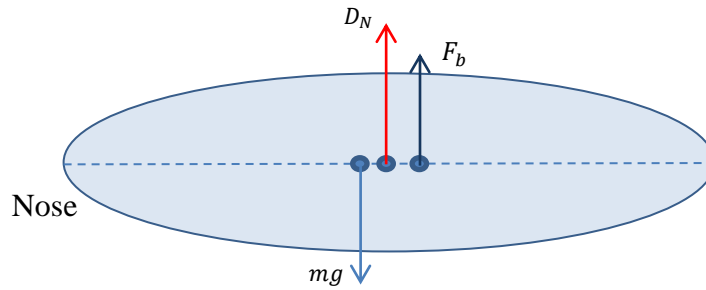


Figure 4-21: Force balance for the drop test under terminal velocity conditions

The results for all 3 tests performed for this experiment are tabulated in Table 4-5. These tests were conducted on the 12th April, 2012. For test case A, the airship’s height during the fall and the corresponding velocity in the z -direction are shown in Figure 4-22 and Figure 4-23, respectively (see Appendix E for other results). Note that the airship’s GPS velocity shown in Figure 4-23 is not calculated by simple differentiation of the airship’s height in Figure 4-22. Rather, the airship’s GPS velocity is calculated by the RTK-NAV software using a method based on Doppler measurements. Furthermore, the heaviness is known from Table 4-1 as $h_a = 0.684 \text{ kg}$, and from Table 2-4, $A_p = 5.204 \text{ m}^2$.

Table 4-4: Summary of results for normal drag test

Test Case	$w_{ss} \text{ (m/s)}$	C_d
A	1.75	0.699
B	1.86	0.619
C	1.77	0.683

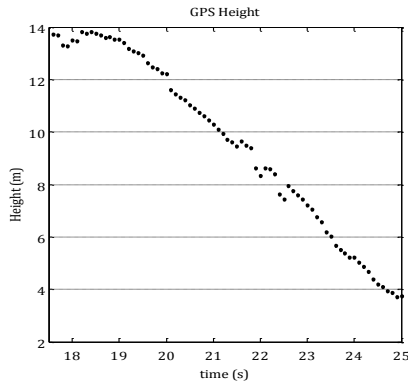


Figure 4-22: Inertial height during drop test – Test case A

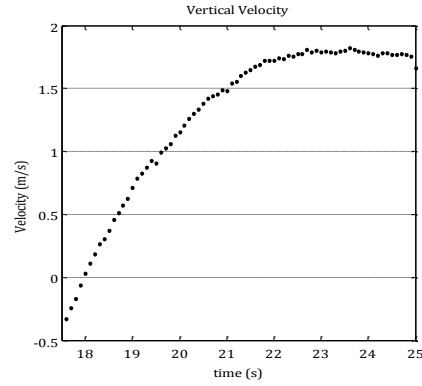


Figure 4-23: Downward velocity during drop test – Test case A

From Table 4-4, the results for C_d from the three tests seem consistent with an average value over three tests of 0.667. Appendix C provides details on an empirical approach based on published wind tunnel data to estimate this drag coefficient, leading to a value of 0.67. In Appendix C, the drag coefficient was also estimated using a method adopted by Allen [44], leading to a value of 0.72. This estimate was obtained by applying a drag proportionality factor η to the drag coefficient of an infinite 2-D cylinder. The experimental result, therefore, is closer to the value estimated through the empirical approach in Appendix C.

4.2.4 Axial Drag Test

This test aims to experimentally evaluate the axial drag coefficient C_{A_0} of the hull and compare this value to that estimated in Section 2.2.2.

In this test, the airship is commanded to fly at a constant forward speed while keeping all other desired states fixed. Figure 4-24 shows the force balance of the airship at steady state forward velocity. From this figure the sum of the commanded thrusts in x -direction

must equal the total aerodynamic drag $D_u = \frac{1}{2} \rho u^2 A_f C_{A_0}$ on the airship. Thus,

$$\sum_{i=1}^4 T_{x,i} = \frac{1}{2} \rho u^2 A_f C_{A_0} \quad (4.7)$$

where, C_{A_0} is the axial drag coefficient and A_f is the frontal area of the airship.

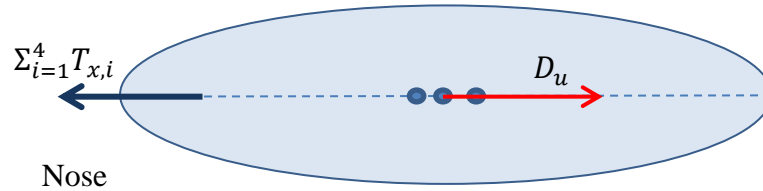


Figure 4-24: Steady-state force balance in x -direction - forward drag test

The results for all 6 tests performed for this experiment are tabulated in Table 4-5. The total commanded thrust in the x -direction due to all four thrusters and the corresponding forward velocity for test case A are plotted in Figure 4-25 and Figure 4-26, respectively (See 0 for the remaining test cases).

Table 4-5: Results for forward drag test. Test cases A-F

Test Case	Avg. over time (s)	Avg. forward velocity (m/s)	Avg. $\sum_{i=1}^4 T_{x,i}$ (N)
A	255→265	0.491	1.015
B	106→115	0.550	1.026
C	200→210	0.590	0.852
D	136→146	0.760	1.066
E	35→45	0.890	0.963
F	60→66	1.020	1.300

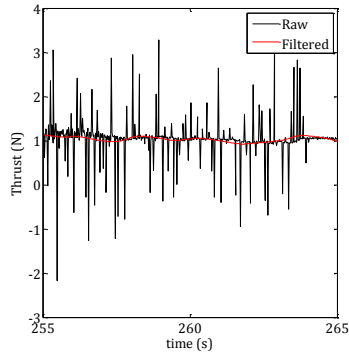


Figure 4-25: Total thrust in x , test case A

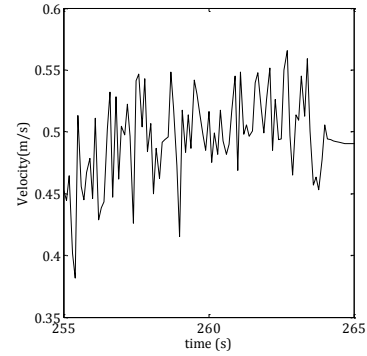


Figure 4-26: Forward velocity, test case A

From Figure 4-25 large spikes are apparent in the commanded thrust, indicating high frequency jitter in the servo inputs. This is largely caused by the response of the PID controller to sensor inputs with high-frequency noise.

For each test case, the average value of $\sum_{i=1}^4 T_{x,i}$ is plotted against the average value of u^2 in Figure 4-27. We find the least-square-error linear fit for these points, bounded at $(0,0)$, the slope of which is $\frac{1}{2}\rho A_f C_{A_0}$. Using $A_f = 1.77 \text{ m}^2$ and $\rho = 1.204 \text{ kg/m}^3$, we find $C_{A_0} \approx 1.5$.

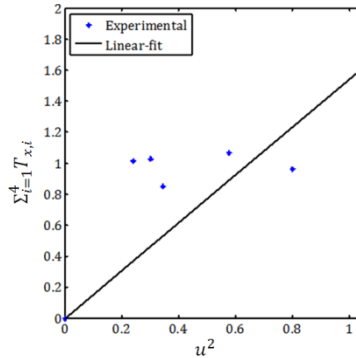


Figure 4-27: Linear fit to determine the forward drag coefficient.

We first note that the data points in Figure 4-27 are very scattered and far from lying on a straight line, indicating poor experimental results. A possible explanation for this can be found in the large spikes in Figure 4-25. These spikes indicate that the thruster commands

were quite erratic and that the thrusters were not operating in steady-state, and therefore producing a very different output than that predicted by a steady-state model. As a result, the average thrust values in Table 4-5 may contain a large error. Beyond this, the final result obtained above for C_{A_0} shows a very large discrepancy from the theoretically predicted value in Section 2.2.2 of $C_{A_0} = 0.058$. By itself, the drag due to protuberances cannot be the cause for such a large difference.

Apart from the drag due to protuberances, another factor that could significantly lead to an increased overall drag in the forward direction would be the presence of the thrusters, which completely change the airflow around the airship hull during flight. For conventional concept airships, such as the LZ-129 (Figure 1-2) or the LEMV (Figure 1-3), the size of the propellers relative to the hull is small, thus implying that they will have a small effect on the airflow around the hull. The Mk-II ALTAV, however, derives a good part of its lift from the propellers, thus requiring the use of relatively large propellers that significantly change the overall airflow around the airship. Figure 4-28 shows a conceptual schematic of the potential flow around the airship in forward flight without thrusters, while Figure 4-29 shows a possible representation of the airflow around the airship in forward flight, as influenced by the thrusters. The dramatic difference between these two airflow profiles indicates that it is likely not valid to estimate the forward drag coefficient of the airship with thrusters while not taking to account the effect of the thrusters. We conclude from this test that the forward drag coefficient of the airship is likely much higher than the empirically estimated one. However, the quality of our results is questionable and the empirically-estimated value of $C_{A_0} = 1.5$ is unlikely to be correct. It is therefore left as future work to investigate this more fully.

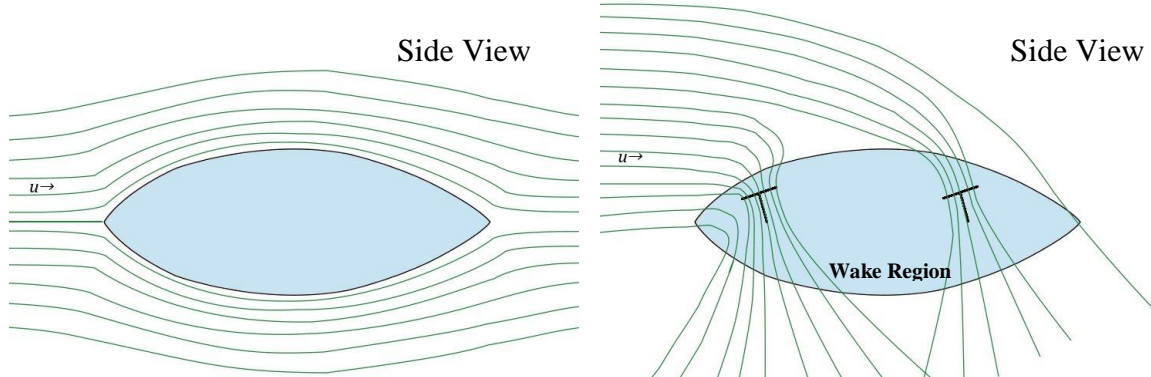


Figure 4-28: Flow over the airship hull without thrusters.

Figure 4-29: Flow over the airship hull with thrusters in operation.

4.2.5 Damping Moment Coefficient Test

In this experiment, we aim to experimentally estimate the rotational damping moment coefficient k_ω , for a pure yawing motion r of the airship. The test is constructed to make use of the relationship given by Equation (2.14) when the pitch-rate $q = 0$, i.e. $M_{D,r} = k_\omega r^2$.

The PID controller on-board the airship which controls 5 independent states $[u \ w \ \phi \ \theta \ \psi]^T$ is modified so that it controls the yaw-rate r instead of the yaw-angle ψ .

The yaw controller is given by Equation (3.1) is therefore replaced by:

$$\begin{bmatrix} T_{1x,r} \\ T_{2x,r} \\ T_{3x,r} \\ T_{4x,r} \end{bmatrix} = \begin{bmatrix} -k_{P,r} \\ -k_{P,r} \\ k_{P,r} \\ k_{P,r} \end{bmatrix} (r_d - r) + \begin{bmatrix} -k_{I,r} \\ -k_{I,r} \\ k_{I,r} \\ k_{I,r} \end{bmatrix} \int (r_d - r) dt + \begin{bmatrix} -k_{D,r} \\ -k_{D,r} \\ k_{D,r} \\ k_{D,r} \end{bmatrix} (\dot{r}_d - \dot{r}) \quad (4.8)$$

Where $T_{ix,r}$ represents the thrusts generated by the i 'th thruster in the x -direction to control the state r , r_d is the desired yaw-rate and $k_{P,r}$, $k_{I,r}$ and $k_{D,r}$ are the P, I and D gains, respectively. These gains were tuned in the simulation model resulting in $k_{P,r} = 0.05 \text{ N}/\frac{\text{deg}}{\text{s}}$, $k_{I,r} = 0.05 \text{ N}/\text{deg}$, $k_{D,r} = 0 \text{ N}/\frac{\text{deg}}{\text{s}^2}$, and the same gains were used in the experiment. During the experiment, the airship is first commanded to hover at a given

height of 4 m. Once stable, four different desired non-zero yaw-rates of $40 \frac{deg}{s}$ ($t = 35 s$), $60 \frac{deg}{s}$ ($t = 274 s$), $80 \frac{deg}{s}$ ($t = 68 s$) and $120 \frac{deg}{s}$ ($t = 298 s$) are commanded, in succession.

We find the total thruster moment acting on the airship as follows:

$$M_{z,thruster} = \sum_{i=1}^4 (r_{y,i} T_{x,i}) \quad (2.40)$$

where, $T_{x,i}$ is the thrust commanded from the thruster i in the x -direction and $r_{y,i}$ is the moment arm of the i 'th thruster in the y -direction. The resulting moment $M_{z,thruster}$ and the corresponding yaw-rate profiles are shown in Figure 4-30 and Figure 4-31, respectively.

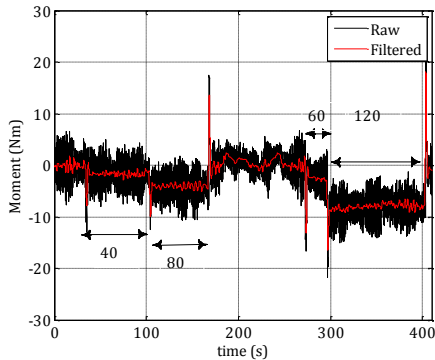


Figure 4-30: Total thruster-induced moment during estimation of rotational damping coefficient.

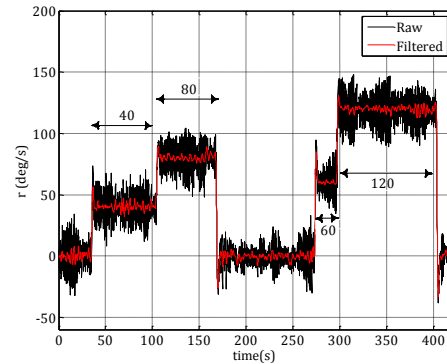


Figure 4-31: Yaw-rate during estimation of rotational damping coefficient

The moment and yaw-rate were filtered using a second-order Butterworth low-pass filter with a cut-off frequency of 100 Hz. These filtered values are shown on each plot². The bi-directional arrows within the plots show corresponding commanded yaw-rates.

² Filtering has only been applied for plotting; filtered values were not used in the calculations that follow.

During steady-state rotation of the airship, we can presume that the total drag moment $M_{D,z}$ acting on the airship is equal to the total moment generated by the thrusters and the reaction torques in the z-direction. Therefore, in steady-state rotation,

$$M_{z,thruster} = k_{\omega} \cdot r^2 \quad (2.41)$$

The following table lists the average values of $M_{z,thruster}$ obtained by averaging over the time intervals indicated in the second column.

Table 4-6: List of calculated values for experimental estimation of k_{ω}

Commanded r ($\frac{deg}{s}$)	Averaged over time (s)	Measured average r ($\frac{deg}{s}$)	$M_{z,thruster}$ (Nm)
40	43→90	41.24	1.95
60	277→295	60.77	2.860
80	114→160	80.54	4.30
120	340→395	122.10	8.08

We now plot $M_{z,thruster}$ vs r^2 . We also add (0,0) to the plot below to account for $M_{z,thruster}|_{r=0} = 0 \text{ Nm}$. A least-square-error linear fit, bounded at (0,0) is shown in Figure 4-32. The slope of the least squares linear fit in Figure 4-32 results in a value $k_{\omega} \approx 2 \frac{Nm}{(rad/s)^2}$, while the theoretically predicted value for this coefficient determined in Section 2.2.1, was $k_{\omega} \approx 4.42 \frac{Nm}{(rad/s)^2}$.

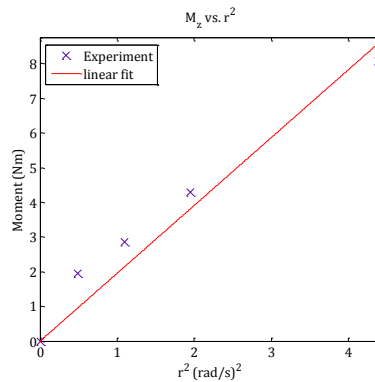


Figure 4-32: $M_{z,thruster}$ vs. r^2 ; experimental data points and linear fit

Since the approach used to determine k_ω in Section 2.2.1 was quite detailed, it is likely that the assumptions made in Section 2.2.1 do not represent the conditions in the experiment. In particular, we expect that, as was the case in the axial drag test, the presence and action of the thrusters leads to a large modification of the flow around the hull. We, therefore conclude that to properly estimate k_ω using empirical methods, the effect of the thrusters must be accounted for.

4.2.6 Experimental Determination of Added Masses

In the following two sub-sections we perform experiments to determine the longitudinal and lateral added masses.

4.2.6.1 Longitudinal Added Mass

In this test, the airship is first commanded to hover at a desired height at the start of the experiment. Once in closed loop equilibrium, a step command is given to change the desired forward speed from $0 \rightarrow 2 \text{ m/s}$. Just after the command is given and before the forward speed rises significantly, the motion can be considered to be governed by a simplified form of Equation (2.10) with $\mathbf{v} = \mathbf{v}_w = \boldsymbol{\omega} = \dot{\boldsymbol{\omega}} = 0$. In this case the x -component of this equation can be reduced to:

$$m_{11} = \frac{\sum_{i=1}^4 T_{i,x}}{\dot{u}} - m \quad (4.9)$$

where $\sum_{i=1}^4 T_{i,x}$ is the sum of the commanded thruster forces from all four thrusters in the x -direction, \dot{u} is the forward acceleration and m is the total inertial mass of the airship (including the helium and all other attachments). A similar technique was used in [45], to

experimentally determine the added mass of a submarine by towing it underwater, under constant acceleration.

It was found impractical to achieve a step input in forward thrust under open-loop control due to the resulting unstable motion caused by the Munk moment. Rather, we conducted this test in closed-loop control. However, the PID low-level controller discussed in the current thesis was not used. Rather, a Non-Linear Back-Stepping (NLBS) controller developed in Liesk [46] was used. The NLBS controller responds to step changes in desired forward velocity, by commanding a constant net thrust in the forward direction, thereby producing a constant forward acceleration; which is desirable for the current test. By contrast, the PID controller responds gradually by increasing/decreasing the commanded thrust levels until the desired velocity is attained (as in Figure 4-38), and this response is too slow in the context of the present experiment. For the sake of brevity, the NLBS controller is not discussed here but the reader is referred to [46] for details.

The added mass can be calculated using Equation (4.9), only just after forward thrusts are commanded. Once the velocity increases, the resulting drag would render Equation (4.9) invalid. Including the axial drag explicitly in Equation (4.9) could improve the results for the calculation of the added mass as was done in [45]. However, since our current axial drag model is of questionable accuracy (See Section 4.2.4), its use was avoided in the present experiment.

An issue of concern, then, is the selection of a good time-range over which we may analyse the variables in Equation (4.9). Since we will be using an averaging technique to estimate the added mass in this section, it is useful to know the minimum time over

which an averaging must be done, so as to minimize the effect of high frequency noise that may deteriorate the results. Using an FFT on the recorded signals, the highest frequency noise was identified at 12.5 Hz in the IMU acceleration data. To minimize the error introduced by this noise, we wish to average a minimum of 10 periods of this noise i.e. the averaging will be carried out over a minimum of 0.8 s.

To identify a good start time for the analysis, we note that once the thrusts are commanded, the thruster dynamics (modeled as a first order system, See Appendix A) introduce delays before the actual thrust of the thrusters can match the commanded thrusts. For the range of thrusts commanded in this test, the time constant of this first-order thruster model for a step input was determined to be $\tau \approx 0.4 \text{ s}$ [8]. Therefore, for each test case, from the point the thrusts first seem to rise (denoted as t_1) we will wait at least 3τ , yielding the minimum start time of the analysis to be $t_1 + 3\tau$.

Finally, it was also noticed that there exists a certain delay between the time the thrusts are first commanded to cause a change in forward velocity and when the IMU data shows a corresponding increase in accelerations. This may be due to transport delays in the communication system or due to delays in the thruster response. By comparing the recorded signals of commanded thrusts and accelerations, this delay was estimated to be about 0.2 s.

Taking the above criteria into account, we now show how Equation (4.9) was used in estimating the longitudinal added mass. As an example, for test case 1, Figure 4-33 shows the commanded thrusts in x -direction $\sum_{i=1}^4 T_{i,x}$ and the corresponding forward acceleration \dot{u} , to effect a change in the forward velocity u (not shown) of the airship.

The time at which the thrust begins to rise, t_1 , is shown as a vertical solid line. The thrusts remain sufficiently constant between the time interval $113.7 \rightarrow 114.5$ s (vertical dashed lines in Figure 4-33). Taking the 0.2 s delay into account, the forward acceleration is averaged over the time interval $113.9 \rightarrow 114.7$ s (vertical dash-dotted lines in Figure 4-33).

A total of four tests were carried out. The value of $m = 6.102$ kg was used for test cases 1, 2 and 3 since they were conducted on 12th April, 2012 while test case 4 was conducted on 15th April, 2012, and so $m = 6.090$ kg was used. Table 4-7 summarizes the results for the four tests (see Appendix G for plots of all four test cases).

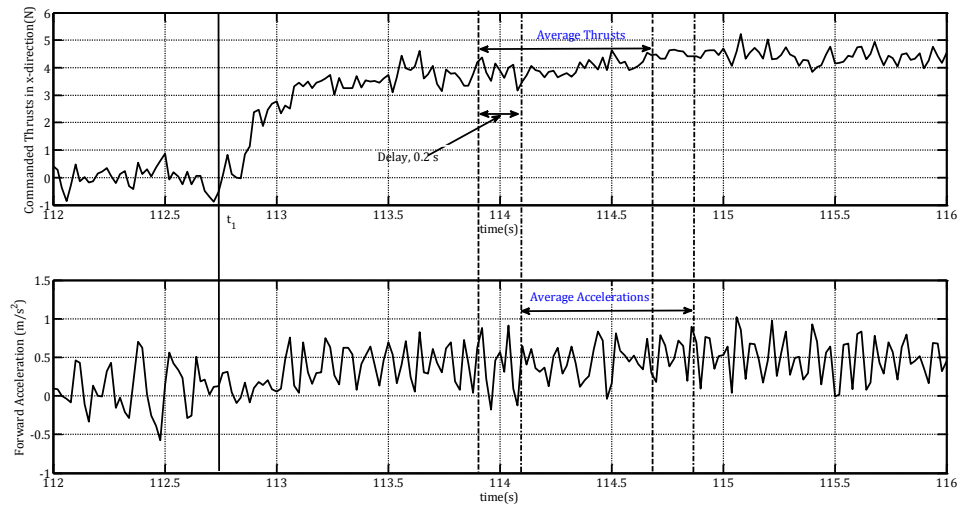


Figure 4-33: Commanded thrusts in x-direction (top) and forward acceleration (bottom) – Forward acceleration test : Test case 1

Table 4-7: Summary of results for estimating longitudinal added mass

Test Case	t_1 (s)	Thrusts, Averaging time, (s)	$\sum_{i=1}^4 T_{i,x}$ (N)	Forward acceleration Averaging time, (s)	\dot{u} , (m/s^2)	m_{11} , (kg)
1	112.7	113.9 → 114.7	3.762	114.1 → 114.9	0.398	3.350
2	180.4	181.6 → 182.4	4.286	181.8 → 182.6	0.638	0.616
3	283.3	284.5 → 285.3	4.068	284.7 → 285.5	0.542	1.403
4	25.6	26.8 → 28.0	4.746	27.0 → 28.2	0.688	0.807

The estimated value of m_{11} was 0.646 kg as discussed in Section 2.5.2. Table 4-7 shows that the added mass experimental estimate lies between $0.616 - 3.350 \text{ kg}$. The fact that $m_{11} > 0$ for every test indicates that there does exist a virtual mass for the airship during accelerations, but there is a large variation in the estimated added mass. One of the reasons for this discrepancy is the variation in the averaged values of both $\sum_{i=1}^4 T_{i,x}$ and \dot{u} over the course of four tests. Equation (4.9) is highly sensitive to variations in values of both these variables. As an example, for a fixed $\sum_{i=1}^4 T_{i,x}$, if \dot{u} was recorded with a 25 % error (say 0.4 m/s^2 instead of 0.5 m/s^2) the propagated error in the calculation of m_{11} would be as high as 50%. Thus, the test conducted does illustrate the presence of a longitudinal added mass, but it cannot accurately predict its magnitude.

4.2.6.2 Lateral Added Mass

In this test, the airship is first commanded to hover at a desired height at the start of the experiment. Once in closed loop equilibrium, all four thrusters are simultaneously switched off ($\mathbf{f}_T = \mathbf{n}_T = 0$). Just after the command is given, the motion can be considered to be governed by a simplified form of Equation (2.10) with $\mathbf{v}_w = \boldsymbol{\omega} = \dot{\boldsymbol{\omega}} = 0$. In this case the z -component of this equation can be reduced to:

$$m_{22} = \frac{h_a g - D_N}{\dot{w}} - m \quad (4.10)$$

where h_a is the heaviness of the airship, g is the acceleration due to gravity, D_N is the normal drag, \dot{w} is the downwards acceleration and m is the total inertial mass of the airship. Note that in Equation (4.10), we are using the drag for our calculations since the drag coefficient C_d was experimentally validated in Section 4.2.3 against empirical predictions. For a pure vertical motion along the z -axis,

$$D_N = \frac{1}{2} \rho w^2 A_p C_d \quad (4.11)$$

As in the case of the estimation of the longitudinal added mass (Section 4.2.6.1), we select a time-range over which we will analyse the variables in Equation (4.10). To select the minimum period over which to average the variables in this equation, we identify the highest frequency noise, using an FFT, at 12.5 Hz in the IMU acceleration data. Thus, we will average a minimum of 10 periods of this noise i.e. 0.8 s.

To identify an appropriate start time for the analysis, we note that once the thrusts are switched off (denoted as t_2) it takes about 3τ ($\tau \approx 0.4$ s) for 95 % of the actual thrusts to die out, where τ is the time constant of the thrusters for a step input of magnitude ≈ 1.5 N. It was also observed that the data for \dot{w} contained undesirable spikes until 4τ , and so the analysis will begin at $t_2 + 4\tau$.

We now show how Equation (4.10) was used in estimating the lateral added mass. As an example, for test case 1, Figure 4-34 (top) shows the commanded thrusts in the z-direction switched off at $t_2 = 117.3$ s and the consequent increase in drag represented by a decreasing $h_a g - D_N$. The corresponding vertical acceleration \dot{w} is also shown (Figure 4-34 (bottom)). We start averaging $h_a g - D_N$ and \dot{w} , from $t_2 + 4\tau$ for a period of 0.8 s. Thus the averaging is done between $t = 118.9 \rightarrow 119.7$ s.

A total of three tests were conducted for this experiment on the 12th April, 2012, the same day as the normal drag test was conducted (Section 4.2.3). Thus, $m = 6.102$ kg and $h_a = 0.684$ kg. Recall that for Equation (4.10) to be valid, we must ensure that $\omega \approx 0$. It was observed that, for test case 2, the airship was not sufficiently stabilized in the hover before the thruster were switched off, and so, the strong angular motions occurring at the

beginning of the fall rendered the data from this test unusable. These results are therefore not presented. Table 4-8 summarizes the results for the two valid test cases.

Table 4-8: Summary of results for estimating lateral added mass

Test Case	t_2 (s)	Averaging time, (s)	$h_a g - D_N$, (N)	\dot{w} , (m/s^2)	m_{22} , (kg)
1	117.3	118.9 → 119.7	6.19	0.632	3.690
3	86.1	87.7 → 88.5	6.02	0.612	3.740

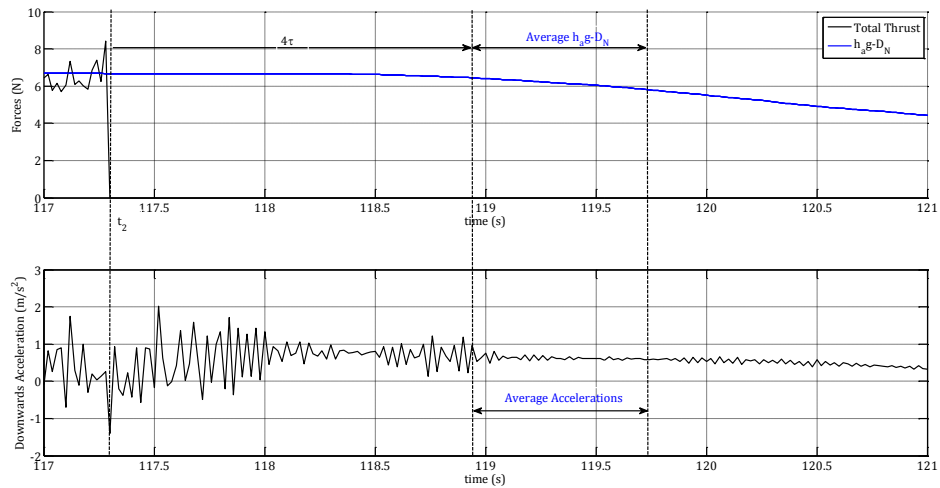


Figure 4-34: Commanded thrusts in z-direction and $h_a g - D_N$ (top), and vertical acceleration (bottom) – Lateral added mass test : test case 1

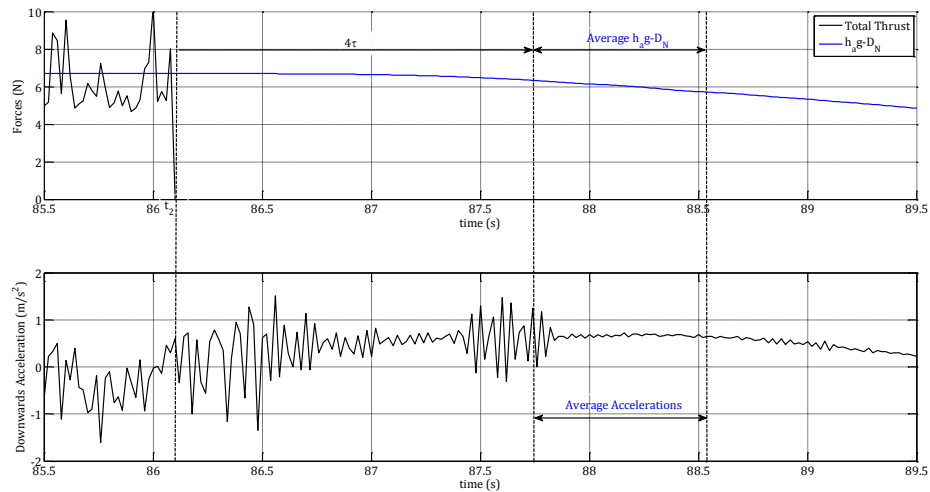


Figure 4-35: Commanded thrusts in z-direction and $h_a g - D_N$ (top), and vertical acceleration (bottom) – Lateral added mass test : test case 3

The empirically estimated value of m_{22} was 4.672 kg . The results for the two test cases from the experiments are quite consistent such that the average m_{22} from the two tests is $\approx 3.715 \text{ kg}$; a value 20 % lower than the empirical estimate. It is noted that in [8], m_{22} was estimated based on the added mass of an equivalent ellipsoid as in Fossen [47]. Thus it is likely that for the airship, which is more tapered at the ends, the amount of ambient fluid accelerated during the airship's accelerations will be less, and so the overall added mass will be reduced.

4.2.7 Experimental Validation of Thruster Reaction Torques

It was noted in Section 2.3.4 that the thruster reaction torques can be significant for the airship, since all four thrusters spin in the same direction i.e. CCW viewed from above. Therefore, it is expected that in a stationary hover, when a certain constant thrust is commanded to each of the thrusters, a net moment will act on the airship tending to yaw the airship clock-wise (the direction opposite the rotating thruster rotation). To test this hypothesis, a field test was carried out with the actual vehicle. The airship is commanded to hover at a height of 5 m using the PID controller. A real-time averaging algorithm averages the thruster command inputs over 20 s , in this condition. Once the airship is stable in the hover, the PID controller is turned off, the average command thrusts in the z-direction are commanded and held at those values and all four servo angles are held at the 0° position. This test was carried out twice and the results for the yaw-rates and the commanded thrusts in the z-direction for the two tests are shown in Figure 4-36. The figure also shows the simulated yaw-rates for two simulations: a) one with the empirically predicted value of the rotational damping coefficient $k_\omega = 4.42 \text{ Nm} / \left(\frac{\text{rad}}{\text{s}}\right)^2$

and b) one with the experimentally estimated value of the rotational damping coefficient

$$k_{\omega} = 2 \text{ Nm} / \left(\frac{\text{rad}}{\text{s}} \right)^2 \text{ (See Section 2.2.1).}$$

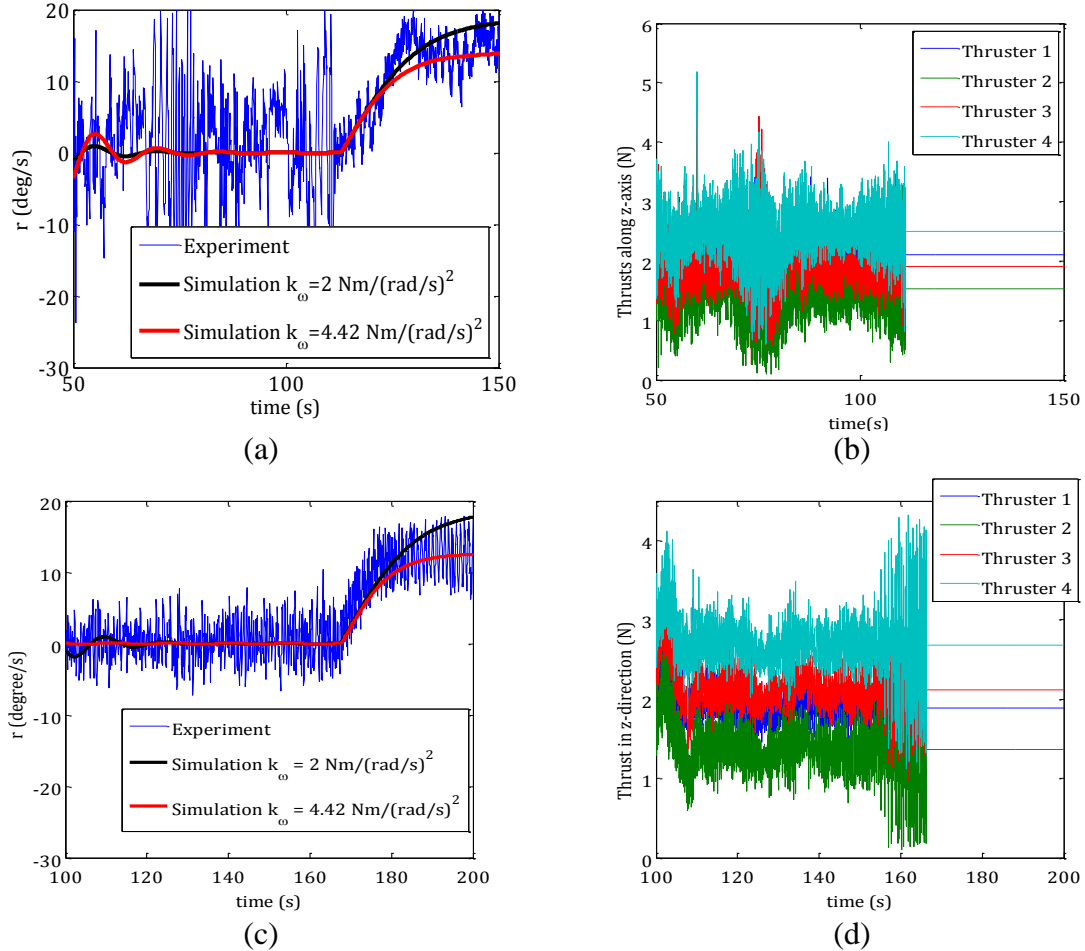


Figure 4-36: Experimental yaw-rates (a) and (c) and corresponding commanded thrust in z-direction profiles (c) and (d).

From the experimental results, it was also observed that the height (not shown) was maintained to within $\pm 0.5 \text{ m}$ for each test, both before and after the thrusters were frozen. In Figure 4-36 (a) and (c), once the average thrusts are commanded in the z-direction, and the airship is no longer under closed-loop control, it starts to yaw clockwise, as predicted. Due to the rotational damping moments discussed in Section 2.2.1, the yaw-rate seems to converge terminally to $\approx 14 \text{ deg/s}$ in the first case, while clearer convergence is observed in the second test case to about $\approx 12 \text{ deg/s}$. Both cases

clearly indicate the presence of the reaction torques. When comparing the simulation results to the experimental ones, it appears that the empirically-estimated damping coefficient of $k_\omega = 4.42 \text{ Nm} / \left(\frac{\text{rad}}{\text{s}}\right)^2$ yields a better match. This may imply that, under certain conditions, that estimated value is accurate. However, it could alternatively imply that the reaction torque is overestimated in the simulation relative to the experiment. More detailed tests and simulations would need to be performed, including the thruster effect on the airflow, before drawing firm conclusions.

4.2.8 Munk Moment Validation

The term $-(\mathbf{v} - \mathbf{v}_w) \times \mathbf{M}_{D_a}(\mathbf{v} - \mathbf{v}_w)$ in Equation (2.10) represents the destabilizing Munk moment acting on the airship. It is a function of the airspeed of the vehicle $(\mathbf{v} - \mathbf{v}_w)$ and the apparent displaced mass matrix \mathbf{M}_{D_a} . If $\mathbf{v}_w = 0$, which is presumably the case inside the dome test-facility, we can rewrite the Munk moment \mathbf{M}_{munk} in the body-frame as:

$$\mathbf{M}_{munk} = (m_{22} - m_{11}) \begin{bmatrix} 0 \\ uw \\ -uv \end{bmatrix} \quad (4.12)$$

where, m_{22} and m_{11} are the added masses in the lateral and longitudinal directions respectively.

In this test, the airship is commanded to fly forward at a constant desired speed. An online-averaging algorithm averages the commanded thrust for each thruster over the last 10 s continuously. Once the airship has reached a steady-state forward velocity, the last averaged thrust value up to this point is used to calculate the magnitude and servo-tilt for each thruster, and the thrusters are now frozen at these values. The frozen values are then commanded until the end of the experiment and the airship operates in open-loop. The

consequent behavior of the airship, which is expected to go unstable, is recorded. The Munk moment is calculated using the measured flight data during post-flight analysis using Equation (4.12).

This test was carried out for desired forward speeds of 1 m/s , 2 m/s and 3 m/s . Given the limited field size, the airship was not able to reach steady-state velocities of 2 m/s and 3 m/s , before the end of the test space. The results presented are, thus, only for the first case, with the desired forward speed of 1 m/s .

The tests are compared to a simulation that was conducted offline. In the simulation, similar to the experiment, we first make the airship hover, command a forward velocity of 1 m/s , and once this velocity is stable, the last averaged thrust value from the thruster model up to this point over the last 10 s is commanded and the thrusters are now frozen at these values. The simulation and experimental results are presented in Figures 4-37 to 4-44.

As seen, the airship is commanded a desired forward velocity at $t = 43\text{ s}$ (Figure 4-37) and the thrusters are locked to the average values at $t = 66\text{ s}$ (Figure 4-38). The vertical dashed line in each figure represents the instant the forward velocity is commanded while the dotted line represents the instant at which the thrusters were frozen. The experimental Munk moment is now calculated using Equation (4.12) and is shown in Figure 4-40 and 4-42.

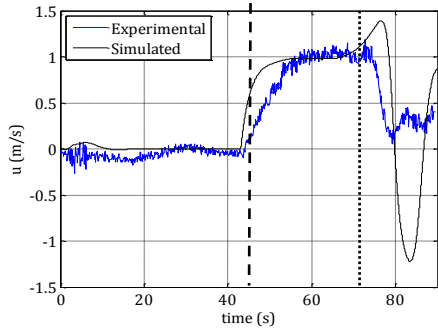


Figure 4-37: Munk moment test 1, u

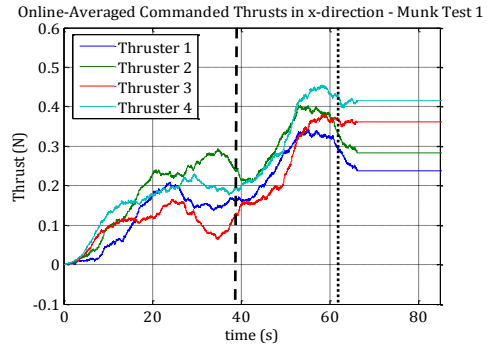


Figure 4-38: Munk moment test 1, average thrust

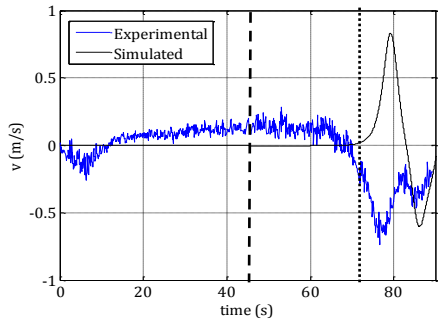


Figure 4-39: Munk moment test 1, v

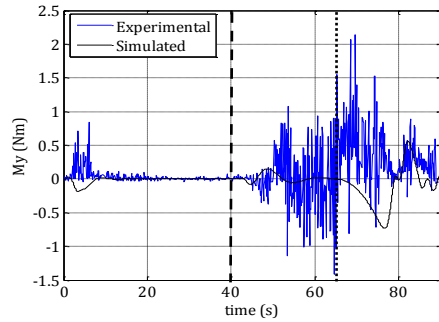


Figure 4-40: Munk moment test 1, Munk moment in y

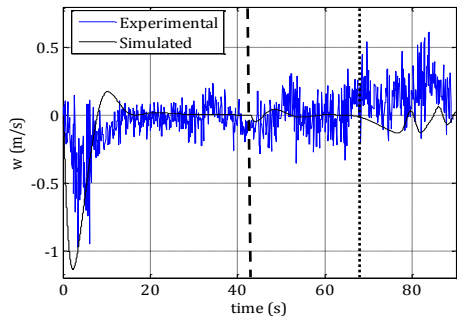


Figure 4-41: Munk moment test 1, w

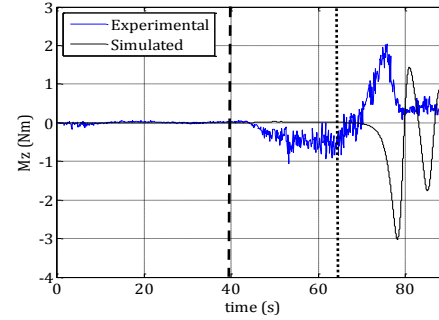


Figure 4-42: Munk moment test 1, Munk moment in z

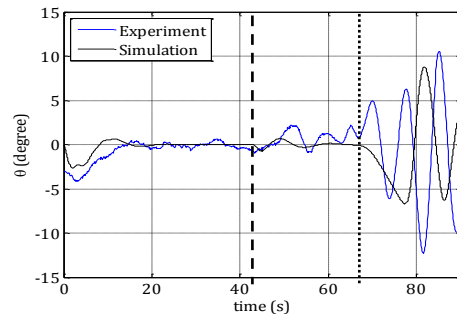


Figure 4-43: Munk moment test 1, pitch

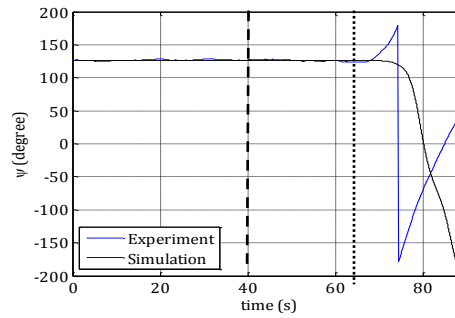


Figure 4-44: Munk moment test 1, yaw

As is seen from the above figures, once the thrusters are frozen, the airship quickly incurs large Munk moments in both the y and z directions. This causes strong unstable pitching and yawing motions in the airship.

The subsequent motions of the airship are quite different between the experiment and the simulation once the airship thrusters are frozen. A possible explanation could be the difference between initial states of the experimental and simulated airship response as it enters the open-loop mode. Different initial conditions can produce significantly different behaviours in the airship motion in open-loop. This will now be investigated by slightly changing the initial states of the simulated airship to be consistent with the experiment.

The difference between the experiment and the simulation is especially apparent in the sideways velocity v (Figure 4-39). The airship experiences a slightly v ($44\text{ s} < t < 66\text{ s}$) of about 0.1 m/s . A possible cause for this could have been an IMU misalignment in roll since if the airship is in a non-zero roll position, there will a component of the thruster forces that would induce some side velocity. Similarly, a misalignment in pitch would have resulted in offsets for u and w . However, these DOF's are controlled and their offsets are regulated by the controller. The most likely reason for the IMU misalignment is that the IMU is attached to the airship with a Velcro patch, and it is quite possible that its orientation suffers slight offsets. This is further validated by the fact that, in Figure 4-38, the average thrust produced by each thruster is different (under perfect IMU alignment, with a center of gravity that is slightly aft CoB the thrusters would command the same values for thrusters 1 and 4, and for thrusters 2 and 3). Using moment relations about the CoB for the thrusts, it was found that the thrusters were in fact compensating for pitch and roll misalignments. For the sake of brevity though, we will not detail these results.

Through trial and error it was found that, when this simulation was carried out with a desired roll setpoint $\phi_d = +1^\circ$ (Figure 4-50) and a desired pitch setpoint $\theta_d = +4^\circ$

(Figure 4-51), a similar behaviour was noted in v (Figure 4-47) and the consequent motions of the airship once the thrusters were frozen.

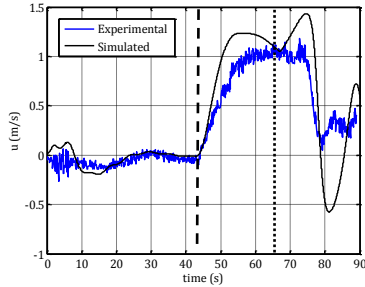


Figure 4-45: Munk moment test 2, u

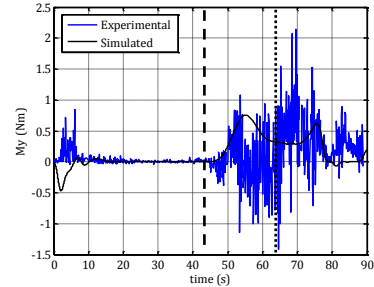


Figure 4-46: Munk moment test 2, Munk moment in y .

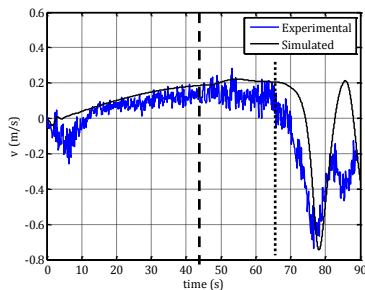


Figure 4-47: Munk moment test 2, v

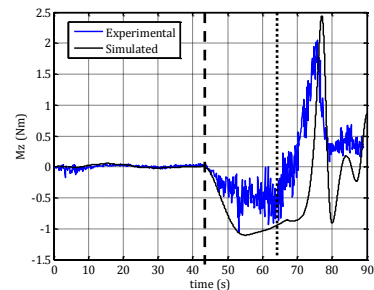


Figure 4-48: Munk moment test 2, Munk moment in z .

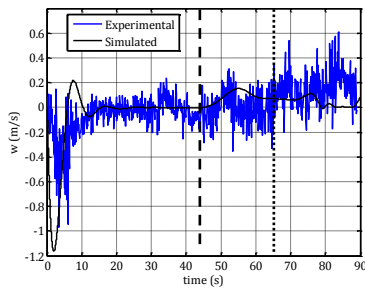


Figure 4-49: Munk moment test 2, w

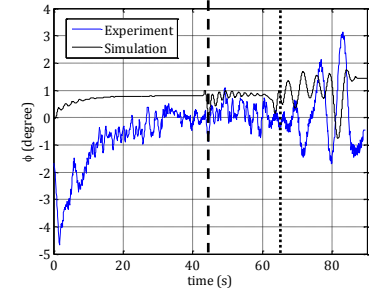


Figure 4-50: Munk moment test 2, roll

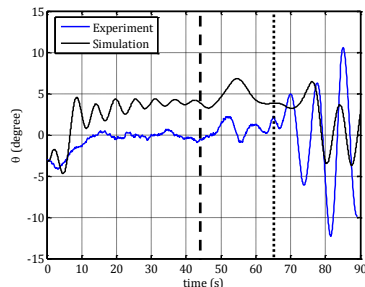


Figure 4-51: Munk moment test 2, pitch

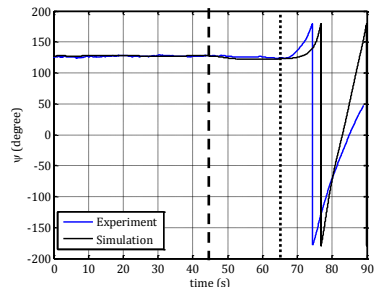


Figure 4-52: Munk moment test 2, yaw

As can be seen by comparing the two sets of results from each simulation, the state of the airship, right before the thrusters are frozen significantly impacts the airship motion. With

the new initial conditions, once the thrusters are frozen, the forward velocity drops (Figure 4-45), while the side wards velocity (Figure 4-47) changes direction and peaks negatively. The Munk moments in the y and z -directions (Figures 4-46 and 4-48), and the corresponding pitch and yaw responses (Figures 4-51 and 4-52) also show good correspondence to the experiment. This experiment thus validates the presence and impact of the Munk moment in destabilizing the airship in open-loop conditions.

It is also worth noting that a slight misalignment in the IMU can produce differences in the results, due to the significant moments and forces that act on the airship as a result. For closed loop flights this might not have a great impact on the performance, but substantial control effort might be wasted as a result of the airship flying misaligned with the relative wind. As such it is suggested that the IMU be fixed on the airship more stably, and a method for proper calibration be designed for repeatability of the tests.

4.3 Closed-Loop Controller Suite Validation

This section details the experimental results for the validation of the low-level controller (LLC) and the high-level controller (HLC), which were discussed in Chapter 3. The LLC is a PID controller, while the HLC is a guidance algorithm to guide the airship along a set of desired waylines. The SGPS configuration for localization and velocity measurements was used in this test. Furthermore, both the SGPS and sonar measurements were used to determine the inertial height, as previously discussed in Section 4.1.4.3. The validation tests were carried out at the Rutherford Park in Montreal. A satellite image of the park is shown in Figure 4-53. The figure also indicates the test field over which the airship was flown and the location of the wind sensor, a height of $\approx 7\text{ m}$ above ground. As

mentioned in Section 4.1.4.4, the wind sensor is used only to record the average wind conditions over the field to be used with post-flight analysis, and does not provide the wind conditions at the airship's location. The wind conditions at this outdoor field vary considerably with time, with intermittent gusts and changing average wind speeds and directions; conditions well suited to test the controller performance in the presence of wind disturbances.

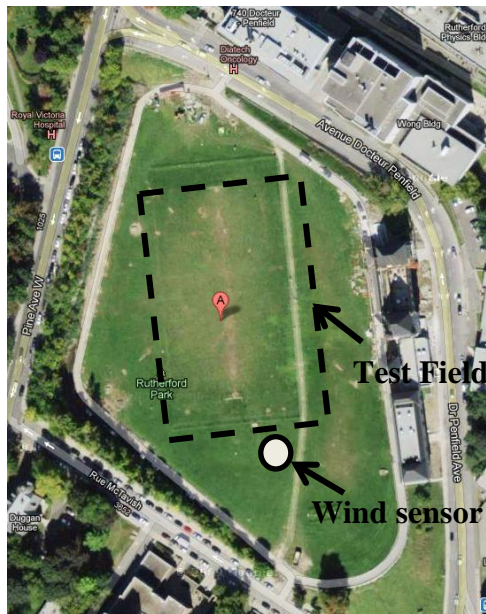


Figure 4-53: Satellite image of Rutherford Park[48]

4.3.1 Low-Level Controller Validation

For the validation of the PID-LLC, the airship was commanded to proceed around the field using a joystick connected to the ground station that would feed the desired setpoints to the QUARC microprocessor. The joystick provides setpoints for desired forward velocity u_d , desired yaw ψ_d and desired height h_d . The desired roll ϕ_d and desired pitch θ_d are held at 0° .

For take-off, two assistants hold the airship lightly, one at the nose and other at the tail. The thrusters are idled first, and then a command is sent to engage the PID controller. All commands are sent from the ground station over the WiFi network to the QUARC microprocessor. The controller is tested by changing velocity, height and yaw set-points. The airship is first commanded to hover at a height of 4 m from ground for the first 25 seconds. A non-zero u_d is then commanded at $t = 25$ s to fly the airship due North-East. During this forward flight, we increase and decrease u_d to test the airship's ability to accelerate and decelerate. At about $t = 90$ s, a near-zero u_d is commanded and the airship is made to turn by changing the desired yaw-heading ψ_d , to fly the airship due South-East. In a similar fashion, by controlling the u_d and ψ_d the airship is flown over the field as seen in Figure 4-54. Towards the end-of-flight, a change in height is commanded, first to increase the height, and then to decrease it between $t = 200$ s and 235 s as seen in Figure 4-59. The complete set of results for all controlled states is shown in Figure 4-54 to 4-59. The PID controller shows good tracking capabilities. The height remains within ± 1 m of desired height and the pitch and roll angles remain within a few degrees of their desired zero values, even during setpoint changes to yaw and forward velocity. The forward velocity and yaw are also tracked very well and the controller reacts well to changes in desired forward velocity and desired yaw. The initial offsets in pitch and roll are quickly regulated by the controller.

For comparison, the desired setpoints for the five controlled states recorded during the flight were fed into the simulation model with the low-level controller active. The resulting simulated airship motion is also shown in Figure 4-54 to 4-59. There is excellent correspondence between the experiment and the simulation, implying good

fidelity of the closed-loop simulation model. However, these results do not necessarily imply accuracy of the airship's open-loop dynamics model.

The difference between the end-points of the airship position in the NE frame is quite significant between the experiment and the simulation, despite the general trajectory being similar. This is likely due to differing wind conditions in the simulation and the experiment. The simulation model assumes zero wind conditions, while the actual experiment outdoors included significant wind (Figure 4-60 and 4-61). We also note peaks in the simulation at certain points for the roll and pitch profiles (e.g. at $t = 90$ s for pitch and $t = 120$ s for roll) at instant where the yaw setpoint is changed. These were investigated and it was found that a slight reduction in the proportional gains for the pitch and roll controllers will suppress these peaks.

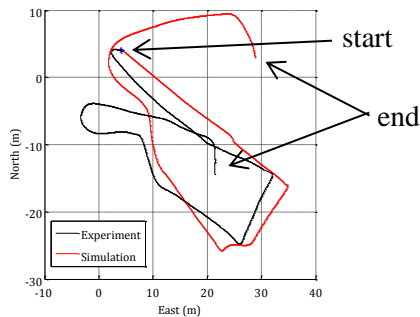


Figure 4-54: PID validation, NE trajectory

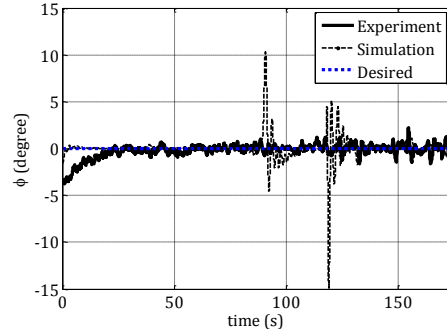


Figure 4-55: PID validation, roll angle

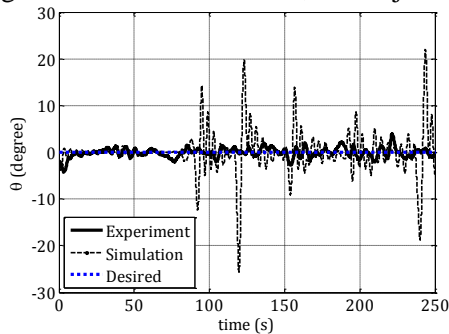


Figure 4-56: PID validation, pitch angle

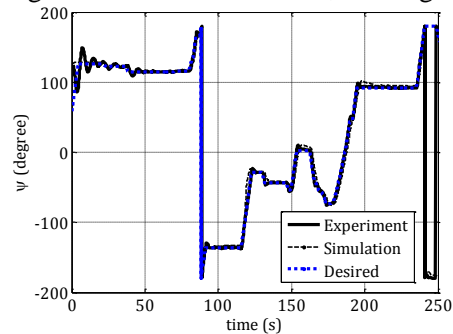


Figure 4-57: PID validation, yaw angle

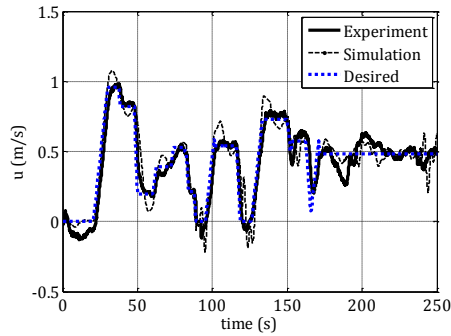


Figure 4-58: PID validation, forward velocity

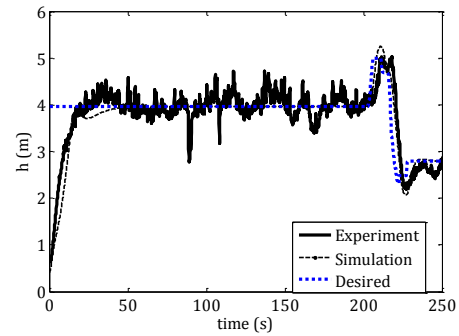


Figure 4-59: PID validation, height

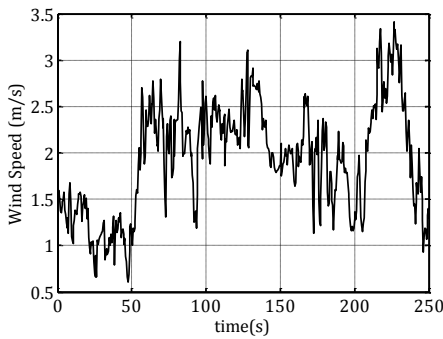


Figure 4-60: PID validation, wind speed

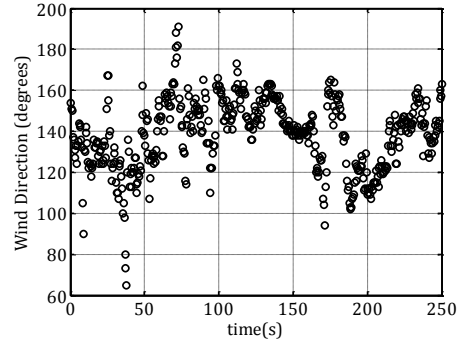


Figure 4-61: PID validation, wind direction

4.3.2 Complete Controller Suite Validation

Having validated the experimental implementation of the low-level controller, we now move on to test the complete controller suite, which includes the PID low-level controller and the proposed guidance algorithm discussed in Section 3.3.2 as the HLC. Figure 3-1 shows the schematic of this setup. The wind data from the wind sensor is also presented. It is emphasized that the wind information only gives us an approximation of the wind conditions over the test-field, and not the specific wind information at the location of the airship, which may be quite different owing to local wind gusts. Also, recall that the HLC does not use this wind information to guide the airship along the path. Rather, these measurements were collected for post-flight analysis only.

The gains and rate-limits used in the guidance algorithm are given in Table 4-9. Note that these are the same values as were used in the simulations in Section 3.3.2.5.

Table 4-9: Gains used in guidance experiment

K_{P_χ}	K_{P_η}	K_{P_h}	$\tilde{\chi}_{max}$	a	$\tilde{\eta}_{max}$	b	$\dot{\psi}_{d,max}$	$\dot{\theta}_{d,max}$
$0.1 s^{-1}$	$0.1 s^{-1}$	$0.2 s^{-1}$	45°	$1.2 m^{-1}$	20°	$0.8 m^{-1}$	$\pm 15^\circ/s$	$\pm 5^\circ/s$

The airship is made to traverse the following waypoints listed in Table 4-10, with the GPS base antenna being the origin of the coordinate system. The height of the desired waylines is kept fixed in this test.

Table 4-10: Waypoint list for guidance experiment

	N	E	D
Waypoint 1	-20	-20	-4
Waypoint 2	20	-20	-4
Waypoint 3	20	20	-4
Waypoint 4	-20	20	-4
Waypoint 5	-20	-20	-4

The airship is first sent the idle command, which idles the thrusters. The LLC-PID is then engaged to make the airship reach a desired height of 4 m. Once noticeably stable, the HLC is engaged and the airship operates in fully autonomous mode. The airship turns into the next wayline once it is within 4 meters from the current targeted waypoint. Results for the airship's trajectory and the corresponding states during flight are shown in Figure 4-62 to 4-67.

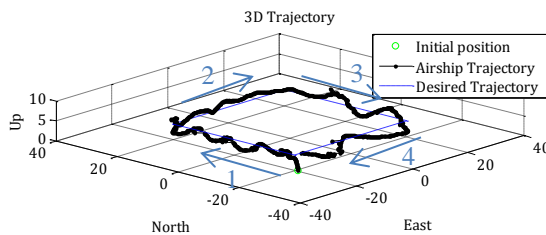


Figure 4-62: HLC validation, 3D trajectory

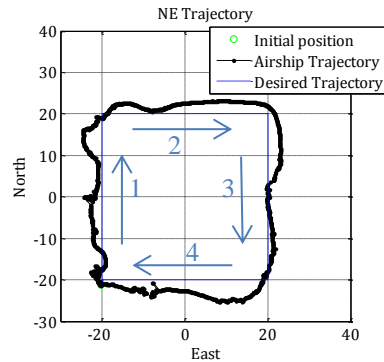


Figure 4-63: HLC validation, NE trajectory

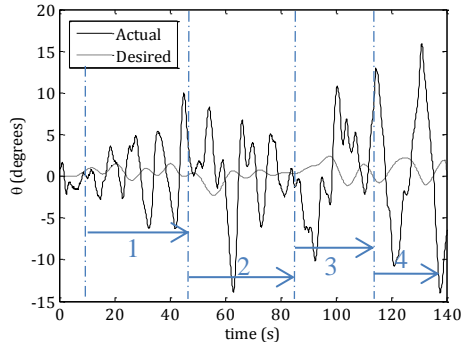


Figure 4-64: HLC validation, pitch angle

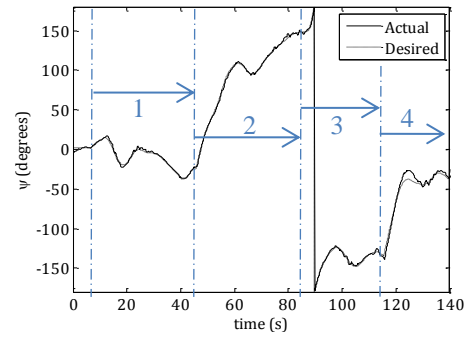


Figure 4-65: HLC validation, yaw angle

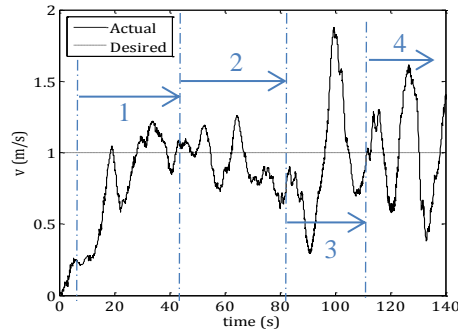


Figure 4-66: HLC validation, forward velocity

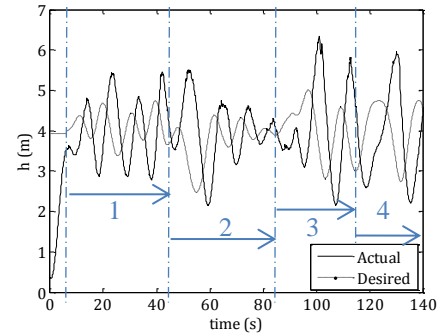


Figure 4-67: HLC validation, inertial height

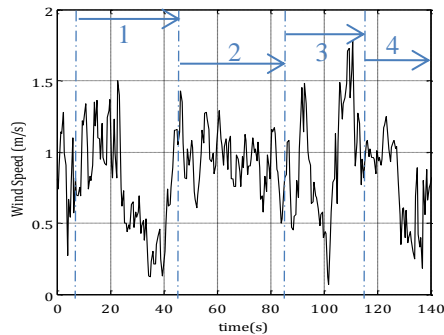


Figure 4-68: HLC validation, wind speed

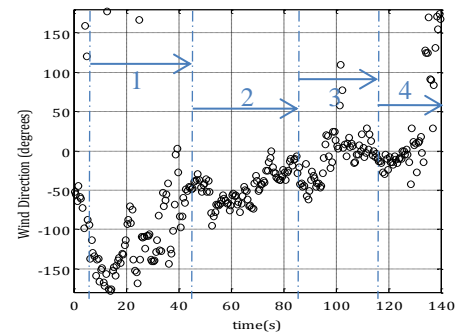


Figure 4-69: HLC validation, wind direction

The airship manages to autonomously fly through the mission waylines even in the presence of winds. Although during the course of this test the airship tried to orient its heading to counter the cross-wind component, there is not much correspondence between the airship's heading information (Figure 4-65) and the wind information gathered from the wind sensor (Figure 4-68 and Figure 4-69) for most of the flight. As mentioned previously, this is because the wind sensor is in a fixed position near the ground station and thus does not fully represent the wind information at the airship's location.

It is apparent from the results, that the airship does not align itself with wayline direction but slightly into the local wind, the direction of which may be judged from the airship heading. For example, from Figure 4-65, while intercepting wayline 3, the airship heading should have converged to -180° in the absence of wind. However, it converges to around -130° , which indicates a cross-wind component from the West. Similarly, for wayline 4 the airship heading should converge to -90° in the absence of wind but it converges to around -40° showing the presence of a component of the wind from the North. Thus, during wayline 3 and 4, a North-Westerly wind likely prevailed, which is close to the wind sensor information (Figure 4-69) which in fact shows an average North-Westerly wind direction between wayline 3 and 4. Figure 4-64 shows the pitch and profile. Figures 4-64, 4-66 and 4-67 show the pitch, forward speed and height profiles, respectively. Taken together, they show a clear oscillation with a period of about 10 s. This oscillation is initially excited by the sharp changes of heading at the waypoints and the LLC does not seem to be able to assertively damp this out; the oscillations continue through the entire flight. The pitch angle, forward speed and height appear to all be in phase. Note, however, that the *desired* height and pitch are changing negatively when the airship height and pitch are increasing, respectively, and vice versa. It appears that the tuning of the LLC controller gains could be improved in the longitudinal degrees of freedom. On the other hand, Figure 4-65 shows that the airship does an excellent job of tracking the desired heading generated by the HLC. In conclusion, the airship is able to complete the course, even under these relatively high wind conditions; as high as 1.75 m/s at one point during the test.

Chapter 5 Conclusions and Recommendations for Future Work

The underlying objectives of this work were three-fold. Firstly, improvements were made to the existing dynamics model of the airship. Next, a high-level guidance algorithm to autonomously maneuver the airship outdoors in windy conditions was developed. Finally, experimental evaluation of certain airship physical parameters and experimental evaluation of the controller suite for the airship were carried out.

5.1 Improvements to the Dynamics Model

Four improvements were made and added to the existing dynamics model: the rotational damping moments, the effect of protuberances on the axial drag, the gyroscopic moments due to the thruster and body rotations, and the thruster reaction torques.

Using a method based on pure rotation of the airship, the rotational damping moment coefficient was found to be $k_{\omega} = 4.42 \frac{Nm}{(rad/s)^2}$. Using a closed loop simulation, it was found that during quick angular maneuvers, the damping moment experienced by the airship was significant. Also, the total thruster effort required during angular decelerations was also reduced, since the damping moments aided the thruster in decelerating the airship.

The modified axial drag coefficient due to protuberances was empirically obtained and it was found that due to the presence of the gondola, the airship's axial drag coefficient increased by about 30 %, while the GPS antenna and the thruster legs had minimal

impact. This result corresponded closely to data available for other airships of similar fineness ratios.

By making a few simplifying assumptions, the gyroscopic moments due to servo and body rotations could be derived as a single equation and, besides these rotations, depended only on the moment of inertia of the spinning assembly about the spin-axis. Even though the spinning velocity was high during operation, in closed-loop flight, the moments had no significant impact on the performance of the airship, since the combined servo and body rotations, and the inertia of the rotating assembly was small.

Finally, it was shown that the reaction torques could be estimated if a reliable thrust model was available. This model accurately estimated, both, the transient and steady-state characteristics of the reaction torques. A closed-loop simulation showed that the reaction torques only had a small impact on the performance and stability of the airship.

5.2 The Airship Controller Suite Design

The simulation gains for the PID controller from [8] were re-tuned for better performance in winds. Simulation results with the new gains showed an improved tracking, especially with respect to the forward velocity and height trajectories than in [8].

A guidance algorithm that had previously been tested on another underwater vehicle was then implemented on the Mk-II ALTAV. The performance of the airship with this guidance method was poor under windy conditions. An advanced dynamics-based algorithm for 3-dimensional guidance was therefore developed and implemented. In simulations, it showed superior performance in the presence of no winds and reduced overshoots at the turns. The vehicle was also simulated under wind conditions

comparable to the vehicle airspeed, yet the airship managed to traverse the prescribed path successfully with minimal overshoot or cross-track error. This was achieved by the airship slightly orienting itself into the cross-wind component. The airship also reduced the drag force on its hull in this manner, facilitating its convergence onto the desired path.

5.3 Validation and Flight Testing

Flight tests were carried out to validate certain airship parameters. Very good agreement was obtained for the heaviness of the airship and the horizontal position of the center of gravity. This also validated the steady-state thruster model on the airship.

The experimentally determined axial drag coefficient, the rotational damping coefficient and the longitudinal added mass coefficient did not show good agreement with the empirically predicted values. In particular, tests conducted with the thrusters switched off yielded results close to empirical predictions (Normal Drag test, Lateral Added Mass test) while tests conducted with the thrusters operating (the Axial Drag test, Rotational Damping Estimation test and the Longitudinal Added Mass test) led to results that did not match empirical predictions. It was concluded that the thrusters' effects must be taken into account, since they seem to strongly affect the airflow around the airship, and by extension, the airship parameters. The reaction torques were also validated and the airship was shown to yaw clockwise, viewed from above, in an open-loop hover flight with all four servos held at 0° .

During the Munk moment test, it was noted that the initial conditions, right before the airship switches to open-loop operation, strongly affect its subsequent behaviour.

Furthermore, it was shown how small offset in the IMU calibration (1° in the roll and 4° in the pitch) can lead to significant changes in the ensuing motion.

The low-level (PID) controller was then tested in the Rutherford Park at McGill University and showed very good performance. The airship tracked reference trajectories quite well with respect to all five controlled states. Finally, the complete controller suite, including the low and high-level (guidance) controllers, was tested and showed the airship's ability to track the desired waylines under wind conditions comparable to its own velocity.

5.4 Future Work

The following recommendations are made for future work on the Mk-II ALTAV

- The effect of the thrusters on the airflow around the airship appears to significantly affect key airship parameters, and should be modeled. The thruster prop-wash could be modeled, possibly using empirical or CFD methods, since it accelerates the air over hull causing additional net drag. The change of the direction of the propwash due to the tilting of the thrusters should also be taken into account.
- Given that the results of Chapter 4 indicate a strong influence of IMU misalignment, a method to ensure correct IMU alignment, especially relative to the thrusters' alignment, should be developed. This could be done by developing a light-weight frame for the airship to which all sensors and thrusters would be attached.
- In most of the experiments performed, the thruster commands were found to be very noisy; likely due to sensor noise being fed back. Some form of filtering should be considered to reduce the 'hyperactivity' of the thrusters.

- The performance of the high-level controller might be improved if the algorithm were modified to also generate desired velocity as a guidance output. An example of this would be regulating the velocity to reduce cross-track errors at the turns.
- After the design of the LLC and the HLC, the next logical step would be the design of a path-planning algorithm. For true autonomous guidance, the vehicle must be able to also plan its own path, given the mission requirements. This will further reduce intervention on part of the human operator.
- The redundancy of the actuator system (as against the controlled states) has not been discussed in this thesis, though it is implicitly handled by the form of the LLC. Perhaps the LLC could be redesigned to consider actuator redundancy more explicitly, and thus make better use of this feature.

Bibliography

1. Ventry, A. M., Kolesnik, E. M., *Airship Saga: The History of Airships Seen Through the Eyes of the Men Who Designed, Built, and Flew Them*. 1982, Poole, Dorset: Blandford Press.
2. Dick, H. G., Robinson, D. H., *Golden Age of the Great Passenger Airships : Graf Zeppelin and Hindenburg*. 1992, Washington D.C.: Smithsonian Books. 226.
3. <http://www.pilotundluftschiff.de>. *Jean-Baptiste de la Place Meusnier Designs the First Airship (Mazhar, H. Trans.)*. [cited 2012 October 7]; Available from: <http://www.pilotundluftschiff.de/Meusnier.htm>.
4. www.airships.net. *Airships: The Hindenburg and other Zeppelins*. The Hindenburg Disaster | Facts, Theory, Photos [cited 2012 October 7]; Available from: <http://www.airships.net/hindenburg/disaster>.
5. Sofge, E. *4 New 'Blimp' Designs Bring Return of the Airship*. [cited 2012 October 7]; Available from: <http://www.popularmechanics.com/technology/aviation/airships/4242974>.
6. www.defenseindustrydaily.com. *Rise of the "Blimps": The US Army's LEMV*. [cited 2011 December 13]; Available from: <http://www.defenseindustrydaily.com/Rise-of-the-Blimps-The-US-Armys-LEMV-06438/>.
7. www.solarship.com. *A New Kind of Aircraft*. [cited 2012 September 10]; Available from: <http://solarship.com/video>.
8. Peddiraju, P., *Development and Validation of a Dynamics Model For an Unmanned Finless Airship*, in *Master's Thesis in Mechanical Engineering*. 2010, McGill University: Montreal.
9. Finck, R. D., Hoak, D. E., *USAF Stability and Control DATCOM*. 1978, McDonnell Douglas Corporation. p. 7.2.1-7.2.2.
10. Pierens, D. A., *Pitch and Roll Damping Coefficients of the Australian 81mm Improved Mortar Projectile*, A.a.M.R. Laboratory, Editor 1994, Department of Defense.
11. Wood, R. H., Murphy C. H., *Aerodynamic Derivatives for Both Steady and Non-Steady Motion of Slender Bodies*. 1955: Maryland.
12. Tobak, M., Reese, E., *Experimental Damping-in-Pitch of 45 degree Triangular Wings*, in *National Advisory Committee for Aeronautics*. 1950.
13. Batchelor, G. K., *An Introduction to Fluid Dynamics*. 99-101 ed1973, Cambridge: Cambridge University Press.

14. Georgiades, C., *Simulation and Control of an Underwater Hexapod Robot*, in *Master's Thesis in Mechanical Engineering*. 2005, McGill Univeristy: Montreal.
15. Hoerner, S. F., *Fluid Dynamic Drag*. 1958: Hoerner, S. F.
16. Abbott, I. H., *The Drag of Two Streamlined Bodies as Affected by Protuberances and Appendages*, NACA, Editor 1934.
17. Blevins R., D., *Applied Fluid Dynamics Handbook*. 1984, New York: Van Nostrand Reinhold Company.
18. Akins, R. E., Peterka, J. A., *Mean Force and Moment Coefficients for Buildings in Turbulent Boundary Layers*. *Journal of Industrial Aerodynamics*. 1977(2): p. 195-209.
19. Dorrington, G.E., *Drag of Spheroid-Cone Shaped Airship*. *Journal of Aircraft*. 2006. **43**(2).
20. Etkin, B., *Dynamics of Flight: Stability and Control*. 1959: John Wiley & Sons, Inc.
21. Bramwell, A., Done, G., Balmford, D., *Bramwell's Helicopter Dynamics*. 2001, MA: Butterworth-Heinemann.
22. Bouabdallah, S., Siegwart, R. *Full Control of a Quadrotor*. in *Proceedings of the 2007 IEEE/RSJ International Conference on Intelligent Robots and Systems*. 2007. San Diego, CA, USA: IEEE.
23. Bouabdallah, S., Noth, A., Siegwart, R., *PID vs LQ Control Techniques Applied to an Indoor Micro Quadrotor*, in *International Conference on Intelligent Robots and Systems (IROS)*. 2004: Sendai, Japan.
24. Amiri, N., Ramirez-Serrano, A., Davies, R., *Modelling of Opposed Lateral and Longitudinal Tilting Dual-Fan Unmanned Aerial Vehicle*, in *18th IFAC World Congress*. 2011: Milan, Italy.
25. Goel, R., Shah, S., Gupta, N., Ananthkrishnan, N. *Modeling, Simulation and Flight Testing of an Autonomous Quadrotor*. in *Proceedings of the IISc Centenary - Conference & Exhibition on Aerospace Engineering*. 2009. Bangalore.
26. Miller, M., Narkiewicz, J., *Tiltrotor Modeling for Simulation in Various Flight Conditions*. *Journal of theoretical and Applied Mechanics*. 2006. **44**(4): p. 881-906.
27. Papachristos, C., Alexis, K., Nikolakopoulos, G., Tzes A., *Model Predictive Attitude Control of an Unmanned Tilt-Rotor Aircraft*, in *IEEE International Symposium on Industrial Electronics (ISIE)*. 2011: Gdansk, Poland.
28. Gates, D. J., *Nonlinear Path Following Method*. *Journal of Guidance, Control, and Dynamics*. 2010. **33**(2): p. 321-332.

29. Raffo, G.V., Ortega M. G., Rubio F. R., *Backstepping/Nonlinear H_∞ Control for Path Tracking of a QuadRotor Unmanned Aerial Vehicle*, in *2008 American Control Conference*. 2008: Seattle, Washington, USA.
30. Johnson, E.N., Calise, A. J., *A Six Degree-of-Freedom Adaptive Flight Control Architecture for Trajectory Following*, in *AIAA Guidance, Navigation and Control Conference and Exhibit*. 2002: Monterey, California.
31. Azinheira, J.R., Moutinho, A., Paiva, E. C., *A Backstepping Controller for Path-Tracking of an Underactuated Autonomous Airship*. *International Journal of Robust and Nonlinear Control*. 2009 (19): p. 418-441.
32. Moutinho A., A., J. R., *A Gain-Scheduling Approach for Airship Path-Tracking*, in *Informatics in Control Automation and Robotics*. 2008, SpringerLink. p. 263-275.
33. Osborne, J., Rysdyk, R. *Waypoint Guidance for Small UAV's in Wind*. in *Proceedings of the AIAA Infotech@Aerospace Conference*. 2005.
34. Nelson, D.R., Barber, D. B., McLain T. W., Beard, R. W., *Vector Field Path Following for Miniature Air Vehicles*. *IEEE Transactions on Robotics*. 2007 **23**(3): p. 519-529.
35. Li, Y., *Dynamics Modeling and Simulation of Flexible Airships*, in *Ph.D Thesis in Mechanical Engineering* . 2007, McGill University: Montreal.
36. Battipede, M.M., Lando, M. and P. Gili. *Mathematical Modelling of an Innovative Unmanned Airship for its Control Law Design*. in *22nd IFIP TC 7 Conference on Systems Modeling and Optimization*. 2006. Turin, Italy.
37. Bedford A., F., W., *Engineering Mechanics - Dynamics*. 5th Edition 2007: Prentice Hall.
38. Carlton, J., S., *Marine Propellers and Propulsion*. 2007, Elsevier: MA. p. 89.
39. Evans, J., Nahon, M., *Dynamics Modeling and Performance Evaluation of an Autonomous Underwater Vehicle*. *Journal of Ocean Engineering*, 2004. **31**: p. 1835-1858.
40. Rysdyk, R., *UAV Path Following for Constant Line-of-Sight*, in *2nd AIAA "Unmanned Unlimited" Systems, Technologies and Operations. Aerospace, Land and Sea Conference*. 2003: San Diego, CA.
41. www.pjs.cz. *Technical Information (n.d)*. 2012 [cited 2012 2nd February]; Available from: <http://www.pjs.cz/produkty/informance/800-1000/index2.htm>.
42. ESRI. *Differential GPS Explained*. 2012 [cited 2012 October 12]; Available from: <http://www.esri.com/news/arcuser/0103/differential1of2.html>.

43. [www.athletics.concordia.ca](http://athletics.concordia.ca). *Stinger Dome*. 2012 [cited 2012 5 May]; Available from: <http://athletics.concordia.ca/stingerdome.shtml>.
44. Allen, H.J., *Estimation of the Forces and Moments Acting on Inclined Bodies of Revolution of High Fineness Ratio*, NACA, Editor 1949, Ames Aeronautical Laboratory: Washington.
45. Booth, T.B., *The Drag of an Accelerating Submarine Part I Skin Friction (U)*, in *AEW Technical Report*, A.E. Works, Editor 1976, Ministry of Defence: Hampshire.
46. Liesk, T. *Integral Backstepping Control of an Unmanned, Unstable, Fin-less Airship*. in *AIAA Guidance, Navigation and Control Conference*. 2010. Toronto, Canada.
47. Fossen, T.I., *Guidance and Control of Ocean Vehicles*. 1994, United Kingdom: Wiley. 5-42.
48. Google. *Google Maps*. 2012 [cited 2012 March 12]; Available from: <http://maps.google.ca>.
49. Jorgensen, L., *Prediction of Static Aerodynamic Characteristics for Space-Shuttle-Like and Other Bodies at Angles of Attack from 0 to 180*. NASA TN D-6996, 1973.
50. Farivar, D., *Turbulent Uniform Flow around Cylinders of Finite Length*. *AIAA Journal* 1981. **19**(1): p. 275-281.
51. Luo, S.C., Gan, T. L., Chew, Y. T., *Uniform Flow Past One (or Two in Tandem) Finite Length Circular Cylinders*. *Journal of Wind Engineering and Industrial Aerodynamics*. 1996. **59**: p. 69-93.
52. Park, C.W., Lee S. J., *Free End Effects on the Near Wake Flow Structure Behind a Finite Circular Cylinder*. *Journal of Wind Engineering and Industrial Aerodynamics*. 2000. **88**: p. 231-246.
53. Zdravkovich, M.M., Brand, V.P., Mathew, G., Weston, A., *Flow Past Short Circular Cylinders with Two Free Ends*. *Journal of Fluid Mechanics*, 1989. **203**: p. 557-575.
54. Kellock, R.E., Miller, P. H., *Aerodynamic Characteristics of Basic Nose-Cylinder Bodies for Large Ranges of Angle of Attack*. 1971, Air Force Armament Laboratory: Florida.

Appendix A Experimental Setup for Measuring Thrust/Torque Data

Equipment

Peddiraju [8] conducted a comprehensive set of tests to measure the thrust and torque produced by a thruster. For the sake of brevity, only a brief description of his experimental setup will be reviewed here. The overall setup in [8] consists of four components: A thruster stand, a load cell, a microcontroller board and a desktop PC. The thruster was bolted to the top of the rigid cylindrical thruster stand as shown in Figure A-1. The load cell (ATI Gamma F/T transducer) was attached to the base of the thruster.

The commands to run the thruster were sent by the microcontroller via the electronic speed controller (ESC). The ESC drives the external-rotor, brushless motor in the thruster, by furnishing the required amount of current that varies with a 50 Hz square wave pulse generated by the HiQ board, a technique referred to as Pulse Width Modulation (PWM). In the setup used by Peddiraju [8], this PWM signal is normalized between 0 and 1, so that during the experiments, a command input is commanded to the thruster, which is translated to the corresponding PWM and received by the ESC. The width of the 50 Hz-square wave thus varies linearly with the normalized input (called the command input c). The desktop PC logged the force and torque data measured by the F/T sensor.

Experiment

The motor is driven using the ‘JETI Advance 30 plus’ ESC. As mentioned in the previous section, the ESC receives a 50 Hz square wave pulse from the HiQ board, the width of which determines the amount of current that is furnished to drive the motor.

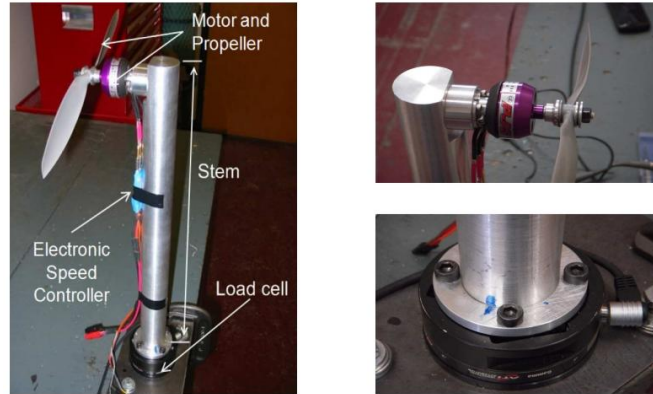


Figure A-1: Experimental setup for measuring thrust and reaction torques. Figure from [8]

The aim of the experiment in [8] was to capture the steady state and transient characteristics of the thrusts and torques generated for a set of command inputs. The thruster was first sent a command input, c , of 0.19, corresponding to ‘idling’ of the thrusters. Subsequently, command inputs 0.25, 0.30, 0.35, 0.40, 0.45 and 0.5 were sent at $t = 14$ s. The response was held for 40 s and the thruster was then commanded back to idle at $t = 54$ s. The forces and torques measured by the F/T sensor were logged by the PC. The thrust characterization that was carried out by Peddiraju[8] using this setup that the transient and steady state behaviours of the thrust, for any given input command, were well captured by a first order transfer function model of the form:

$$G(s) = \frac{T(s)}{c(s)} = \frac{\alpha_g}{\tau s + 1} \quad (\text{A-1})$$

where the parameters τ and α_g were functions of the command input, c . Thus, the transient response was emulated by the time constant τ (time needed to reach 63% of the steady-state thrust), while the steady-state response was emulated by the gain α_g .

Finally, a servo model was also implemented in [8], where it was shown that each servo could be modeled simply by employing a rate-limiter on the rate of the servo rotations.

The reader is referred to [8] for a detailed discussion on the thrust characterization.

Appendix B Estimation of the Aerodynamic Hull Forces

The aerodynamic viscous forces on the hull were computed by Peddiraju [8] based on Jorgensen's [49] derivation. The 3-Dimensional angle of attack α_A of the airship is given by:

$$\alpha_A = \tan^{-1} \frac{(\sqrt{v_{ac}^2 + w_{ac}^2})}{u_{ac}} \quad (\text{B-1})$$

where $\mathbf{v}_{ac} = [u_{ac} \ v_{ac} \ w_{ac}]$ is the velocity of the aerodynamic center, expressed in the body frame. The position of the aerodynamic center is the center of the hull planform.

For $\alpha'_A = \alpha_A$ for $0^\circ \leq \alpha_A \leq 90^\circ$ and $\alpha'_A = 180 - \alpha$ for $90^\circ \leq \alpha \leq 180^\circ$, the final results for the normal force, axial force and pitching moment coefficients, based on the angle of attack of the airship α_A are given below

Normal Force Coefficient C_N :

$$C_N = \eta C_d \sin^2 \alpha'_A; \quad 0^\circ \leq \alpha_A \leq 180^\circ \quad (\text{B-2})$$

Axial Force Coefficient C_A :

$$C_A = C_{A_0} \cos^2 \alpha'_A; \quad 0 \leq \alpha_A \leq 90^\circ \quad (\text{B-3})$$

and

$$C_A = -C_{A_0} \cos^2 \alpha'_A; \quad 90 < \alpha_A \leq 180^\circ \quad (\text{B-4})$$

Pitching Moment Coefficient C_M :

$$C_M = \eta C_d \frac{A_p}{A} \left(\frac{x_m - x_p}{d_{max}} \right) \sin^2 \alpha'_A \quad (\text{B-5})$$

where, x_p is the center of the hull planform measured from the nose.

Appendix C The Cross-flow Drag Model

It is well documented in literature that the drag experienced by a 3D-cylinder (also known as a cylinder of *finite* length) in a cross-flow is affected by the flow separation that occurs at the free ends of the cylinder. Essentially, the flow that separates from the free ends interacts strongly with the flow that separates from the sides of the cylinder, thereby leading to a reduction of the drag relative to the drag of a 2-D cylinder (cylinder of *infinite* length) [50-52]. For low fineness ratio cylinders, this interaction occurs along the entire length while for high fineness ratio cylinders, this interaction is limited to the vicinity of the free ends. For the purpose of deriving the damping moment coefficient, it is useful to have a model of how the drag varies along the length of the airship, when it undergoes a pure cross-flow motion.

Before proceeding, we note that the cross-flow drag of a cylinder has a strong dependence on the cross flow Reynolds number of the flow Re_{cross} such that the drag coefficient remains sufficiently constant in the subcritical regime ($300 < Re_{cross} < 2.5 \times 10^5$) and decreases rapidly when $Re_{cross} > 2.5 \times 10^5$ [35]. Our approach to estimate the damping moment coefficient assumes the airship to be made of differential cylinder discs. To determine the appropriate drag coefficient to use during typical operations of the airship, we must determine the Reynolds number of each of these cylinder disc elements. To begin with, we note that Re_{cross} can be given by:

$$Re_{cross} = \frac{V_{cross}d}{\nu} \quad (C-1)$$

where ν is the kinematic viscosity of the fluid, V_{cross} is the relative cross-flow velocity between the fluid and the differential disc element along the length and d is the disc's

diameter. The local diameter d is known from the hull profile given by Equation (2.39). Given that the airship operates in standard atmosphere, we have a temperature $20^\circ C$, density $\rho = 1.204 \text{ kg m}^{-3}$ and kinematic viscosity $\nu = 14.813 \times 10^{-6} \text{ m}^2 \text{ s}^{-1}$. We can now evaluate Re_{cross} along the length of the airship for an extreme maneuver. For almost all operating conditions, the airship's angular rates remain quite low. In Section 4.2.5 however, we will consider a very high yaw-rate for the airship during flight of about $r = 120 \text{ deg/s}$. We can plot the values of Re_{cross} for this value of r , along the airship's length $x \in [-(L - x_m), x_m]$ using $V_{cross} = rx$ as shown in Figure C-1. Thus the range of values for the Reynolds number, typically, remains under 2.5×10^5 (subcritical regime).

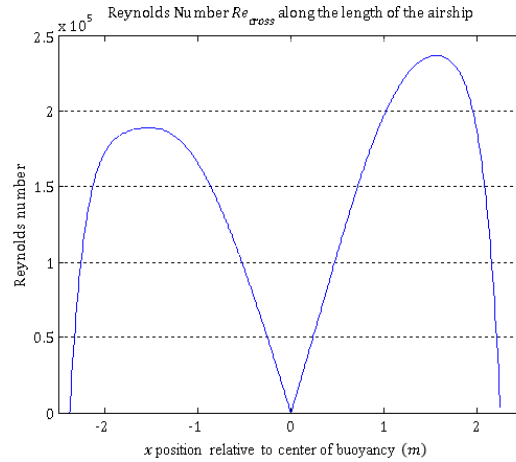


Figure C-1: Reynolds number along the entire length of the airship for $r = 120^\circ/s$

To model the span-wise drag coefficient $C'_d(x)$, experimental data collected by Luo et al. [51] for a 3D single-ended cylinder of fineness ratio $\mu = 4$ will be used, and will be corrected to account for the fact that our airship has two free rounded ends, and has a lower fineness ratio. The data from [51] is reproduced in Figure C-2 showing how the drag coefficient varies from the base of a single-ended cylinder ($l_x = 0$) until the free-end

($l_x = l$). As can be seen, the span-wise drag of a cylinder of this low aspect ratio, generally decreases towards the mid-span of the cylinder. This result for low aspect ratio cylinders is consistent with the data collected by other researchers. Zdravkovich et al. [53], who studied two-ended cylinders, discuss how the inflow from the free-ends significantly alters the downstream wake of the inboard part of the cylinder, as shown in Figure C-3.

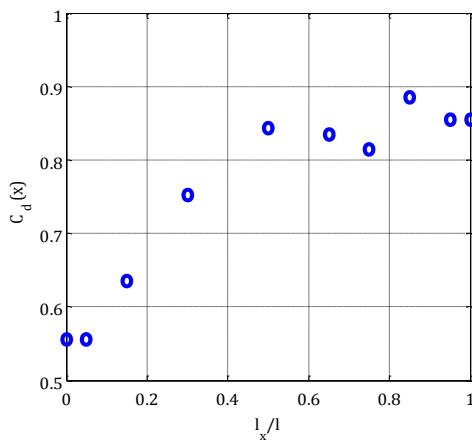


Figure C-2: Span-wise drag variation for a cylinder of aspect ratio 4.

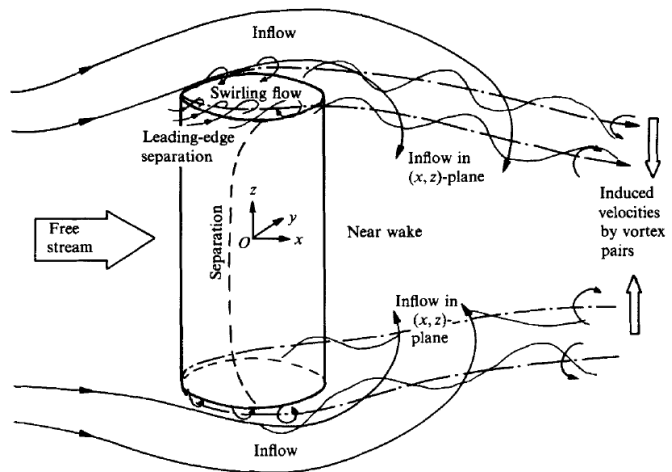


Figure C-3: Cross-flow around a low aspect ratio cylinder with two free-ends [53].

To adapt the data in Figure C-2 to our airship, we treat the center of buoyancy as the base ($l_x = 0$). Data from Figure C-2 can then be used by multiplying the x -axis information in the figure by x_m for the front part of the cylinder and by $(L - x_m)$ for the rear part of the cylinder. We then linearly interpolate these data points, leading to the dashed line in Figure C-4.

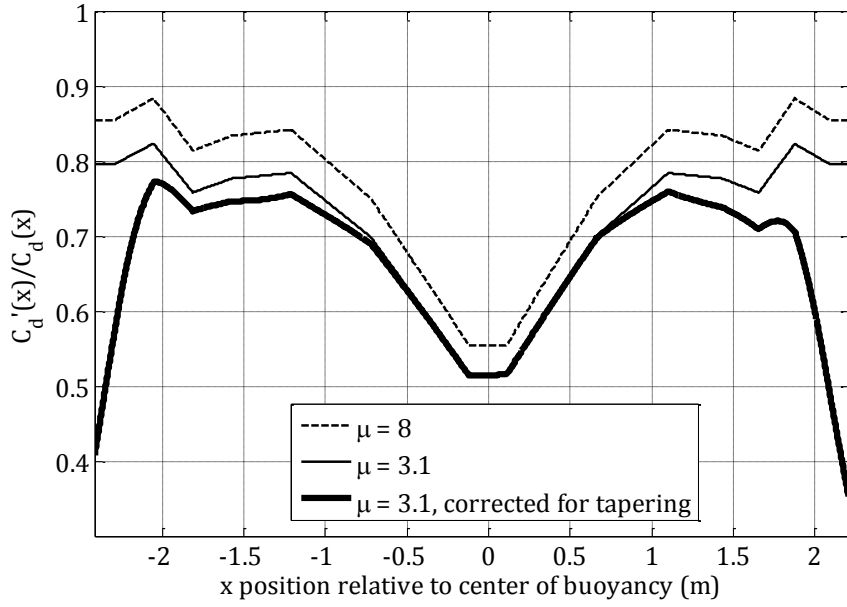


Figure C-4: Drag coefficient along airship length.

Based on our treatment of the data in Figure C-2, the dashed line in Figure C-4 actually represents the drag coefficient along a cylinder of aspect ratio 8 (two single-ended cylinders of aspect ratio 4 joined end to end at the center). We can compare the average value of the drag coefficient $C'_{d_{avg}}|_{\mu=8} = \frac{1}{L} \left[\int_{-(L-x_m)}^{x_m} C'_d(x) \right]$ obtained from the data in Figure C-4 with that measured by Zdaravkovich et al. [53] for a cylinder with two free ends and aspect ratio $\mu = 8$. The average value of the drag coefficient from Figure C-4, $C'_{d_{avg}}|_{\mu=8} = 0.77$, while that obtained from Zdaravkovich et al.'s measurements (Figure 5 in [53]) is ≈ 0.77 . Our approach seems consistent with Zdaravkovich et al.'s results. However, we need to use the data in Figure C-4 for $\mu = 8$ to estimate the drag coefficient variation for a two-ended cylinder with $\mu = 3.1$. While the approach is debatable, we scale the data in Figure C-4 by multiplying it by $\frac{C'_{d_{avg}}|_{\mu=3.1}}{C'_{d_{avg}}|_{\mu=8}}$, where $C'_{d_{avg}}|_{\mu=8} = 0.77$ and $C'_{d_{avg}}|_{\mu=3.1} = 0.72$ [53]. The scaled result is shown as the thin solid line in Figure C-4.

Authors such as Allen [44] also suggest a technique to find $C'_{d_{avg}}$ using a drag-proportionality factor η , which depends on the fineness ratio of a two-ended cylinder, and can be multiplied by the cross-flow drag coefficient of an infinite 2D cylinder at a given Reynolds number $C'_{d_{avg}}|_{\mu=\infty}$ to get the average drag coefficient of a finite two-ended 3D cylinder. Using the data in [44], $\eta \approx 0.6$ for $\mu = 3.1$, and knowing that $C'_{d_{avg}}|_{\mu=\infty} \approx 1.2$ for $Re_{cross} < 2.5 \times 10^5$, we find $C'_{d_{avg}}|_{\mu=3.1} = 0.72$. Thus, our analysis seems consistent with [44].

Zdaravkovich et al. [53] also measured the drag on low aspect ratio cylinders with two hemispherical ends, because most vehicle fuselages have rounded noses, and not upright faces for free-ends. This geometry led to a further reduction in drag. Kellock and Miller [54] suggest a correction for this ‘nose-end effect’ for vehicles with varying radii $R(x)$ along the length of the vehicle. In [54] it is suggested that if the hull-profile half angle $\varepsilon = \tan^{-1}\left(\frac{dR(x)}{dx}\right) \approx 90^\circ$, then almost no drag is contributed by this portion. Also, if $\varepsilon \approx 0^\circ$, the flow is essentially the same as that for an equivalent straight-ended cylinder. The final drag model $C_d(x)$, corrected for the hull-profile half angles as suggested by [54], is given as:

$$C_d(x) = C'_d(x) \cos \varepsilon \quad (\text{C-2})$$

The measurements of $R(x)$ presented in Section 2.4 are used here to calculate $C_d(x)$. Using the scaled data for $C'_d(x)|_{\mu=3.1}$ from Figure C-4 and the hull profile measurement to calculate $\cos \varepsilon$, the drag coefficient $C_d(x)$ given by Equation (C-2) is shown as the thick solid line in Figure C-4.

From Figure C-4, it is seen that since the airship nose and tail hull profiles are quite slanted, ε is large and so the drag coefficient at the ends is reduced. Towards the center, the airship's hull-profile half angle is $\approx 0^\circ$, and so the drag coefficient remains nearly the same as that in for the uncorrected drag coefficient. It is also useful to know the average drag coefficient along the length of the airship $C_{d_{avg}} = \frac{1}{L} \left[\int_{-(L-x_m)}^{x_m} C_d(x) \right]$. This was found to be $C_{d_{avg}}|_{\mu=3.1} = 0.67$. For the purpose of the current thesis, this value of $C_{d_{avg}}|_{\mu=3.1}$ will be denoted simply as C_d .

Although Zdaravkovich et al. [53] measured the drags on cylinders with hemispherical ends for $\mu = 1, 2$ and 3 , (Figure 5 in [53]). If we extrapolate this data for $\mu = 3.1$, we find $C_{d_{avg}} \approx 0.64$. We do not expect this value to exactly match the estimate for our airship since the geometry of a cylinder with hemispherical ends is different than the geometry of the airship. However, a general conclusion can be drawn for both i.e. a reduction in the average drag coefficient due to the tapered ends.

Appendix D Results for Reaction Torques Test

The following is the complete set of results for Section 2.3.4. Figure D-1 shows these results over the entire range of measurement time for each command input, while Figure D-2 shows the details of rise and fall for each command input.

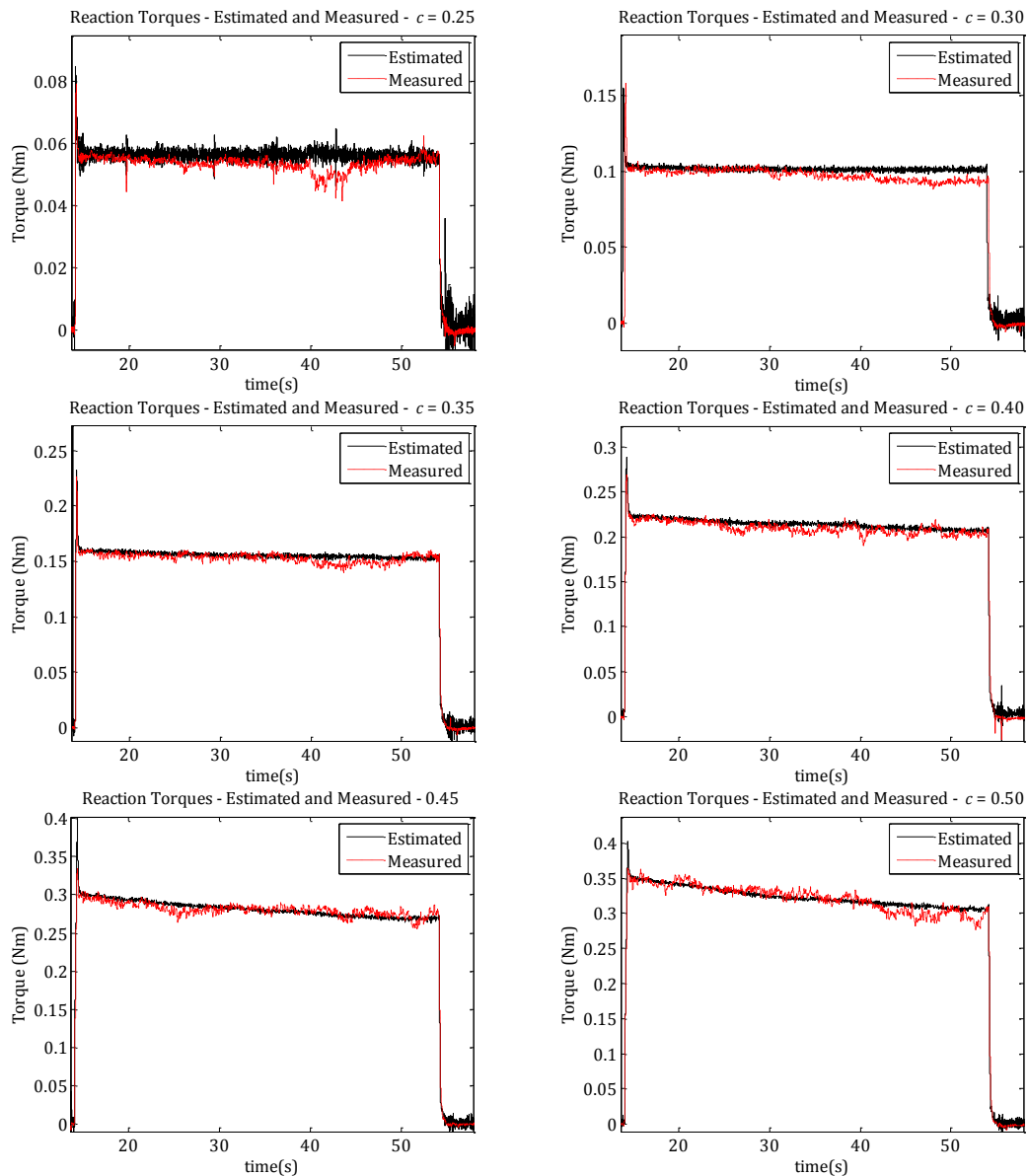


Figure D-1: Measured and estimated reaction torques for 6 different command inputs.

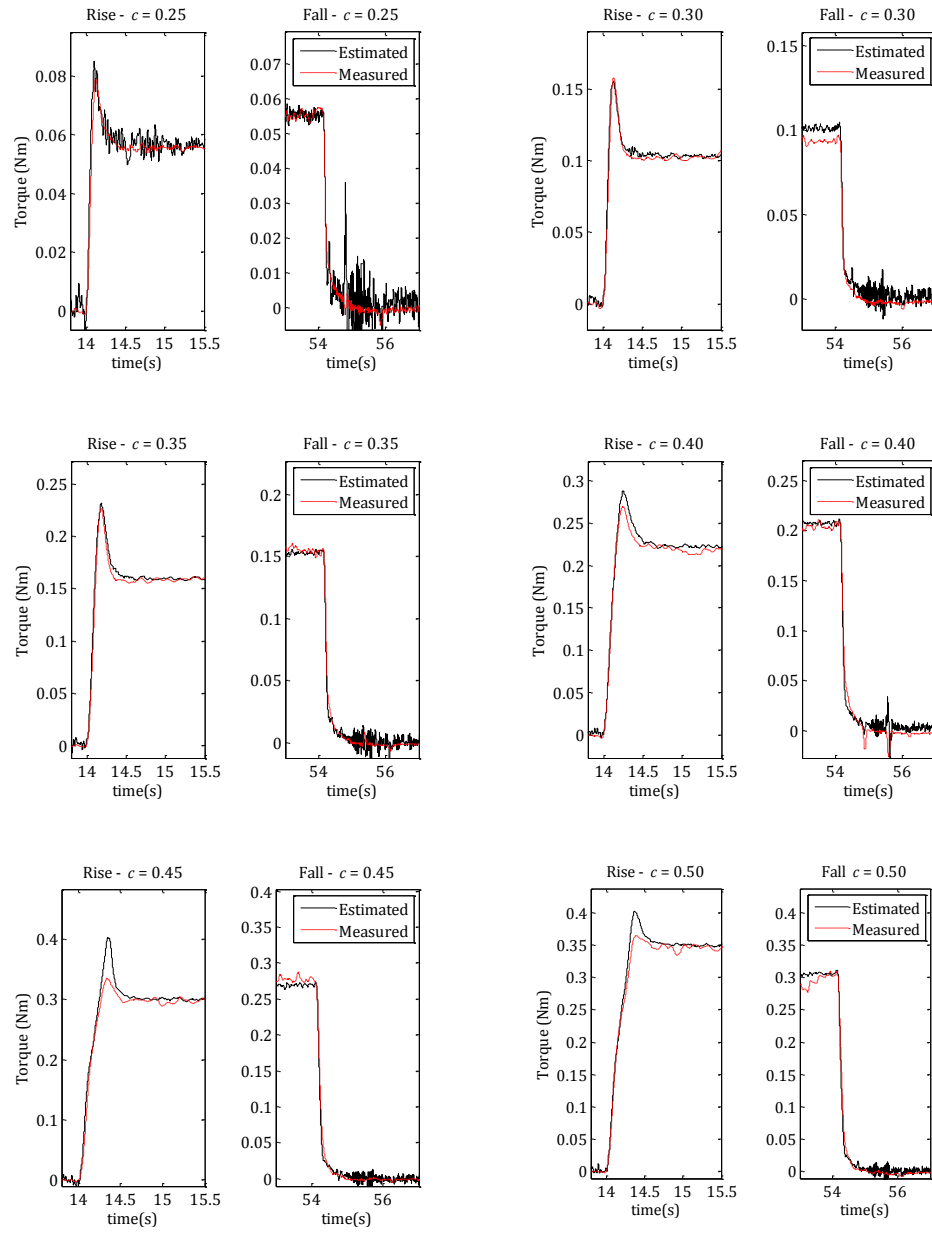


Figure D-2: Measured and estimated reaction torques for 6 different command inputs. Details of rise and fall.

Appendix E Results for Normal Drag Test

The following are the results for the normal drag test as outlined in Section 4.2.3. For each test case, the height during the fall and the corresponding downward velocity are presented.

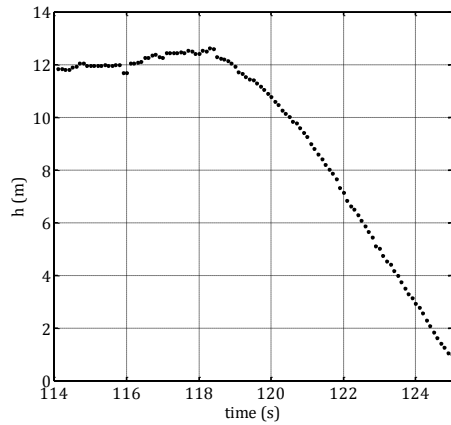


Figure E-1: Inertial height during drop test – Test case B

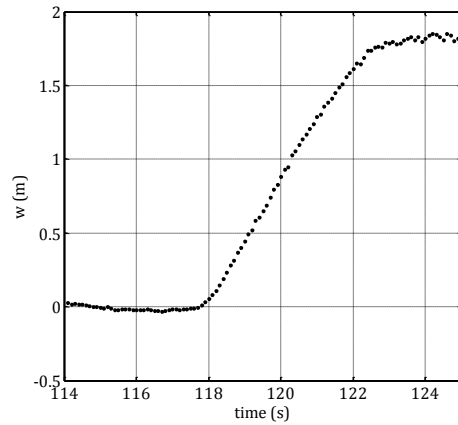


Figure E-2: Downward velocity during drop test – Test case B

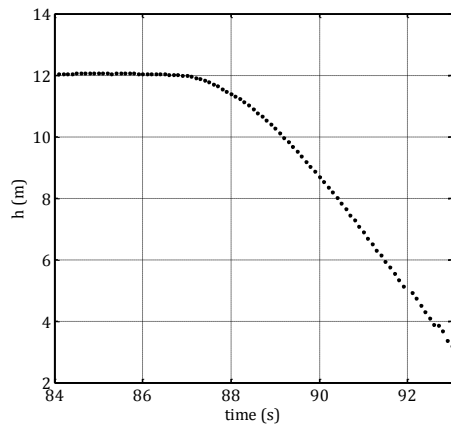


Figure E-3: Inertial height during drop test – Test case C

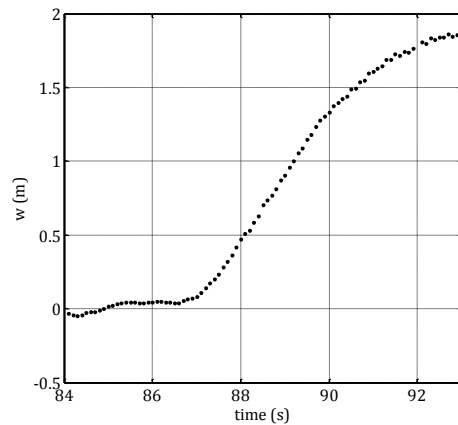


Figure E-4: Downward velocity during drop test – Test case C

Appendix F Results for Axial Drag Test

The following are the results for the axial drag test as outlined in Section 4.2.4. For each test case, the thrust in the x -direction and the corresponding forward velocity is presented.

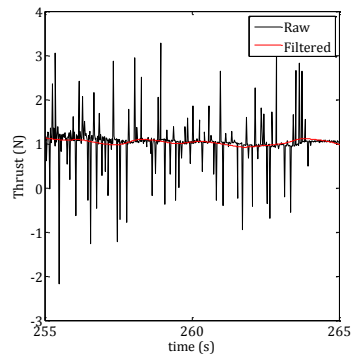


Figure F-1: Total thrust in x , test case A

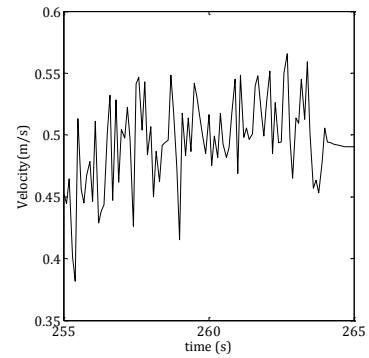


Figure F-2: Forward velocity, test case A

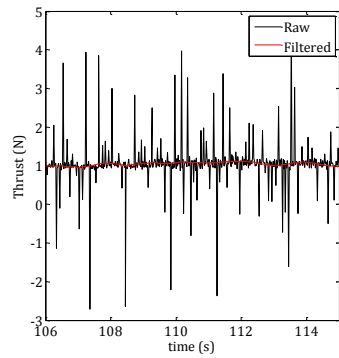


Figure F-3: Total thrust in x , test case B

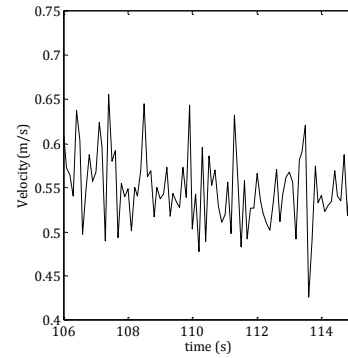


Figure F-4: Forward velocity, test case B

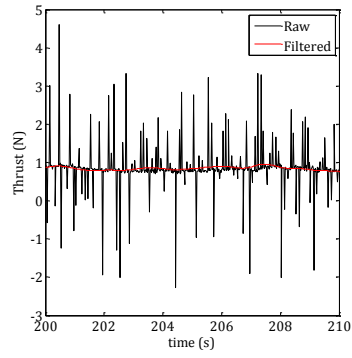


Figure F-5: Total thrust in x , test Case C

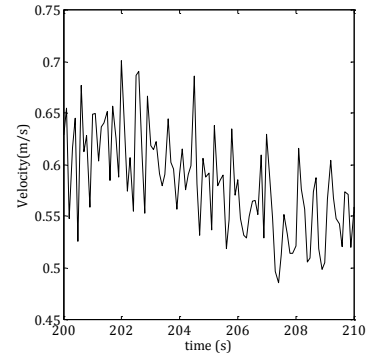


Figure F-6: Forward velocity, test case C

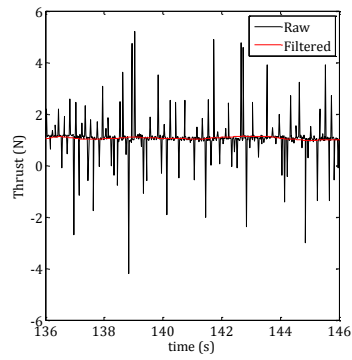


Figure F-7: Total thrust in x , test case D

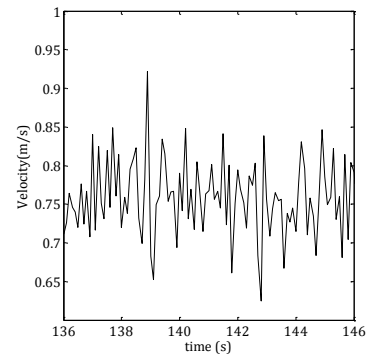


Figure F-8: Forward velocity, test case D

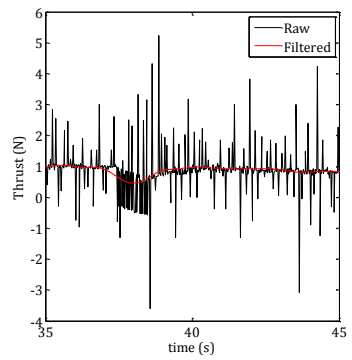


Figure F-9: Total thrust in x , test case E

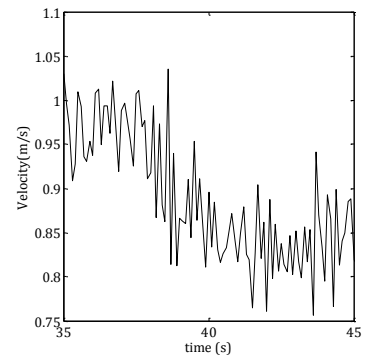


Figure F-10: Forward Velocity, test case E

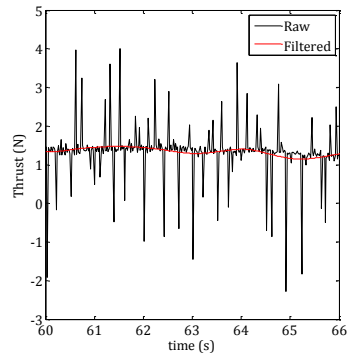


Figure F-11: Total thrust in x , test case F

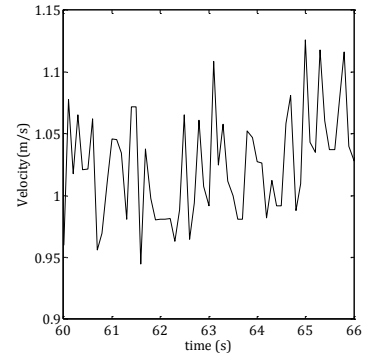


Figure F-12: Forward velocity, test case F

Appendix G Results for Estimation of Longitudinal Added Mass

The following are the results for the longitudinal added mass test as outlined in Section 4.2.6.1. For each test, the total commanded thrust in the x -direction and the corresponding forward acceleration is shown.

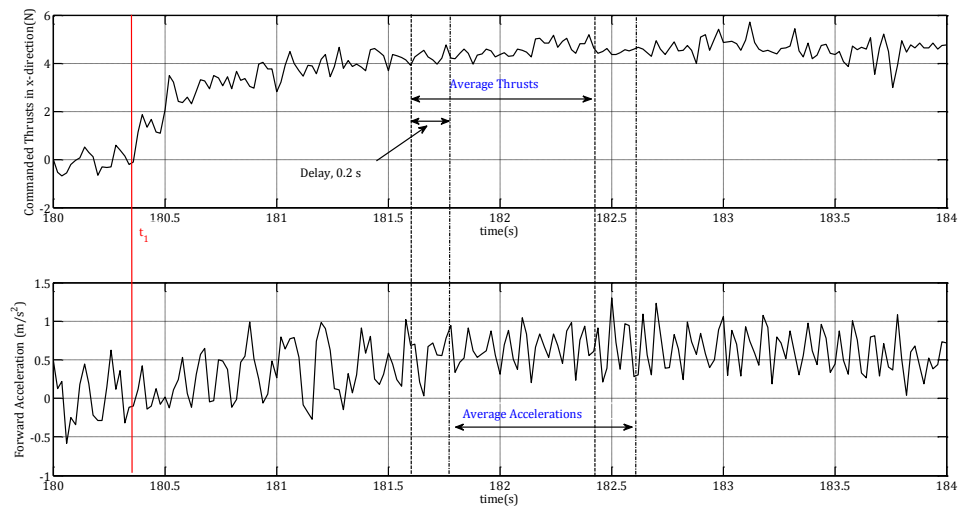


Figure G-1: Commanded thrusts in x-direction (top) and forward acceleration (bottom) – Forward acceleration test : test case 2

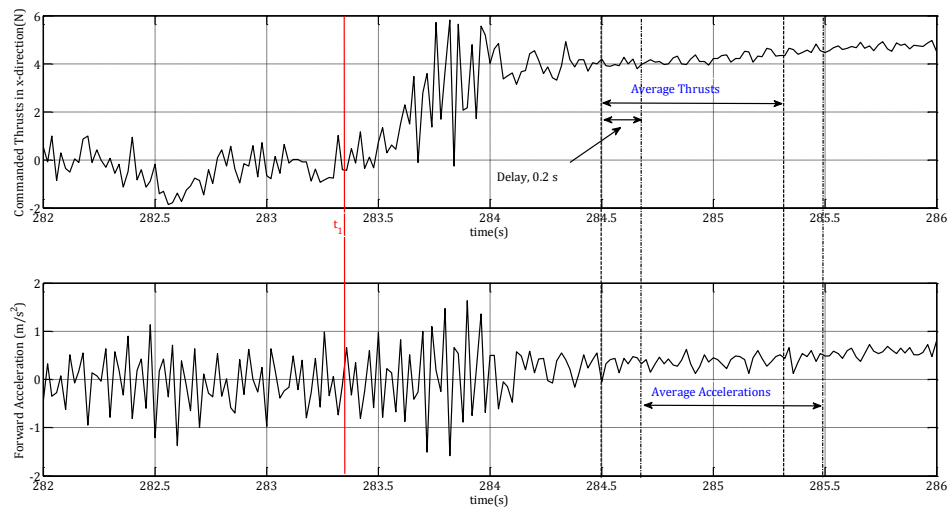


Figure G-2: Commanded thrusts in x-direction (top) and forward acceleration (bottom) – Forward acceleration test : test case 3

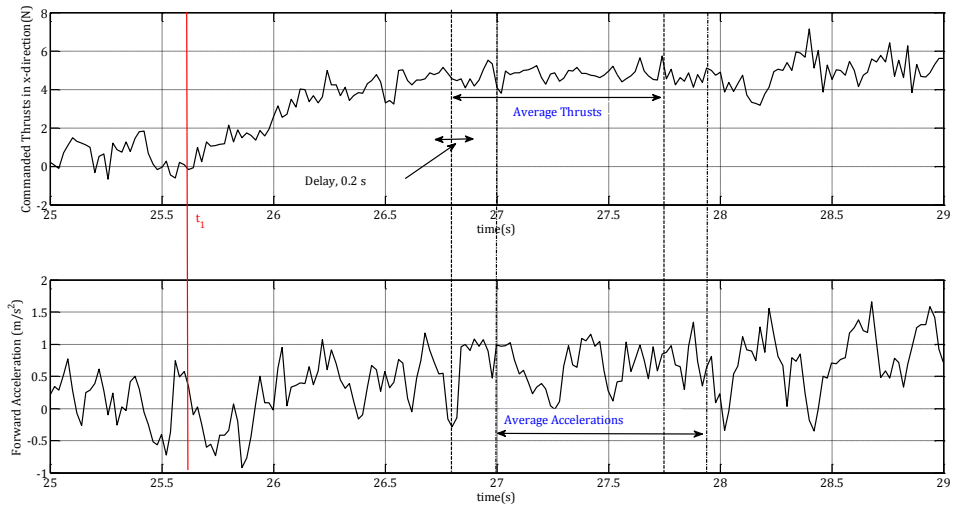


Figure G-3: Commanded thrusts in x-direction (top) and forward acceleration (bottom) – Forward acceleration test : test case 4